Shrinkage and Temperature Forces in Frame Piers

Final Report
February 2023

Iowa State University
Institute for Transportation

Sponsored by
Iowa Highway Research Board
(IHRB Project TR-738)
Iowa Department of Transportation
(InTrans Project 18-633)

About the Bridge Engineering Center

The mission of the Bridge Engineering Center (BEC) is to conduct research on bridge technologies to help bridge designers/owners design, build, and maintain long-lasting bridges.

About the Institute for Transportation

The mission of the Institute for Transportation (InTrans) at Iowa State University is to save lives and improve economic vitality through discovery, research innovation, outreach, and the implementation of bold ideas.

Iowa State University Nondiscrimination Statement

Iowa State University does not discriminate on the basis of race, color, age, ethnicity, religion, national origin, pregnancy, sexual orientation, gender identity, genetic information, sex, marital status, disability, or status as a US veteran. Inquiries regarding nondiscrimination policies may be directed to the Office of Equal Opportunity, 3410 Beardshear Hall, 515 Morrill Road, Ames, Iowa 50011, telephone: 515-294-7612, hotline: 515-294-1222, email: eooffice@iastate.edu.

Disclaimer Notice

The contents of this report reflect the views of the authors, who are responsible for the facts and the accuracy of the information presented herein. The opinions, findings and conclusions expressed in this publication are those of the authors and not necessarily those of the sponsors.

The sponsors assume no liability for the contents or use of the information contained in this document. This report does not constitute a standard, specification, or regulation.

The sponsors do not endorse products or manufacturers. Trademarks or manufacturers' names appear in this report only because they are considered essential to the objective of the document.

Iowa DOT Statements

Federal and state laws prohibit employment and/or public accommodation discrimination on the basis of age, color, creed, disability, gender identity, national origin, pregnancy, race, religion, sex, sexual orientation or veteran's status. If you believe you have been discriminated against, please contact the Iowa Civil Rights Commission at 800-457-4416 or Iowa Department of Transportation's affirmative action officer. If you need accommodations because of a disability to access the Iowa Department of Transportation's services, contact the agency's affirmative action officer at 800-262-0003.

The preparation of this report was financed in part through funds provided by the Iowa Department of Transportation through its "Second Revised Agreement for the Management of Research Conducted by Iowa State University for the Iowa Department of Transportation" and its amendments.

The opinions, findings, and conclusions expressed in this publication are those of the authors and not necessarily those of the Iowa Department of Transportation.

Technical Report Documentation Page

1. Report No. IHRB Project TR-738	**2. Government Accession No.**	**3. Recipient's Catalog No.**

4. Title and Subtitle Shrinkage and Temperature Forces in Frame Piers	**5. Report Date** February 2023
	6. Performing Organization Code
7. Author(s) Behrouz Shafei (orcid.org/0000-0001-5677-6324), Al Nelson (orcid.org/0000-0003-2059-7564), and Cole Shurbert-Hetzel (orcid.org/0000-0001-8646-7485)	**8. Performing Organization Report No.** InTrans Project 18-633
9. Performing Organization Name and Address Bridge Engineering Center Iowa State University 2711 South Loop Drive, Suite 4700 Ames, IA 50010-8664	**10. Work Unit No. (TRAIS)**
	11. Contract or Grant No.
12. Sponsoring Organization Name and Address Iowa Highway Research Board Iowa Department of Transportation 800 Lincoln Way Ames, IA 50010	**13. Type of Report and Period Covered** Final Report
	14. Sponsoring Agency Code IHRB Project TR-738
15. Supplementary Notes Visit https://bec.intrans.iastate.edu/ for color pdfs of this and other research reports.	

16. Abstract

Shrinkage and temperature forces are known to have short- and long-term effects on both the superstructures and substructures of bridges. In the substructure, such effects are more pronounced if frame piers are used, given their volumetric change is often restrained.

The main objective of this research was to investigate the forces developed in frame piers and their supporting foundations due to volumetric changes caused by thermal and shrinkage effects. For this purpose, a set of finite element (FE) models capable of simulating shrinkage strain, creep strain, thermal strain, strength development of concrete, and nonlinear behavior of concrete were developed and calibrated using experimental test results. Field data were then collected from bridges instrumented with vibrating wire strain gauges embedded in the frame piers at the time of construction. Further to obtaining firsthand information from the field, the FE models were validated using collected field data. Various frame pier geometries were then analyzed using the validated model to identify the most susceptible geometries.

The results of the study indicated that frame piers cast in Iowa on warm summer days, particularly in June and July, experience the most demand from temperature and shrinkage effects compared to frame piers cast at other times of the year. The most critical factors affecting frame pier susceptibility were found to be column stiffness, length of the cap beam, and flexural stiffness of the cap beam. Column stiffness was observed to be the most impactful factor on the susceptibility of frame piers to these effects. Basic susceptibility metrics, such as the length of the frame and the length-to-height ratio of the frame, were found to be not accurate enough to predict susceptibility, as accurate susceptibility metrics must account for column stiffness and column restraint factors. These results led to the development of two-dimensional linear elastic models that simplified the assessment process without losing accuracy. Overall, the requirements set by the Iowa DOT's *Bridge Design Manual* were found to be adequate in capturing the performance of frame piers subjected to temperature and shrinkage forces.

17. Key Words bridge frame piers—concrete shrinkage—field investigations—pier cap beams—column restraint—temperature effects	**18. Distribution Statement** No restrictions.

19. Security Classification (of this report) Unclassified.	**20. Security Classification (of this page)** Unclassified.	**21. No. of Pages** 144	**22. Price** NA

Form DOT F 1700.7 (8-72) **Reproduction of completed page authorized**

SHRINKAGE AND TEMPERATURE FORCES IN FRAME PIERS

Final Report
February 2023

Principal Investigator
Behrouz Shafei, Associate Professor
Bridge Engineering Center, Iowa State University

Authors
Behrouz Shafei, Al Nelson, and Cole Shurbert-Hetzel

Sponsored by
Iowa Highway Research Board and
Iowa Department of Transportation
(IHRB Project TR-738)

Preparation of this report was financed in part
through funds provided by the Iowa Department of Transportation
through its Research Management Agreement with the
Institute for Transportation
(InTrans Project 18-633)

A report from
Bridge Engineering Center
Institute for Transportation
Iowa State University
2711 South Loop Drive, Suite 4700
Ames, IA 50010-8664
Phone: 515-294-8103 / Fax: 515-294-0467
https://bec.intrans.iastate.edu/

TABLE OF CONTENTS

LIST OF FIGURES

LIST OF TABLES

ACKNOWLEDGMENTS

The authors would like to acknowledge the Iowa Highway Research Board (IHRB) and the Iowa Department of Transportation (DOT) for sponsoring this research. The authors would also like to thank the Iowa DOT technical advisory committee (TAC) members on this project, including Mike Nop, David Evans, and Curtis Carter.

EXECUTIVE SUMMARY

Background and Problem Statement

Frame piers are a popular type of bridge pier composed of columns that support a cap beam. Frame piers are often the most economical pier choice when a pier does not need to be placed in water or designed for vehicular collisions. However, certain frame pier geometries, such as long frame piers, are susceptible to forces caused by temperature and shrinkage effects. In design, thermal strain, shrinkage strain, creep strain, and even the nonlinear behavior of concrete may not be considered together. This can lead to questions about the adequacy of the current set of design requirements for this category of piers.

Research Description

In this research project, a set of finite element (FE) models capable of simulating shrinkage strain, creep strain, thermal strain, strength development of concrete, and nonlinear behavior of concrete were developed and calibrated using experimental test results. Field data were then collected from bridges instrumented with vibrating wire strain gauges embedded in the frame piers at the time of construction. Further to obtaining firsthand information from the field, the FE models were validated using collected field data. Various frame pier geometries were then analyzed using the validated model to identify the most susceptible geometries. These results led to the development of two-dimensional (2D) linear elastic models that simplified the assessment process without losing accuracy.

Key Findings

- Based on the results of field monitoring activities and supporting FE simulations, it was found that frame piers cast in Iowa on warm summer days, particularly in June and July, experience the most demand from temperature and shrinkage effects compared to other times of the year.
- Frame piers with nonuniform columns, such as larger exterior columns or varying column heights, were not found to be more susceptible to these effects than piers with uniform columns. Bay length was also found to have a negligible effect on the susceptibility of frame piers to these effects.
- The most critical factors affecting frame pier susceptibility were found to be column stiffness, length of the cap beam, and flexural stiffness of the cap beam. Column stiffness was observed to have the greatest impact on the susceptibility of frame piers to these effects.
- The development of 2D linear elastic models helped provide a simplified assessment process without losing accuracy. Overall, the requirements set by the Iowa DOT’s *Bridge Design Manual* were found to be adequate in capturing the performance of frame piers subjected to temperature and shrinkage forces.

Implementation Readiness and Benefits

Considering the construction cost advantages of frame piers compared to hammerhead piers, the development of appropriate design strategies is essential to ensure the satisfactory performance of this category of piers, particularly taking into consideration the fact that they can be subjected to relatively large shrinkage and temperature forces during their service lives.

It was advantageous to develop a set of models with varying levels of complexity capable of simulating the effects of temperature and shrinkage. This helped identify the frame piers most susceptible to these effects. Furthermore, various metrics, along with a simplified 2D analysis, can now be utilized during design to help predict the susceptibility of frame piers to temperature and shrinkage effects.

CHAPTER 1. INTRODUCTION

Background

Frame piers, also known as multi-column piers, are a common type of bridge pier. This pier type consists of multiple columns that support a cap beam. The cap beam directly supports the superstructure of the bridge. The foundations of frame piers can vary significantly to best suit site conditions. Common types of foundations used in frame piers include drilled shafts, pile caps and piles, and spread footings.

Frame piers are common due to their economic benefit compared to other types of piers, such as T piers. This is because the smaller member sizes and simplistic geometry of frame piers use less material and allow for easier construction. These benefits make frame piers the primary choice for piers in road overpasses, railroad overpasses, and stream or river crossings in Iowa when piers do not need to be designed for vehicular collisions or placed in waterways (Iowa DOT Office of Bridges and Structures 2018).

Research Motivation and Objectives

Due to their economic benefits, frame piers are often the top design choice for bridges. However, in some analyses, frame piers may experience high forces due to shrinkage and temperature effects. Designing for these high forces may diminish the economic benefits of using frame piers.

This study aimed to accurately calculate the forces imposed on frame piers by temperature and shrinkage effects and provide design guidance for such forces. The first objective was to develop a numerical model that could accurately model the behavior of frame piers subjected to shrinkage, creep, and temperature effects. The next objective was to identify the most critical factors that make a frame pier susceptible to shrinkage and temperature effects. The last objective was to investigate the accuracy of various metrics used to predict the susceptibility of frame piers to temperature and shrinkage effects.

These objectives were achieved through a set of investigations, ranging from long-term field monitoring to rigorous three-dimensional (3D) and two-dimensional (2D) structural analyses.

Research Summary

A numerical model was developed to simulate the behavior of frame piers under temperature and shrinkage effects. A shrinkage and creep model was selected for the model and calibrated using experimental test results. The numerical model was validated using field data collected from two instrumented frame piers.

The effect of the time of frame pier casting was investigated to determine its effect on the magnitude of forces due to temperature and shrinkage. A worst-case casting time was then chosen for use in a series of parametric studies to investigate the effects of column stiffness, frame length, and bay length on the behavior of frame piers subjected to temperature and shrinkage effects. This investigation was then paired with simplified 2D analyses using linear elastic models.

Research Benefits

The results of this study have led to more informed design guidance for frame piers in Iowa and beyond. The outcome helps predict the susceptibility of frame piers to temperature and shrinkage effects, thus preventing underdesign or overdesign of this important category of piers.

CHAPTER 2. MODELING OF SHRINKAGE AND CREEP

Background

Shrinkage

Shrinkage is the contraction of concrete with time. The overall shrinkage effect is composed of multiple types of shrinkage. The causes, duration, and contribution of total shrinkage strain are different for each shrinkage type. However, two types of shrinkage are most prominent from a design standpoint: autogenous shrinkage and drying shrinkage (Šahinagić-Isović et al. 2012).

Autogenous shrinkage, also known as hydration shrinkage, is caused by the loss of water in the concrete's pores due to the chemical processes involved in hydration. Since autogenous shrinkage depends on hydration, the rate of this shrinkage matches closely to the rate of strength development of the concrete and is most prominent in the first month after casting. For example, 60 to 90% of autogenous shrinkage of concrete occurs by 28 days (Šahinagić-Isović et al. 2012). Autogenous shrinkage strain affects ordinary concrete much less than drying shrinkage strain. A typical range of ultimate autogenous shrinkage strain is 50 to 100 microstrain (Tinni 2008).

Drying shrinkage is caused by the loss of water in the pore spaces of the concrete to the environment. Environmental factors, such as humidity, wind velocity, and temperature, majorly influence drying shrinkage (Ali and Urgessa 2014). Additionally, concrete thickness affects drying shrinkage, with drying shrinkage occurring more slowly in thicker members. Drying shrinkage occurs over a much longer period than autogenous shrinkage. For ordinary concrete, drying shrinkage is generally several times more prominent than autogenous shrinkage, with a typical range of 200 to 400 microstrain (Šahinagić-Isović et al. 2012).

Another type of shrinkage, known as plastic shrinkage, can be a significant component of total shrinkage. However, plastic shrinkage only occurs in the first hours after casting and is caused by rapid evaporation or absorption of water into formwork and the environment. Generally, the strength of concrete is too low when plastic shrinkage occurs for notable stresses to form in the concrete. Additionally, current curing practices mitigate rapid evaporation of water, thus further reducing the effects of plastic shrinkage (Šahinagić-Isović et al. 2012).

The progression of shrinkage greatly depends on the concrete mixture, geometry, and climate conditions (Khatami et al. 2016, Kulkarni and Shafei 2018, Khatami and Shafei 2021). Generally, a shrinkage curve is steepest early on and then flattens with age. For example, up to 34% of the ultimate shrinkage can occur in the first 2 weeks after casting, and up to 80% can occur in the first 3 months (Gribniak et al. 2013). Since shrinkage can occur so rapidly early on, it can be relaxed with time by creep. Around 40 to 70% of shrinkage stress can be relaxed by creep (Gribniak et al. 2013, Altoubat and Lange 2001). Due to the stress relaxation from creep, many design guides, like the Bridge Design Manual (BDM) from the Iowa DOT, design for shrinkage effects at 28 days after casting (Iowa DOT Office of Bridges and Structures 2018).

Both tensile and compressive stresses are known to result from shrinkage in reinforced concrete. In unrestrained members, the steel reinforcement generally experiences compressive stress, while the concrete generally experiences tensile stress. Tensile stress in the concrete is critical, since concrete is susceptible to cracking under tensile stresses which adversely affects the performance of the concrete (Gilbert 1992). Stress induced by shrinkage can affect the structural behavior of reinforced concrete. For example, shrinkage in reinforced concrete columns has been found to reduce stiffness, cracking resistance, and ultimate strength. The magnitude of these effects depends on the amount of steel reinforcement in the member and the shape of the member (Lampropoulos and Dritsos 2011).

Shrinkage does not occur uniformly throughout a cross section of a concrete member. Rather, the magnitude of shrinkage varies throughout the cross section due to the difference in moisture content at the surface and at the center of a member (Karim et al. 2019, Shi et al. 2020a, Shi et al. 2020b, Kazemian and Shafei 2022). However, it is common to consider an average shrinkage strain for analysis purposes. For example, many popular shrinkage models estimate shrinkage by providing a single, average shrinkage strain for a concrete member (ACI 209 2008, ACI 209 1992, Baweja 1995). One method to apply shrinkage strain in analysis is to input the strain as a static, initial condition (Lampropoulos and Dritsos 2011). This approach is limiting since shrinkage varies with time, as does the strength of concrete. A more suitable approach for time-sensitive analyses is to accurately model the shrinkage strain with time, which most shrinkage models are capable of calculating.

Creep

Creep occurs when concrete continuously deforms over time under a sustained load. Creep strain depends on stress history, with the amount of creep increasing as stress increases. Creep depends on time and occurs most rapidly soon after a load is applied. Under certain loading and structural configurations, creep can act as a stress relaxation mechanism. For example, creep can relax stress due to restrained shrinkage. An important property of creep under variable loading is that after a load is removed, only part of the creep strain is recoverable, and the recovery is time dependent (ACI 209 2008).

Creep is often quantified in one of two ways: creep coefficient or specific creep (Tong 2016). Creep coefficient is the ratio of creep strain to elastic strain. Specific creep, also known as creep compliance, is the total stress dependent strain per unit stress. There are two components of creep: basic creep and drying creep. Basic creep is generally considered a constitutive material property and independent of geometry (ACI 209 2008). Basic creep occurs even when concrete is fully submerged in water. Drying creep is defined as the total strain minus shrinkage strain, basic creep strain, and elastic strain. Drying creep requires both the drying of concrete and an applied stress and does not occur if either is absent.

Depending on the level of stress and desired accuracy, it may be adequate to assume that the creep coefficient for tensile creep is equal to that of compressive creep (ACI 209 2008). This assumption is useful as compressive creep in concrete has been studied significantly more than tensile creep (Østergaard et al. 2001, Khan et al. 2017, Bissonnette and Pigeon 1995, Wei and

Hansen 2012). However, studies have noted differences in the behavior of tensile creep and compressive creep (Wei and Hansen 2012, Ranaivomanana et al. 2013, Gilbert and Ranzi 2018). Therefore, it is suitable to uniquely account for tensile creep and compressive creep in analyses where creep is an important factor.

The literature focuses more on compressive creep, partly because concrete’s lower strength under tension compared to compression means that tensile creep experiments need to be performed at much lower stress levels than compressive experiments. The lower stress levels make reliably measuring creep strain more difficult. The studies that have investigated tensile creep behavior discovered that more tensile creep occurs than compressive creep under the same loading (Wei and Hansen 2012).

Modeling Shrinkage and Creep

Modeling shrinkage and creep is a demanding task due to the large number of variables that must be considered and the complexity of the mechanisms that cause shrinkage and creep. Fortunately, numerous models have been developed to predict shrinkage and creep. These models are often empirical and may only require a few inputs to predict shrinkage or creep. However, the simplicity of these models can lead to significant error, especially when predicting shrinkage and creep of concrete composed of an unusual mixture or exposed to unusual environmental conditions.

This chapter explores some of the most popular shrinkage and creep models that are used in bridge research. The performance of various shrinkage and creep models were analyzed by comparing the outputs of each model to data from shrinkage and creep experiments. The concrete mix and environmental conditions of the experiments used to assess the models were selected to match well with those for frame piers. A single shrinkage and creep model was selected and further calibrated for tensile creep and variable loading. The final calibrated model was used throughout this study in tandem with finite element (FE) analysis software to simulate the effects of temperature and shrinkage for frame piers.

Available Shrinkage and Creep Models

ACI 209R Model

The American Concrete Institute (ACI) 209R shrinkage and creep model empirically predicts the shrinkage strain and creep coefficient of concrete as a function of time (ACI 209 1992, 2008). This model also provides an ultimate shrinkage strain and creep coefficient. Shrinkage strain is predicted based on the age of the concrete, curing method, time of drying, relative humidity, volume to surface ratio, slump, fine aggregate to total aggregate ratio, cement content, and air content. The creep coefficient is predicted based on the age of the concrete, curing method, time of loading, relative humidity, volume to surface ratio, slump, fine aggregate to total aggregate ratio, and air content. The ACI model defines shrinkage strain according to equation (2.1).

$$\varepsilon_{sh}(t,t_c) = \frac{(t-t_c)^{\alpha}}{f+(t-t_c)^{\alpha}}\varepsilon_{shu} \tag{2.1}$$

where $\varepsilon_{sh}(t,t_c)$ is the shrinkage strain at a concrete age of t days, t_c is the age of the concrete at the time of drying in days, α is a constant between 0.90 and 1.10 to tune the model to experimental data, f is a constant between 20 to 130 days to tune the model to experimental data, and ε_{shu} is the ultimate shrinkage strain. The ultimate shrinkage strain is defined according to equations (2.2) and (2.3).

$$\varepsilon_{shu} = 780\gamma_{sh}(10^{-6}) \tag{2.2}$$

$$\gamma_{sh} = \gamma_{sh,tc}\gamma_{sh,RH}\gamma_{sh,vs}\gamma_{sh,s}\gamma_{sh,\psi}\gamma_{sh,c}\gamma_{sh,\alpha} \tag{2.3}$$

where γ_{sh} is the product of all correction factors for the ultimate shrinkage strain.

Creep coefficient at any time according to ACI 209R model is defined according to equation (2.4).

$$\phi(t,t_0) = \frac{(t-t_0)^{\psi}}{d+(t-t_0)^{\psi}}\phi_u \tag{2.4}$$

where $\phi(t,t_0)$ is the creep coefficient at a concrete age of t days, t_0 is the age of the concrete at the time of loading in days, ψ is a constant between 0.40 and 0.80 to tune the model to experimental data, d is a constant between 6 to 30 days to tune the model to experimental data, and ϕ_u is the ultimate creep coefficient. The ultimate creep coefficient is defined according to equations (2.5) and (2.6).

$$\phi_u = 2.35\gamma_c \tag{2.5}$$

$$\gamma_c = \gamma_{c,to}\gamma_{c,RH}\gamma_{c,vs}\gamma_{c,s}\gamma_{c,\psi}\gamma_{c,\alpha} \tag{2.6}$$

where γ_c is the product of all correction factors for the ultimate creep coefficient.

A significant benefit of the ACI 209R model is that the model is relatively simple yet allows tuning the model to experimental data. For example, the α, f, ψ, and d constants from equations (2.1) and (2.4) can tune the shape of the shrinkage strain and creep coefficient curves. Additional factors can be applied to the ultimate shrinkage strain and ultimate creep coefficient to modify the ultimate values. This allows the model to accurately match nearly any set of experimental data. The model also provides recommended ranges for ultimate shrinkage strain, ultimate creep coefficient, and all constants to ensure an accurate estimate is obtained.

AASHTO Model

The American Association of State Highway and Transportation Officials (AASHTO) shrinkage and creep model empirically predicts the shrinkage strain and creep coefficient of concrete as a function of time (AASHTO 2012).

Shrinkage strain in this model is predicted based on the age of the concrete, time of drying, relative humidity, volume to surface ratio, and compressive strength of the concrete. The creep coefficient in this model is predicted based on the age of concrete, time of loading, relative humidity, volume to surface ratio, and compressive strength of the concrete. Shrinkage strain according to the AASHTO model is defined according to equation (2.7).

$$\varepsilon_{sh} = 0.48 k_s k_{hs} k_f k_{td} (10^{-3}) \tag{2.7}$$

where ε_{sh} is the shrinkage strain at any time and k_s, k_{hs}, k_f, and k_{td} are correction factors.

Creep coefficient according to the AASHTO model is defined according to equation (2.8).

$$\phi = 1.9 k_s k_{hc} k_f k_{td} {t_i}^{-0.118} \tag{2.8}$$

where ϕ is the creep coefficient at any concrete age, and k_s, k_{hc}, k_f, and k_{td} are correction factors.

The AASHTO shrinkage and creep model is one of the simplest models available. This is because the model is less general and intended for use on a specific set of structures with regulated concrete mixtures, curing techniques, and geometries. Under conditions that the model is intended for, the AASHTO model can quickly provide shrinkage and creep values.

However, if conditions differ from what the model is geared towards, the AASHTO model will likely provide inaccurate predictions. Furthermore, the AASHTO model lacks clear constants with recommended ranges to tune the model to experimental data. However, the model can easily be tuned to match long-term shrinkage and creep behavior by introducing factors into shrinkage strain and creep coefficient equations.

Bažant-Baweja B_3 Model

The Bažant-Baweja B_3 model is a hybrid empirical and theoretical shrinkage and creep model that predicts the shrinkage strain and creep compliance of concrete as a function of time (ACI 209 2008). This model provides ultimate values of shrinkage strain and creep compliance as well as distinguishes between the basic and drying components of creep.

This model predicts shrinkage strain based on the age of the concrete, curing method, time of drying, relative humidity, concrete strength, cement type, water content, cross section shape, and volume to surface ratio. Creep compliance in this model is predicted based on the age of the concrete, curing method, time of drying, time of loading, strength of the concrete, relative humidity, cement content, water to cement ratio, aggregate to cement ratio, cross section shape, and volume to surface ratio. Shrinkage strain according to the B_3 model is defined according to equation (2.9).

$$\varepsilon_{sh}(t,t_c) = \varepsilon_{sh\infty} k_h S(t-t_c) \tag{2.9}$$

where $\varepsilon_{sh}(t,t_c)$ is the shrinkage strain at concrete age t in days, t_c is the age of the concrete at the start of drying in days, $\varepsilon_{sh\infty}$ is the ultimate shrinkage strain, k_h is a humidity dependence factor, and $S(t-t_c)$ is the time curve. The time curve is calculated as defined in equations (2.10) and (2.11).

$$S(t-t_c) = tanh\sqrt{\frac{(t-t_c)}{\tau_{sh}}} \tag{2.10}$$

$$\tau_{sh} = 190.8{t_c}^{-0.08}{f_{cm28}}^{-0.25}[2k_s(V/S)]^2 \tag{2.11}$$

where τ_{sh} is the shrinkage half-time in days, f_{cm28} is the mean compressive strength of the concrete at 28 days, k_s accounts for member shape, and V/S is the volume to surface ratio. The ultimate shrinkage strain is defined according to equation (2.12).

$$\varepsilon_{sh\infty} = \varepsilon_{s\infty}\frac{E_{cm607}}{E_{cm(t_c+\tau_{sh})}} \tag{2.12}$$

where $\varepsilon_{s\infty}$ is a constant and E_{cm607} and $E_{cm(t_c+\tau_{sh})}$ are the elastic moduli at their corresponding times.

Creep compliance according to the B_3 model is defined according to equation (2.13).

$$J(t,t_0) = q_1 + C_0(t,t_0) + C_d(t,t_0,t_c) \tag{2.13}$$

where $J(t,t_0)$ is the creep compliance at a concrete age of t in days, t_0 is the time of loading in days, q_1 is a constant, $C_0(t,t_0)$ accounts for basic creep, and $C_d(t,t_0,t_c)$ accounts for drying creep. $C_0(t,t_0)$ and $C_d(t,t_0,t_c)$ are defined according to equations (2.14) and (2.15), respectively.

$$C_0(t,t_0) = q_2Q(t,t_0) + q_3ln[1+(t-t_0)^n] + q_4ln(t/t_0) \tag{2.14}$$

$$C_d(t,t_0,t_c) = q_5\left[e^{-8H(t)} - e^{-8H(t_0)}\right]^{1/2} \tag{2.15}$$

where q_2, q_3, q_4, and q_5 are all constants, $Q(t, t_0)$ is a component of aging velocity, n is taken as 0.1, and $H(t)$ and $H(t_0)$ are special averages of pore relative humidity. $H(t)$ and $H(t_0)$ are calculated as defined in equations (2.16) through (2.19).

$$H(t) = 1 - (1 - h)S(t - t_c) \tag{2.16}$$

$$H(t_0) = 1 - (1 - h)S(t_0 - t_c) \tag{2.17}$$

$$S(t - t_c) = tanh\sqrt{\left(\frac{t - t_c}{\tau_{sh}}\right)^{1/2}} \tag{2.18}$$

$$S(t_0 - t_c) = tanh\sqrt{\left(\frac{t_0 - t_c}{\tau_{sh}}\right)^{1/2}} \tag{2.19}$$

where h is relative humidity as a decimal, $S(t - t_c)$ and $S(t_0 - t_c)$ time curves, and τ_{sh} is shrinkage half-time in days.

The B_3 model has unique advantages due to its ties to theory. For example, basic and drying creep, as well as specific components of shrinkage, are separated in this model. Additionally, this model is well suited for general use over a wide range of parameters affecting shrinkage and creep. However, this model has little advantage over simple empirical models when calibrating a model to experimental data. This model is complex, especially in comparison to the ACI or AASHTO shrinkage models.

CEB MC90-99 Model

The Euro-International Committee for Concrete (CEB) model is an empirical shrinkage and creep model that predicts the shrinkage strain and creep compliance of concrete as a function of time (ACI 209 2008). Similar to the B_3 model, the CEB model differentiates between autogenous and drying shrinkage. Additionally, the creep compliance function is calculated from a creep coefficient.

Shrinkage strain in this model is predicted based on the age of concrete, time of drying, relative humidity, volume to surface ratio, cement type, and compressive strength of the concrete. Creep compliance in this model is predicted based on the age of concrete, time of loading, relative humidity, volume to surface ratio, cement type, and compressive strength of the concrete. Shrinkage strain according to the CEB model is defined according to equation (2.20).

$$\varepsilon_{sh}(t, t_c) = \varepsilon_{cas}(t) + \varepsilon_{cds}(t, t_c) \tag{2.20}$$

where $\varepsilon_{sh}(t, t_c)$ is the total shrinkage at a concrete age of t days, t_c is the age of the concrete at the start of drying in days, $\varepsilon_{cas}(t)$ is the autogenous component of shrinkage, and $\varepsilon_{cds}(t, t_c)$ is the drying component of shrinkage. The autogenous component of shrinkage is defined according to equations (2.21) and (2.22), respectively.

$$\varepsilon_{cas}(t) = \varepsilon_{caso}(f_{cm28})\beta_{as}(t) \tag{2.21}$$

$$\beta_{as}(t) = 1 - e^{\left[-0.2\left(\frac{t}{t_1}\right)^{0.5}\right]} \tag{2.22}$$

where $\varepsilon_{caso}(f_{cm28})$ is the notional autogenous shrinkage coefficient, $\beta_{as}(t)$ is the time development factor for autogenous shrinkage, and t_1 is one day. The drying component of shrinkage is defined according to equations (2.23) and (2.24).

$$\varepsilon_{cds}(t, t_c) = \varepsilon_{cdso}(f_{cm28})\beta_{RH}(h)\beta_{ds}(t - t_c) \tag{2.23}$$

$$\beta d_s(t - t_c) = \sqrt{\frac{(t-t_c)/t_1}{350[(V/S)/(V/S)_0]^2 + ((t-t_c)/t_1)}} \tag{2.24}$$

where $\varepsilon_{cdso}(f_{cm28})$ is the notional drying shrinkage coefficient, $\beta_{RH}(h)$ accounts for relative humidity, $\beta d_s(t - t_c)$is the time development factor for drying shrinkage, V/S is the volume to surface ratio, and $(V/S)_0$ is 2 in.

Creep compliance according to the CEB model is defined according to equation (2.25).

$$J(t, t_0) = \frac{1}{E_{cm28}}[\eta(t_0) + \phi_{28}(t, t_0)] = \frac{1}{E_{cmto}} + \frac{\phi_{28}(t,t_0)}{E_{cm28}} \tag{2.25}$$

where $J(t, t_0)$ is creep compliance at a concrete age of t days, t_0 is the time of loading in days, E_{cm28} is the modulus of elasticity at an age of 28 days, E_{cm28} is the modulus of elasticity at an age of 28 days (psi), E_{cmto} is the modulus of elasticity at the time of loading (psi), $\eta(t_0)$ is the ratio of E_{cm28} to E_{cmto}, and $\phi_{28}(t, t_0)$ is 28-day the creep coefficient. The 28-day creep coefficient is defined according to equations (2.26) and (2.27).

$$\phi_{28}(t, t_0) = \phi_0\beta_c(t - t_0) \tag{2.26}$$

$$\beta_c(t - t_0) = \left[\frac{(t-t_0)/t_1}{\beta_H + (t-t_0)/t_1}\right]^{0.3} \tag{2.27}$$

where ϕ_0 is the notional creep coefficient, $\beta_c(t - t_0)$ is a coefficient that accounts for the time development of creep, and β_H accounts for relative humidity.

Similar to the B_3 model, the CEB model differentiates between basic and drying creep. Furthermore, the CEB model also differentiates between drying and autogenous components of shrinkage. The CEB model also allows for modifications to account for unusual temperatures and stress levels.

Model Calibration and Selection

An abundance of shrinkage and creep experiments have been performed and published. With that in mind, this study used available experimental data from the Northwestern University Infrastructure Technology Institute (ITI-NU) database to calibrate and analyze the considered models. This database, formerly known as the RILEM database, was created 40 years ago and hosts experimental data from concrete shrinkage and creep tests. Over its life, this database has expanded in collaboration with ACI, CEB, and RILEM and is now maintained by the ITI-NU. The expanded database hosts data for 490 shrinkage tests and 621 creep tests as of 2008 (Bažant and Li 2008).

The primary purpose of the database is to calibrate and validate prediction models, which made this database suitable for calibrating and comparing models in this study. Additionally, the data in this database are mostly for low-strength and normal-strength concrete, which are common for frame piers. Comparing the performance of the shrinkage and creep models by using all the available data in the ITI-NU database is a feat that has already been done and offered little benefit to this study due to the large variation in parameters explored by the test results in the database. This study focused on a single category of structures—frame piers—which are constructed with consistent concrete mixes that adhere to governing codes and standards, common geometry, and relatively common environmental exposure.

Therefore, it was necessary to only select tests from the database that aligned with the mix design and environmental factors that frame piers are known to experience. This approach was preferred due to the high demand needed for a model to accurately capture the effect of all possible ranges of parameters relating to shrinkage and creep. Each of the shrinkage and creep models was calibrated to selected data from the ITI-NU database. Only the ACI model provides variables and guidance for this type of calibration. However, calibration factors are applied to all models. The calibration factors target the time development and ultimate values of shrinkage and creep.

Unrestrained Shrinkage

The shrinkage models were calibrated for unrestrained shrinkage using available experimental data from the ITI-NU database. A selection of experiments from the ITI-NU database were chosen based on how well their mix designs, curing types, curing durations, environmental conditions, and ages of exposure to drying compared to that of frame piers.

The concrete mixtures of the selected experiments needed to match reasonably well with Class A concrete as specified by AASHTO (AASHTO 2012). For curing, the selected samples needed to use moist curing and be allowed to cure for at least two full days. For environmental factors, the selected experiments needed to have a relative humidity between 50% and 80% and be exposed to a constant temperature around 68°F (20°C). Ten experiments from the ITI-NU database were selected based on these criteria and used to calibrate the shrinkage models. The most notable properties of each experiment selected are presented in Table 2.1.

Table 2.1. ITI-NU database experiments used to calibrate and compare shrinkage models

Database File	w/c	a/c	Cement (kg/m^3)	f_{c28} (MPa)	2VS (mm)	t_0 (day)	Humidity (%)
e_100_01	0.48	5.429	350	33.2	42	7	65
e_100_02	0.48	5.429	350	33.2	80	7	65
e_100_03	0.48	5.429	350	33.2	150	7	65
e_011_03	0.45	5.392	345	35.3	100	7	65
e_069_03	0.45	5.405	353	23.9	75	7	65
e_071_02	0.5	-	350	40.7	75	3	65
e_071_03	0.5	-	350	37.5	75	3	65
e_084_01	0.48	5.428	350	33.2	41.5	7	65
e_084_02	0.48	5.428	350	33.2	80	7	65
e_084_03	0.48	5.428	350	33.2	150	7	65

The selected experiments for shrinkage calibration and analysis had an average 28-day compressive strength of 4.88 ksi (33.7 MPa) and an average age of the concrete at the start of drying of 6.2 days. Additionally, all selected shrinkage experiments had a relative humidity of 65%. Each model was calibrated for shrinkage through two means. First, a single factor was applied to the ultimate shrinkage strain in each model. This factor could be adjusted for each model to best match the model to the experiments. For example, if a model was found to predominantly underestimate the shrinkage recorded in the experiments, this factor could be set to a value higher than unity to improve the accuracy of the model.

A second factor was applied to the time development component of each model. This second factor attempted to modify the shape of the shrinkage curve of each model. For instance, if the long-term predicted shrinkage of a model closely matched that of the experiments, but the rate of shrinkage development differed notably, this factor could be set different from unity to alter the rate at which shrinkage development was predicted.

The ACI model already had two well defined coefficients built in that served as this second factor. However, since the remaining models considered had no such factor already built in, a factor was inserted into each model mimicking that of the ACI defined factors. The calibration factors were calibrated such that each model had only one value for each factor that covered every experiment (i.e., models with a single value for each calibration factor). For each model, data from the selected experiments were plotted against the predicted values of the calibrated models. A data point perfectly matched between the model and experiment if it landed on a line with a slope of one originating from the origin. A graphical comparison of the calibrated models to data from the ITI-NU database is presented in Figure 2.1 through Figure 2.4.

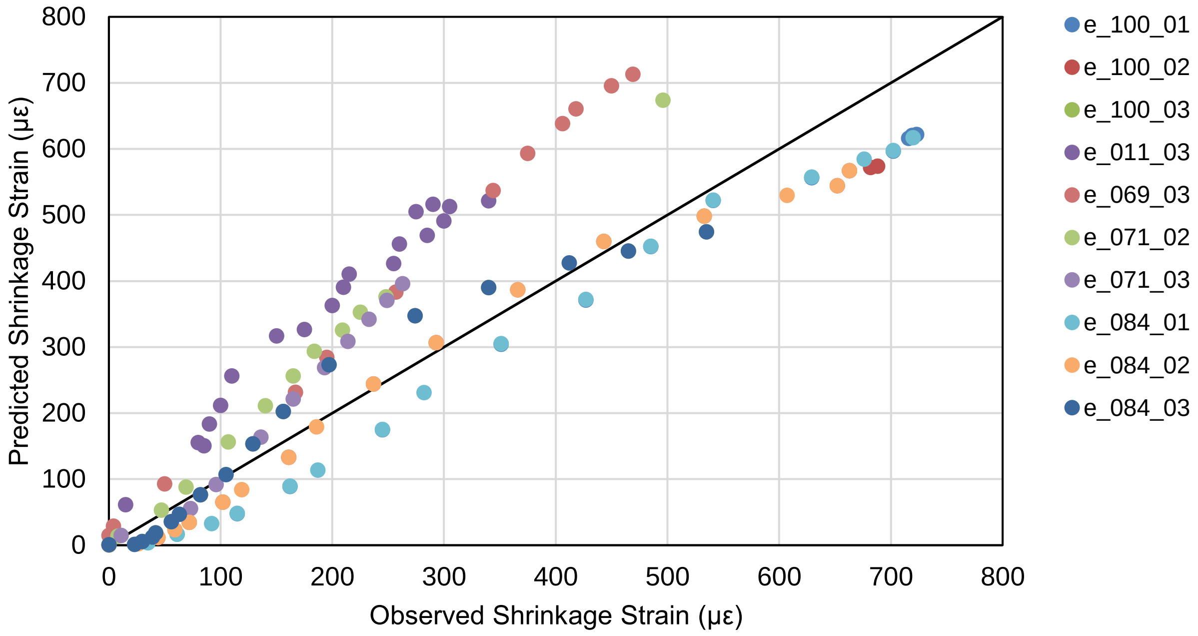

Figure 2.1. Calibrated AASHTO shrinkage model performance

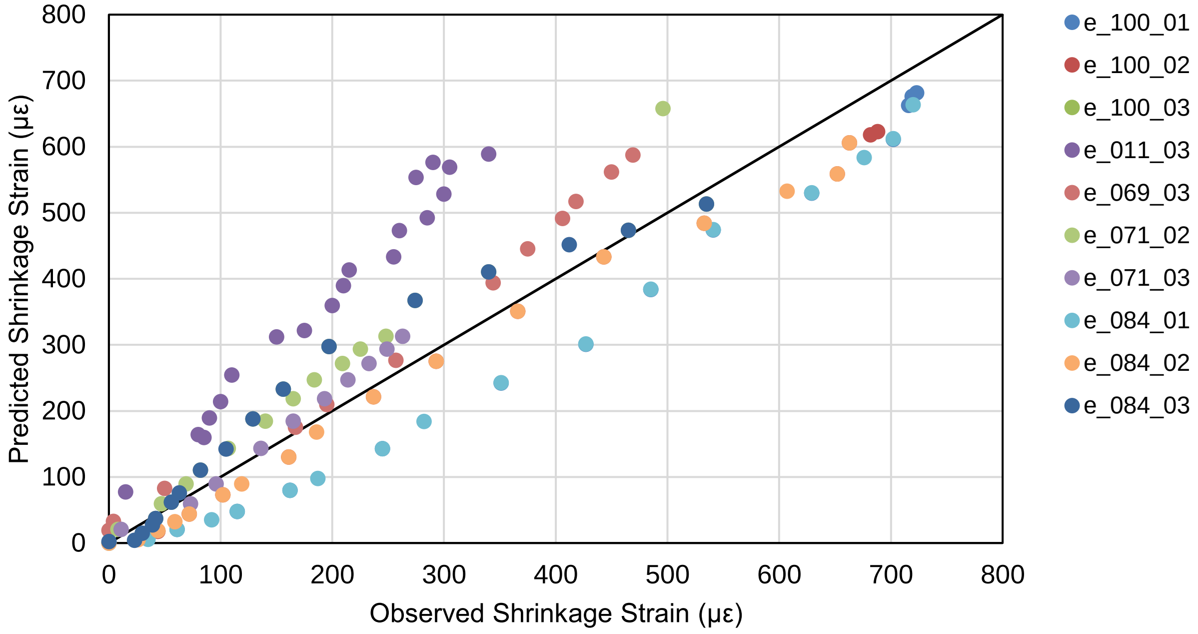

Figure 2.2. Calibrated ACI shrinkage model performance

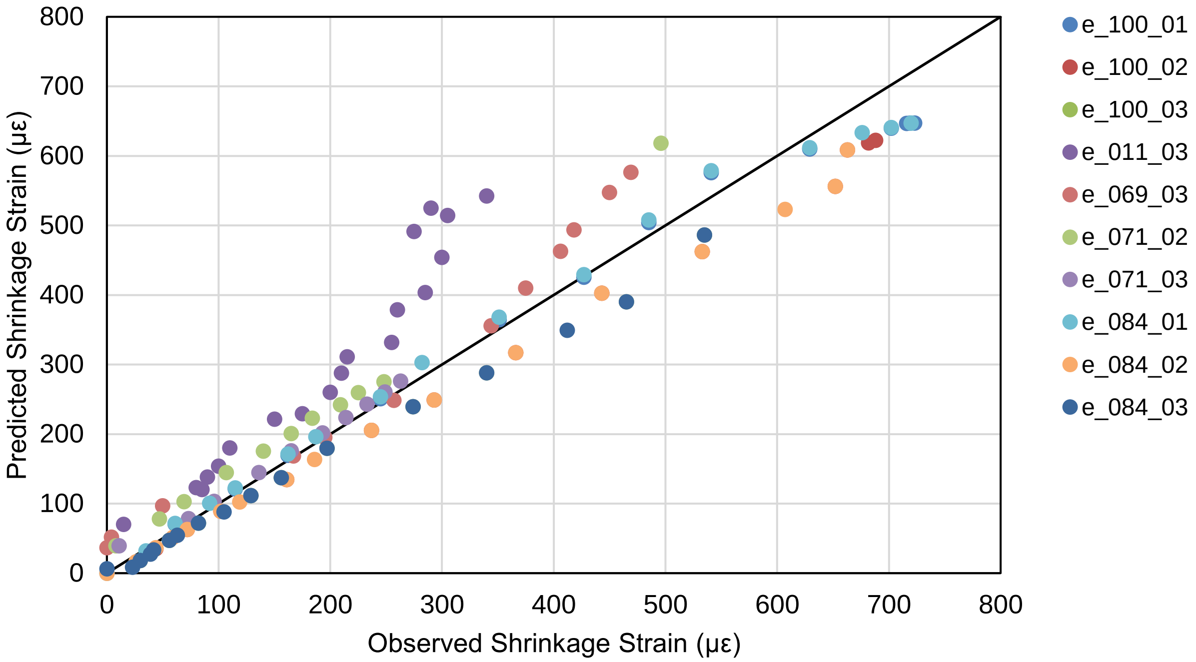

Figure 2.3. Calibrated B3 shrinkage model performance

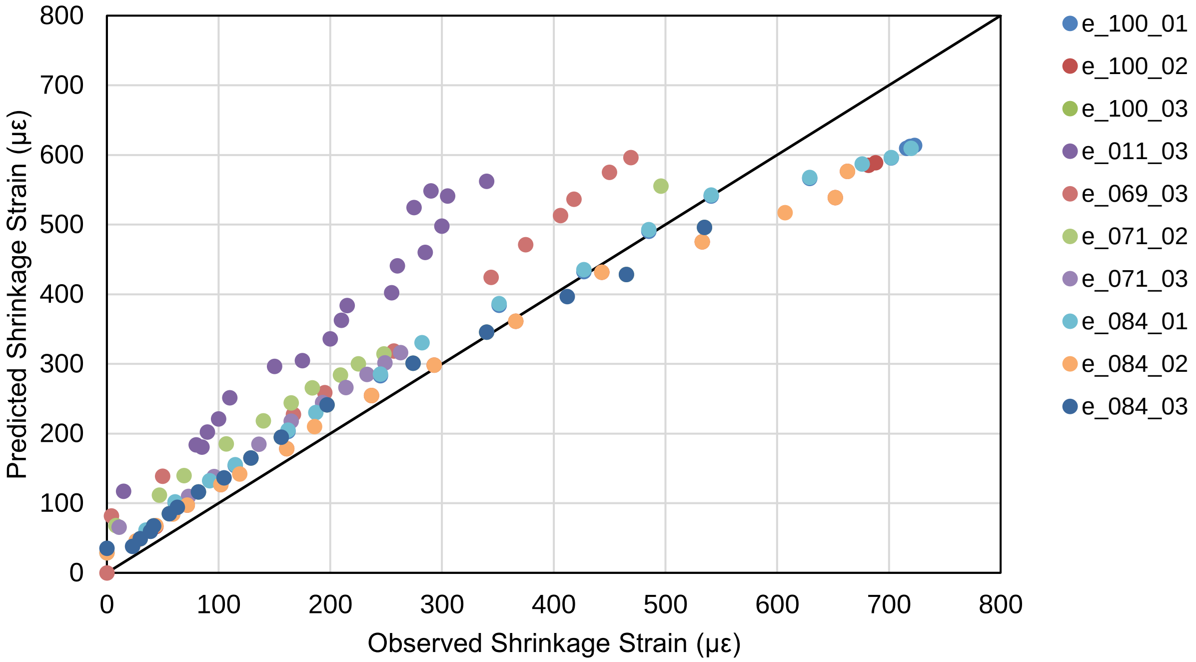

Figure 2.4. Calibrated CEB shrinkage model performance

The final calibration factors affecting the ultimate shrinkage strain for each model were 1.00, 1.20, 1.20, and 1.15 for the AASHTO, ACI, B_3, CEB models, respectively. These values were obtained through an iterative approach to achieve the best match between the models and recorded data. The calibration factors affecting time development were found to barely differ from unity among the models.

The coefficient of determination was used to measure the performance of the models by quantifying the correlation between the predicted and recorded values for each model. A perfect match between a model and recorded values would lead to a coefficient of determination (r^2) of 1.0. As the predicted values of a model begin to differ from the recorded values, the r^2 value will decrease. The B_3 model was found to perform the best of all the shrinkage models considered. Overall, the r^2 value between the predictions of the B_3 model to the recorded data was 0.91. The remaining models had r^2 values of 0.80, 0.79, and 0.75 for the ACI, AASHTO, and CEB models, respectively.

Additionally, r^2 values were calculated over certain periods for each model. This allowed insight into how the models behaved during just the early-age period or long-term period of shrinkage. The early-age period was the first 30 days of a specimen being exposed to drying and the long-term period was any time after the first 90 days of being exposed to drying. During the early period, the models achieved r^2 values of 0.99, 0.96, 0.95, and 0.85 for the B_3, AASHTO, ACI, and CEB models, respectively. During the long-term period, the models achieved r^2 values of 0.87, 0.76, 0.75, and 0.69 for the B_3, CEB, ACI, and AASHTO models, respectively.

Compressive Creep

The creep models were calibrated for compressive creep with experimental data from the ITI-NU database. Experiments from the ITI-NU database were chosen based on how well their mix designs, curing types, curing durations, environmental conditions, and age of concrete at the start of loading matched to that of frame piers.

For concrete mixtures, the selected experiments must have matched reasonably well with Class A concrete specified by AASHTO (AASHTO 2012). For curing, the selected samples must have used moist curing and been allowed to cure for at least two full days. For relative humidity, the selected experiments must have had a relative humidity between 50% and 80% and been exposed to a constant temperature around 68°F (20°C).

Twenty experiments from the ITI-NU database were selected based on these criteria and used to calibrate the creep models. The most notable properties of each experiment selected are presented in Table 2.2.

Table 2.2. ITI-NU database experiments used to calibrate and compare creep models

Database File	w/c	a/c	Cement (kg/m^3)	f_{c28} (MPa)	2VS (mm)	t_0 (day)	Humidity (%)	Stress (MPa)
c_011_08	0.45	5.392	345	35.3	100	28	65	14.22
c_017_01	0.49	4.814	350	33.9	35	7	50	4.91
c_017_02	0.49	4.814	350	33.9	35	21	50	4.91
c_017_05	0.49	4.814	350	33.9	35	7	50	9.81
c_017_06	0.49	4.814	350	33.9	35	21	50	9.81
c_017_07	0.49	4.814	350	33.9	35	28	50	9.81
c_017_26	0.49	4.814	350	33.9	35	28	35	9.81
c_017_27	0.49	4.814	350	33.9	35	28	50	9.81
c_017_28	0.49	4.814	350	33.9	35	28	75	9.81
c_043_02	0.41	5.587	332	40.9	100	28	65	9.4
c_044_01	0.399	5.595	343	27.9	75	28	50	8.83
c_058_01	0.5	6.3	300	29.2	75	28	60	14.71
c_058_03	0.44	5.266	360	37.8	75	7	60	17.66
c_058_04	0.47	5.232	375	39	75	17	60	17.66
c_058_07	0.5	6.3	300	29.2	75	28	60	14.71
c_058_08	0.5	5.314	350	33.6	75	28	60	9.81
c_058_09	0.47	5.232	375	39.4	75	7	60	17.66
c_058_12	0.4	4.525	400	38.9	75	28	60	15.7
c_069_05	0.45	5.405	353	23.9	75	28	65	6.77
c_069_06	0.45	5.405	353	23.9	75	28	65	12.32

The selected experiments for creep calibration and comparison had an average 28-day compressive strength of 4.86 ksi (33.5 MPa) and the average age of the concrete at the start of loading of 22.6 days. Additionally, the selected creep experiments had an average relative humidity of 57%.

Each model was calibrated for creep through the same means used for the shrinkage models: applying a factor to the ultimate value of creep of each model and applying a factor to the time development component of each model. These two calibration factors were applied to models to adjust the long-term progression of creep and the rate of creep development of the models. The ACI model already had two built-in coefficients that served as the factor applied to the time component. However, the remaining models had no such factor already well-defined, so a factor was inserted into each model mimicking that of the ACI defined factors. The calibration factors were calibrated such that each model had only one value for each factor that covered every experiment (i.e., models with a single value for each calibration factor).

For each model, data from the selected experiments were plotted against the predicted values of the calibrated models. A data point perfectly matched between the model and experiment if it landed on the line with a slope of one originating from the origin. A graphical comparison of the calibrated models to data from the ITI-NU database is presented in Figure 2.5 through Figure 2.8.

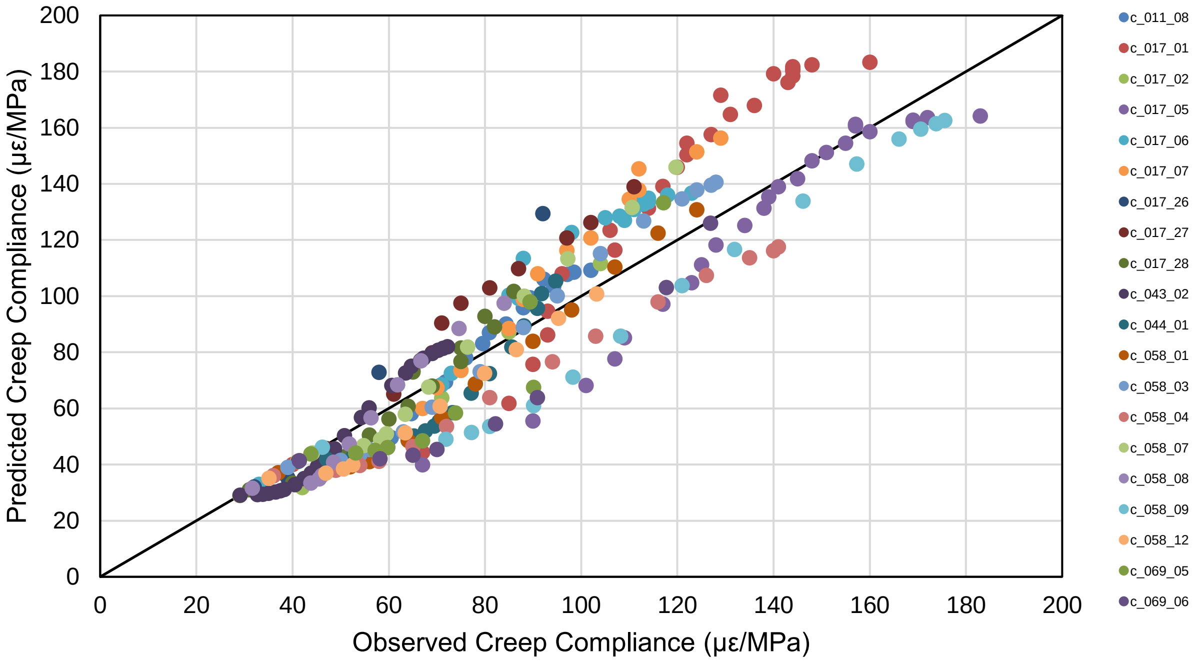

Figure 2.5. Calibrated AASHTO creep model performance

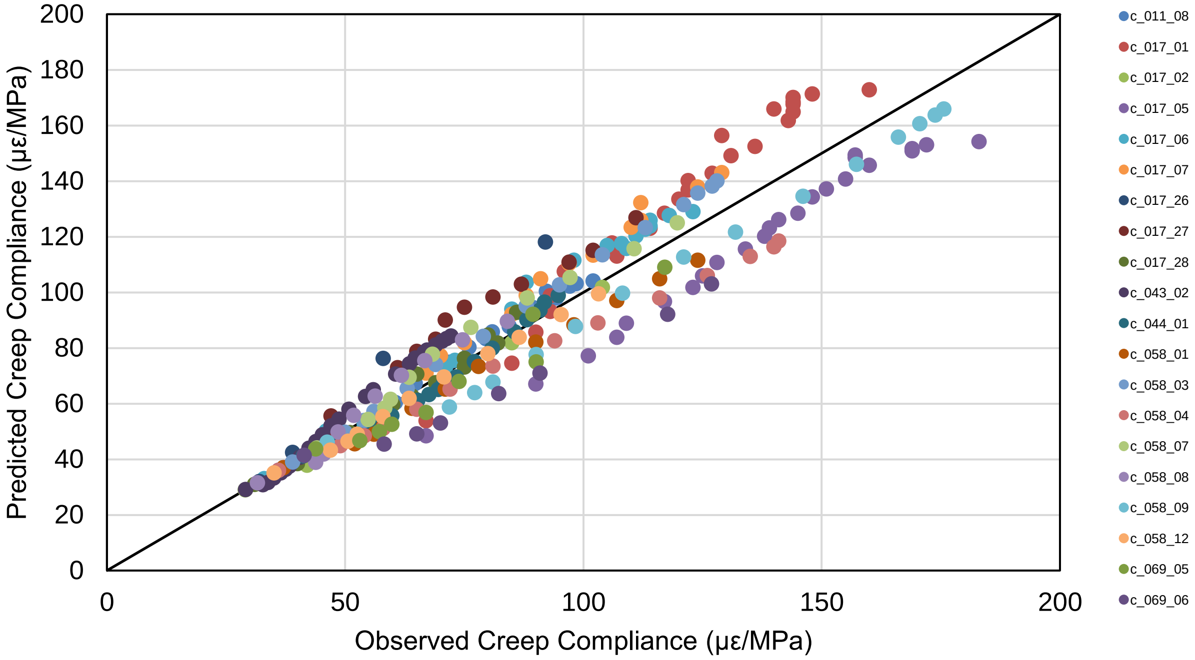

Figure 2.6. Calibrated ACI creep model performance

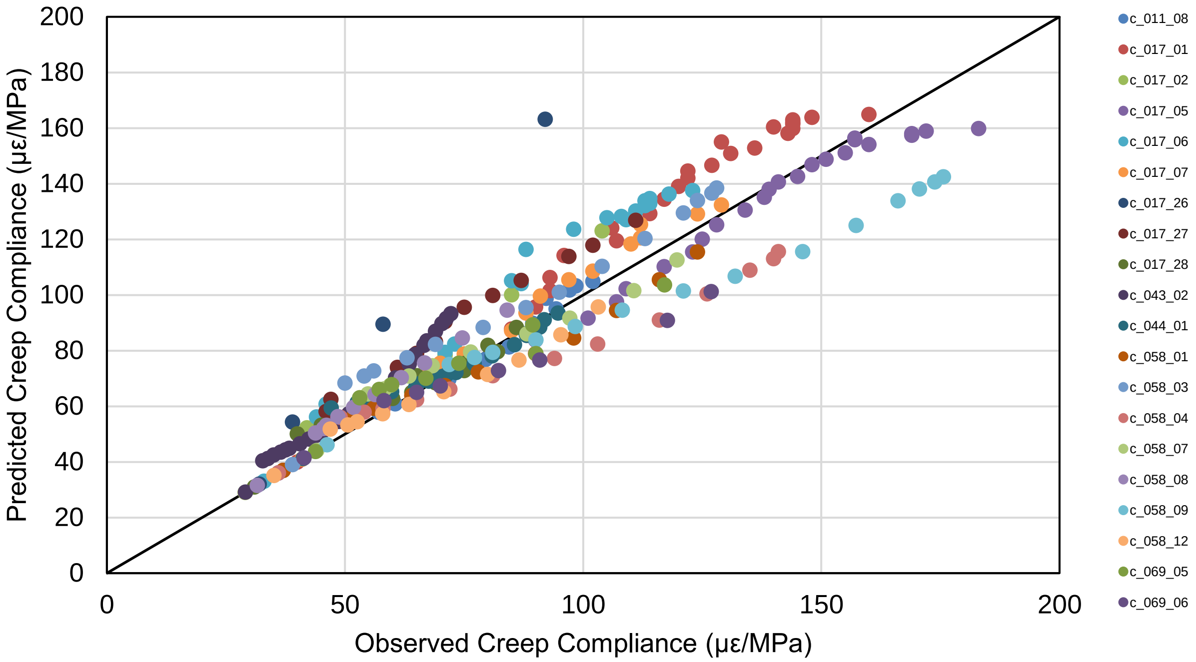

Figure 2.7. Calibrated B_3 shrinkage creep performance

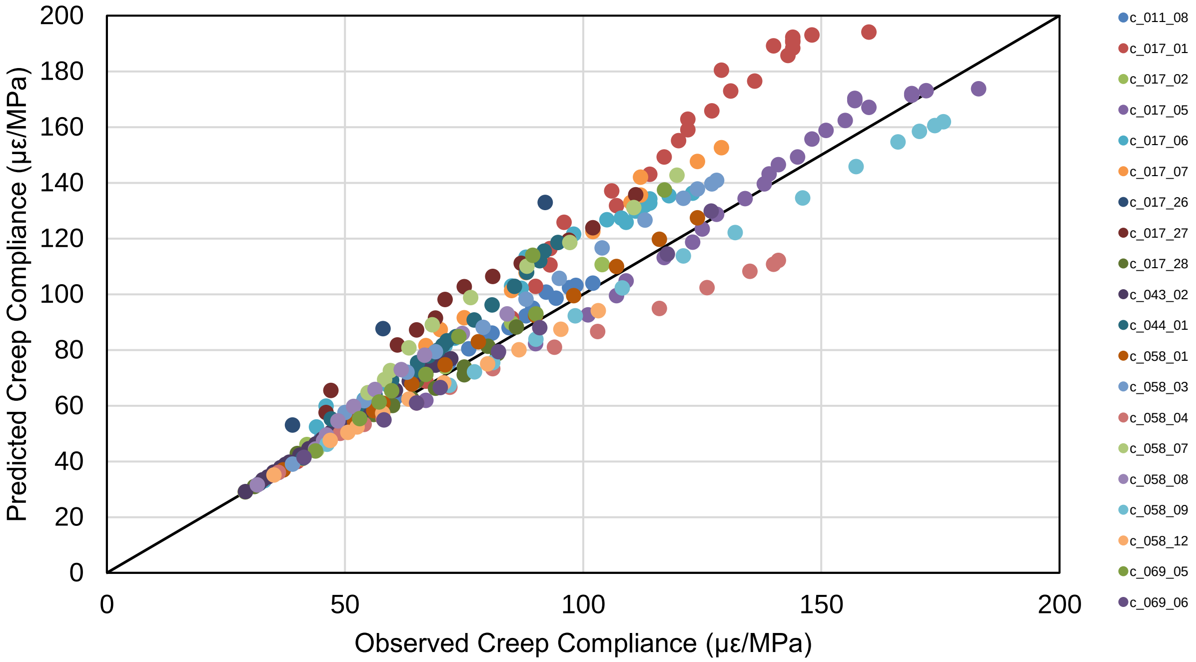

Figure 2.8. Calibrated CEB creep model performance

The final calibration factors affecting the ultimate creep for each model were 1.80, 1.40, 0.80, and 0.85 for the AASHTO, ACI, B_3, and CEB models, respectively. The calibration factors affecting time development were found to barely differ from unity among the models. As with the shrinkage model analysis, the r^2 value was used to measure the performance of the models by quantifying the correlation between the predicted values and recorded values for each model. A perfect match between a model and recorded values would lead to an r^2 value of 1.0. As the predicted values of a model began to differ from the recorded values, the r^2 value would decrease.

The ACI model performed the best of all the creep models considered. Overall, the r^2 value between the predictions of the ACI model to the recorded data was 0.91. The remaining models had r^2 values of 0.87, 0.86, and 0.85 for the AASHTO, B_3, and CEB models, respectively. Additionally, r^2 values were calculated over certain periods for each model. This allowed insight into how the models behaved during just the early-age period or long-term period of shrinkage. The early-age period was the first 30 days after a specimen was loaded and the long-term period was any time after the first 90 days since being loaded. During the early-age period, the models achieved r^2 values of 0.95, 0.94, 0.94, and 0.89 for the ACI, CEB, B_3, and AASHTO models, respectively. During the long-term period, the models achieved r^2 values of 0.90, 0.87, 0.83, and 0.82 for the ACI, AASHTO, B_3, and CEB models, respectively.

Model Selection

Models were selected primarily based on their ability to predict and match recorded test data. In that regard, the B_3 and ACI models were identified as the most performant models for the application of this research. The B_3 model clearly predicted shrinkage strain most accurately. However, for the early-age period, which is crucial to shrinkage sensitive structures, the ACI and AASHTO models performed comparable to the B_3 model with r^2 values of 0.96 and 0.95, respectively, compared to the 0.99 r^2 value of the B_3 model.

For creep, the ACI model performed best, with an overall r^2 value of 0.91. The remaining three models all had similar r^2 values, with no model clearly lacking in accuracy to the others. However, the AASHTO model had a notably lesser r^2 value of 0.89 over the early-age period compared to the other models, which had values of 0.95, 0.94, and 0.94 for the ACI, CEB, and B_3 models, respectively. It is important to note that the ACI shrinkage model relied on slump as its only input regarding water content of the concrete mix. This led to the ACI model being the only model considered that did not use the 28-day mean compressive of the concrete, which also can be related to water content. Given that water content is known to affect the magnitude and rate of shrinkage and creep, water content is a crucial factor to consider in a shrinkage and creep model.

However, the ITI-NU database does not report concrete slumps. Therefore, a uniform slump of 3.5 in. was assumed for all experiments considered. This assumption put the ACI shrinkage model at a disadvantage, as it caused the ACI model to consider all experiments to have the same water content, while the other models consider unique water content for each experiment. However, even with this disadvantage, the ACI shrinkage model compared favorably with the other models.

Simplicity is another factor considered when selecting a shrinkage and creep model. The model selected for this research needed to be programmed to run with an FE analysis. The more complicated a model is, the more complicated the program must be, which can cause complications during debugging. Compared with the B_3 model, the ACI model was clearly the simpler of the two top-performing models. While maintaining the second highest number of inputs, the ACI model had fewer steps and simpler calculations compared with the B_3 model, which also had the highest number of inputs. In this regard, the ACI model was the best model to develop into code.

For this research, the ACI shrinkage and creep model was selected to predict shrinkage and creep. Similar studies investigating shrinkage and creep have used the ACI shrinkage and creep model and have achieved accurate results (Purani 2013, Kasera 2014).

Further Calibration

Despite the selected shrinkage and creep model already being calibrated for unrestrained shrinkage and compressive creep through data from the ITI-NU database, other aspects of shrinkage and creep needed to be calibrated. First, the model was compared and calibrated to field-collected data for unrestrained shrinkage and compressive creep. This allowed the model to be compared to actual concrete that is used in frame piers. This comparison was important to this research as the only structures of concern in this research were frame piers.

Furthermore, the model needed to be calibrated for tensile creep and restrained shrinkage. These two phenomena needed to be captured by the model for the model to be used in a comprehensive FE analysis. Since restrained shrinkage results in a time-varying load, the effect of aging needed to be considered for the model to predict creep accurately under such loading.

Field Data Comparison

The calibrated shrinkage model was validated by comparing the model to the recorded shrinkage of concrete samples collected from the field. The samples were collected from the construction site of a frame pier in Sioux City, Iowa, during the pouring of the cap beam. The collected samples were composed of three rectangular prism specimens that were transferred from the field to a lab environment after allowing the samples to set in the field for one day. The samples were exposed to drying in a controlled environment to monitor unrestrained shrinkage. A comparison between the model and recorded shrinkage is presented in Figure 2.9.

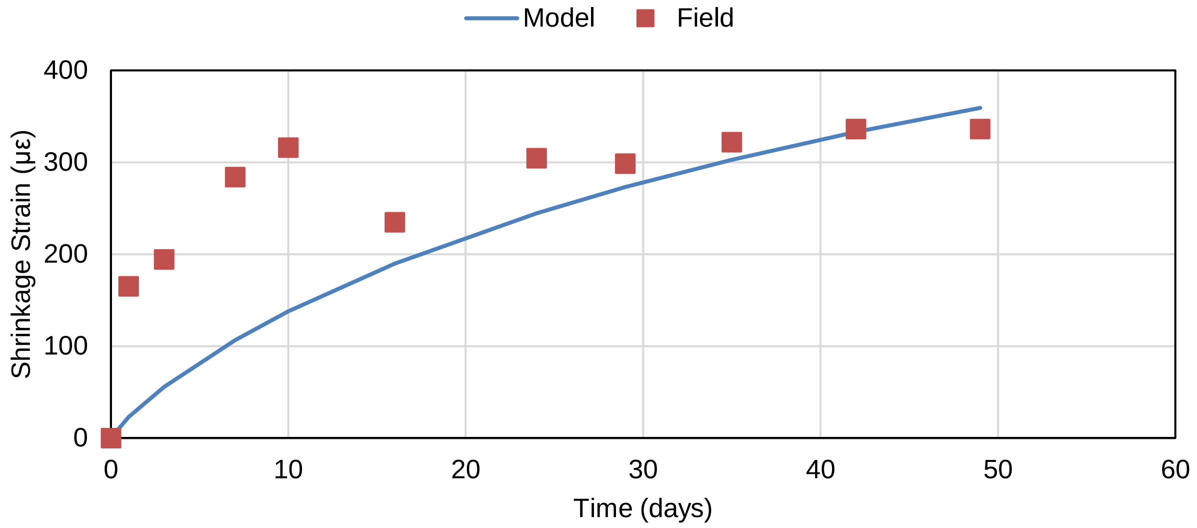

Figure 2.9. Calibrated shrinkage model compared to field samples

As seen in Figure 2.9, the model reasonably matched the recorded shrinkage behavior of the field samples, thus affirming that the model was calibrated appropriately for use with frame piers.

The calibrated creep model was further validated by comparing the model to the recorded creep behavior of concrete samples collected from the field. The field samples were collected from the construction site of a frame pier in Sioux City, Iowa, during the pouring of the cap beam. Six cylindrical specimens were transferred from the field to a lab environment to monitor creep. The samples were subjected to a sustained compressive load and their lengths were recorded regularly. A comparison between the model and recorded creep is presented in Figure 2.10.

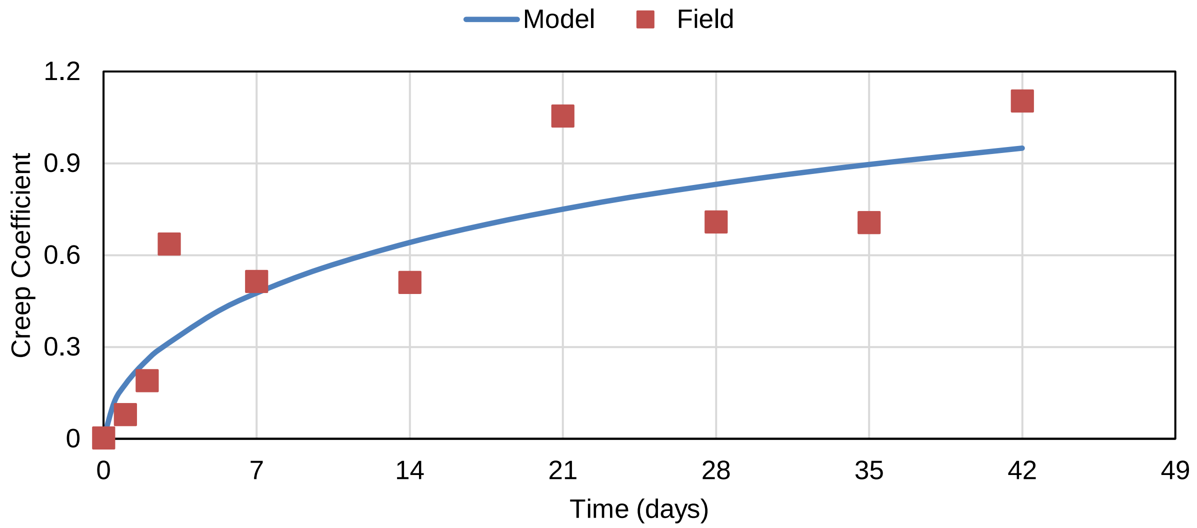

Figure 2.10. Calibrated creep model compared to field samples

As seen in Figure 2.10, the model appropriately matched the recorded creep behavior of the field samples, thus affirming that the model was calibrated appropriately for use with frame piers.

Tensile Creep

In comparison to the amount of concrete compressive creep tests available (i.e., the 621 tests available in the ITI-NU database alone), there are very few concrete tensile creep tests. Experimental data from multiple studies that investigated tensile creep were selected to calibrate the current model (Khan et al. 2017, Bissonnette and Pigeon 1995, Østergaard et al. 2001). As the concrete properties varied between the studies, the concrete material and creep model were adjusted accordingly using the data provided by the studies. If information necessary to the model was missing from a study, a common value was used.

Bissonnette and Pigeon (1995) investigated uniaxial tensile creep with a focus on the effects of water-cement ratio, cement type, and age of loading. Three different mix designs were considered in the study. However, only one mix is selected to calibrate the model to avoid considering mixes that use fiber reinforcement or high strength cement. Furthermore, experiments with a loading age of 1 day are not considered as they differ to much from the conditions of frame piers. The specimens used by Bissonnette and Pigeon (1995) are prismatic with a length of 27.56 in. (700 mm) and exposed to a constant relative humidity of 50%.

Østergaard et al. (2001) investigated tensile creep of ordinary Portland cement concrete with a focus on the effects of the age of loading, stress-strength ratio, and water-cement ratio. They considered three different mix designs. However, only the results from the mix design with a water-cement ratio of 0.5 were used to calibrate the model for tensile creep, as the other mixtures used superplasticizers which are not commonly used in frame piers. This is due to this mix being comparable to the AASHTO-specified mix used in frame piers and because this mix was tested for an age of loading similar to what frame piers would experience due to self-weight and shrinkage (i.e., more than two days). The specimens used by Østergaard et al. (2001) are bone-shaped and exposed to a constant relative humidity of 50%.

Khan et al. (2017) investigated the long-term (i.e., weeks and months) progression of tensile creep under sustained loading less than 50% of the tensile strength of the concrete. Khan et al. used a single mix design with a water-cement ratio of 0.55. The results from the specimens loaded at an age of two days were used to calibrate the model for tensile creep. The specimens were bone-shaped and exposed to a constant relative humidity of 50%.

To calibrate the model for tensile creep, only the factor applied to the ultimate creep coefficient was altered, while the remaining previously calibrated constants of the creep model were unchanged. The ultimate creep coefficient factor was tuned specifically for each experiment and then averaged for use in the model. Figure 2.11 through Figure 2.13 show the various calibrated tensile creep models in comparison to each experiment.

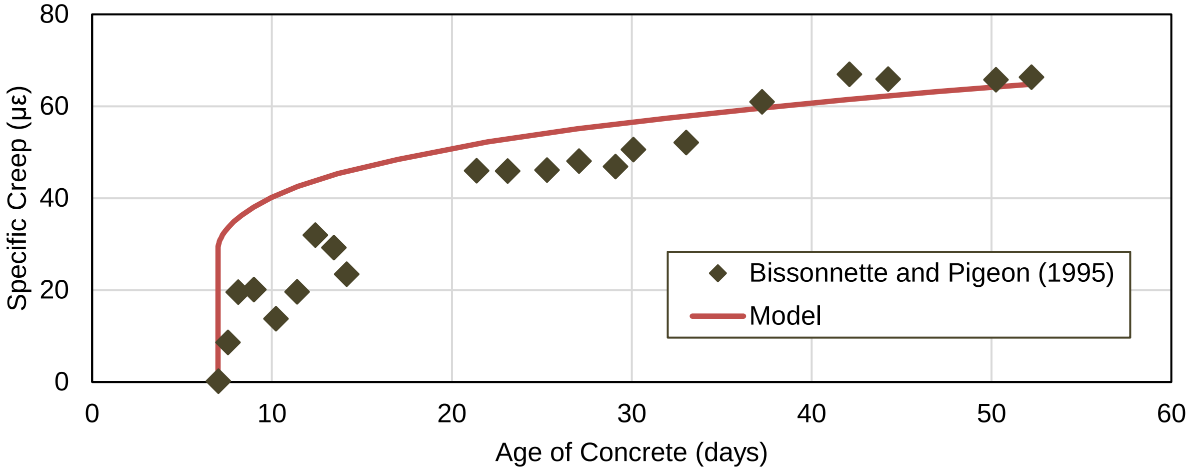

Figure 2.11. Experimental data from Bissonnette and Pigeon (1995) in comparison to the calibrated model

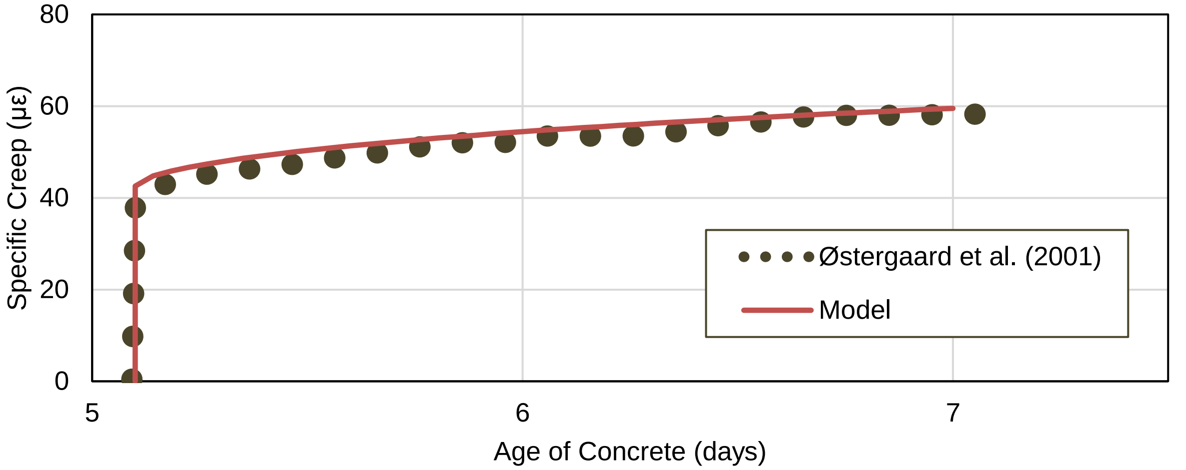

Figure 2.12. Experimental data from Østergaard et al. (2001) in comparison to the calibrated model

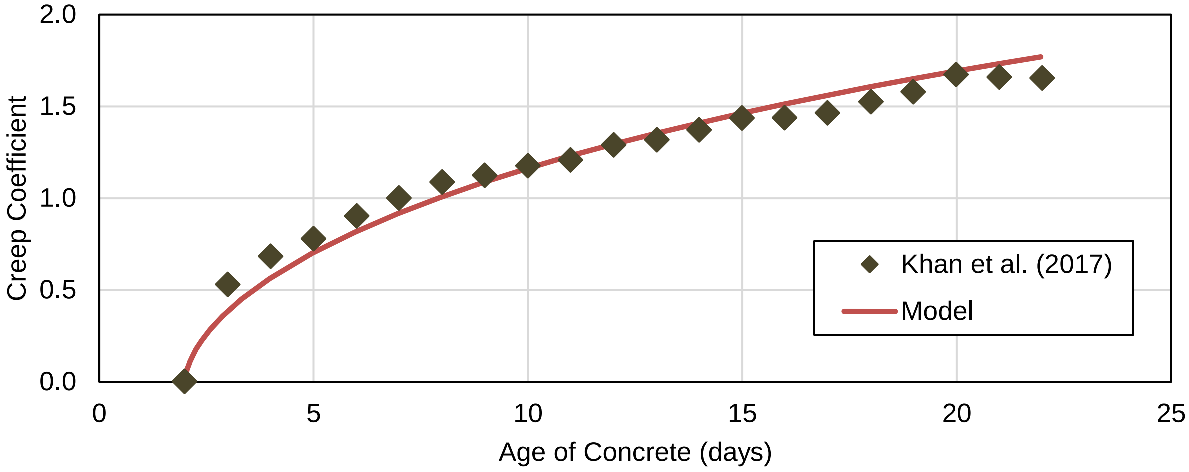

Figure 2.13. Experimental data from Khan et al. (2017) in comparison to the calibrated model

As expected, the factor applied to the ultimate creep coefficient for tensile creep was greater than that of compressive creep. Additionally, altering only the factor applied to the ultimate creep coefficient was sufficient to match the model to experimental data. The calculated calibration factor applied to the ultimate creep coefficient to account for tensile creep in the model was 1.8.

Aging Coefficient

Creep curves, such as those predicted by the ACI model, only represent the creep response due to a constant, sustained load applied at a known time. However, creep models tend to overestimate creep if the load is variable. This is due to the models not accounting for the aging of the concrete due to creep that has already occurred. This aging effect is especially critical in loads caused by restrained shrinkage, as these loads tend to gradually increase with time. Therefore, a creep model such as the ACI 209R must be modified to account for the aging of the concrete due to previously experienced creep.

Prior groundwork by Zdeněk Bažant and Heinrich Trost led to the development of a method known as the age-adjusted effective modulus method, which can account for the aging concrete due to creep. In this method, the aging effect of the concrete is captured by reducing the creep coefficient with time by introducing an aging coefficient. The aging coefficient depends on the age of the concrete and the age of the concrete at the beginning of loading (Bažant and Kim 1979). An empirical method to calculate the aging coefficient can be obtained from equations 2.28-2.31 (Gilbert 1988).

$$\chi(t,\tau_o) = 1 - \frac{(1-\chi^*)(t-\tau_o)}{20+(t-\tau_o)} \qquad (2.28)$$

$$\chi^* = \frac{k_1\tau_o}{k_2+\tau_o} \tag{2.29}$$

$$k_1 = 0.78 + 0.4e^{-1.33\phi^*(\tau_o)} \tag{2.30}$$

$$k_2 = 0.16 + 0.8e^{-1.33\phi^*(\tau_o)} \tag{2.31}$$

where $\chi(t, \tau_o)$ is the aging coefficient at any age t in days due to a variable load beginning at age τ_o in days, χ^* is the final aging coefficient, k_1 and k_2 are factors depending on creep, and $\phi^*(\tau_o)$ is the final creep coefficient for a load applied at age τ_o. The use of an aging coefficient is common in models containing restrained shrinkage and is thus used in this study (Khan et al. 2015, Khan et al. 2017, Gilbert 1990).

Restrained Shrinkage

Restrained shrinkage produces a tensile stress that varies with time. This contrasts with the tensile creep experiments which maintained a constant stress. Therefore, calibrating for restrained shrinkage went beyond the calibration already performed for unrestrained shrinkage and tensile creep. For this calibration, the aging coefficient needed to be considered with the model.

Khan et al. (2015) investigated the behavior of reinforced concrete subjected to a sustained tensile load. The specimens consisted of prismatic concrete prisms with a length of 15.75 in. (400 mm) and a single steel reinforcement bar with a diameter of 0.47 in. (12 mm) embedded at the center of the prism. The mix design had a water-cement ratio of 0.55 and the specimens were loaded and restrained at an age of two days. The specimens were exposed to a constant relative humidity of 50%.

Altoubat and Lange (2001) also performed restrained shrinkage experiments. However, the experiments by Altoubat and Lange were fully restrained at an age of 14 hours, which is not enough curing for the ACI model predict accurately. Thus, the calibration for restrained shrinkage was performed using the results from Khan et al. (2015).

To account for the gradual increase in stress that is related to restrained shrinkage, an aging coefficient was considered with the creep model. An aging coefficient was used and calculated according to Gilbert (1988). With minor modifications to the calibration factors determined from unrestrained shrinkage, compressive creep, and tensile creep experiments to represent the concrete mix and environmental conditions of the experiment, the model could accurately match the experimental data provided by Khan et al. (2015) without any modifications to the aging coefficient defined by Gilbert (1988). Therefore, no additional modification was performed on the model or aging coefficient given the model was appropriately calibrated for restrained shrinkage. The results of the model are compared to data from the restrained shrinkage experiment by Khan et al. (2015) in Figure 2.14.

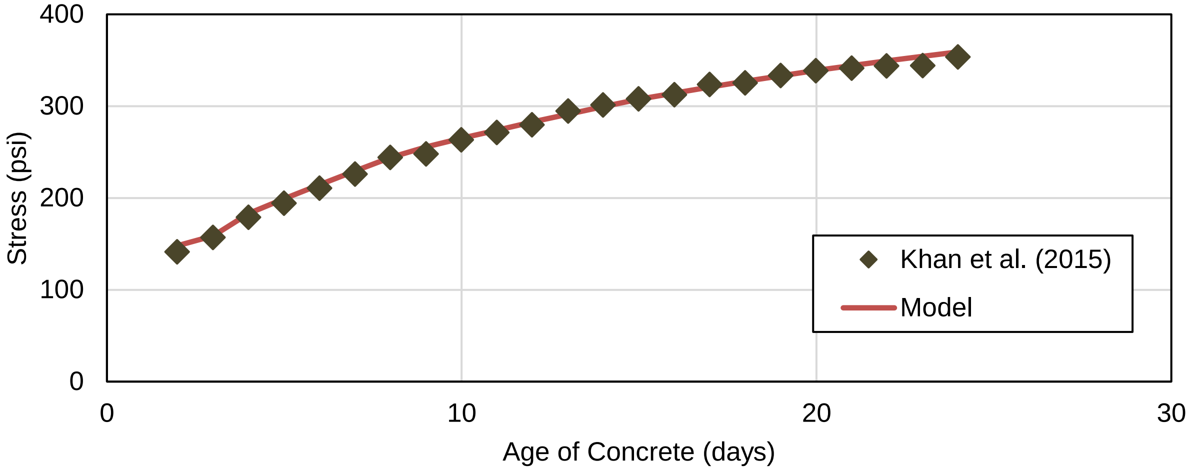

Figure 2.14. Experimental data from Khan et al. (2015) in comparison to the calibrated model

Summary

The AASHTO, ACI, B_3, and CEB shrinkage and creep models were examined to determine an appropriate model for use in this study. All of these models shared the same fundamental limitations in terms of their outputs, so the decision of which model to use relied heavily on the performance of the models. The performance of each model was quantified by comparing the model outputs to data from the ITI-NU shrinkage and creep database that resembles the environmental and concrete mix properties of frame piers.

For shrinkage, the two best models were the B_3 model and the ACI model with r^2 values of 0.91 and 0.80, respectively. For creep, the two best models were the ACI model and B_3 model with r^2 values of 0.91 and 0.87, respectively. The ACI model was ultimately selected for this study due to its simplicity over the B_3 model. The simplicity of a model is advantageous when developing a computer program of the model. Furthermore, since the lowest r^2 value of any model analyzed was 0.75, it was likely that each model would produce reasonable results for this study.

The selected ACI creep model was calibrated for tensile creep using available data in the literature (Khan et al. 2017, Bissonnette and Pigeon 1995, Østergaard et al. 2001). Furthermore, an aging coefficient was applied to the ACI creep model to account for variable loading. Through comparing the model outputs to data from a restrained shrinkage experiment, the ACI model was determined to properly predict strain due to variable loading with the aging coefficient applied (Khan et al. 2015).

The ACI shrinkage and creep model was calibrated for free shrinkage, compressive creep, tensile creep, and creep under variable loading (i.e., restrained shrinkage). The calibrated model was proven to predict each of these phenomena well by comparing the outputs of the model to data of experiments that resembled the concrete mixes, environmental factors, and loading associated with frame piers. This calibrated model was used in this study in tandem with FE analysis software to simulate the effects of shrinkage and creep on frame piers.

CHAPTER 3. FIELD INSTRUMENTATION AND DATA

Inspections

Prior to instrumenting bridges for this study, several frame piers were selected in Iowa for visual inspection. The bridges were selected based on the expected susceptibility to the temperature and shrinkage effects of their frame piers. The ratio of the length of a frame to the height of the frame was used to predict susceptibility, with an understanding that the larger the ratio, the more susceptible the frame is to temperature and shrinkage effects (Badrah and Jadid 2014).

The frame piers of the bridges were purposefully selected to vary in length, column height, column shape, foundation type, and age. The details of the inspected frame piers are summarized in Table 3.1.

Table 3.1. List of bridges inspected

Year Built	Pier Cap Length (ft)	No. of Columns	Column Height (ft)	Skew (deg)	No. of Piers	Foundation Type	Location
2016	111	3	11	35	5	Drilled Shaft	Sioux City
2015	96	3	10.5	37	5	Drilled Shaft	Sioux City
2005	90.2	5	15	11	2	Piles	Des Moines
2004	89.6	5	15.4	0	2	Piles	Des Moines
1966	42.3	3	14.9	5	2	Piles	Ames
1966	42.3	3	14.9	5	2	Piles	Ames
2016	147.5	7	23.5	55	4	Drilled Shaft	Council Bluffs
2016	138	7	16.5	55	4	Drilled Shaft	Council Bluffs
2002	119	6	23	45	2	Drilled Shaft	Ankeny

The connections between columns and cap beams were given special attention during these visual inspections. The column bases were also given special attention, when possible, given that the bases of most columns are backfilled. Very few of the frame piers showed any signs of damage. An example of a frame pier inspected in Sioux City, Iowa, is provided in Figure 3.1.

Figure 3.1. Inspected frame pier in Sioux City, Iowa

Any recorded damage was minor and attributed to construction issues and not to temperature and shrinkage effects. These inspections showed that current frame piers in Iowa perform adequately under temperature and shrinkage forces.

Additional frame piers were examined by reviewing Iowa DOT inspection reports. The Iowa DOT performs these inspections biannually to ensure bridges remain in satisfactory condition. Therefore, these reports cover the superstructure of the bridges as well as the substructure. However, only the substructure information of these reports was reviewed for this study.

The inspection reports of several bridges were selected for review based on the high length-to-height ratios of their frame piers. Most of the inspection reports reviewed had no clear indication of damage due to temperature and shrinkage effects. However, two inspection reports noted damage that was likely to be caused or worsened by temperature and shrinkage effects.

The report of one frame pier, located in Dubuque, Iowa, noted cracking origination from the column-cap beam interface, as shown in Figure 3.2.

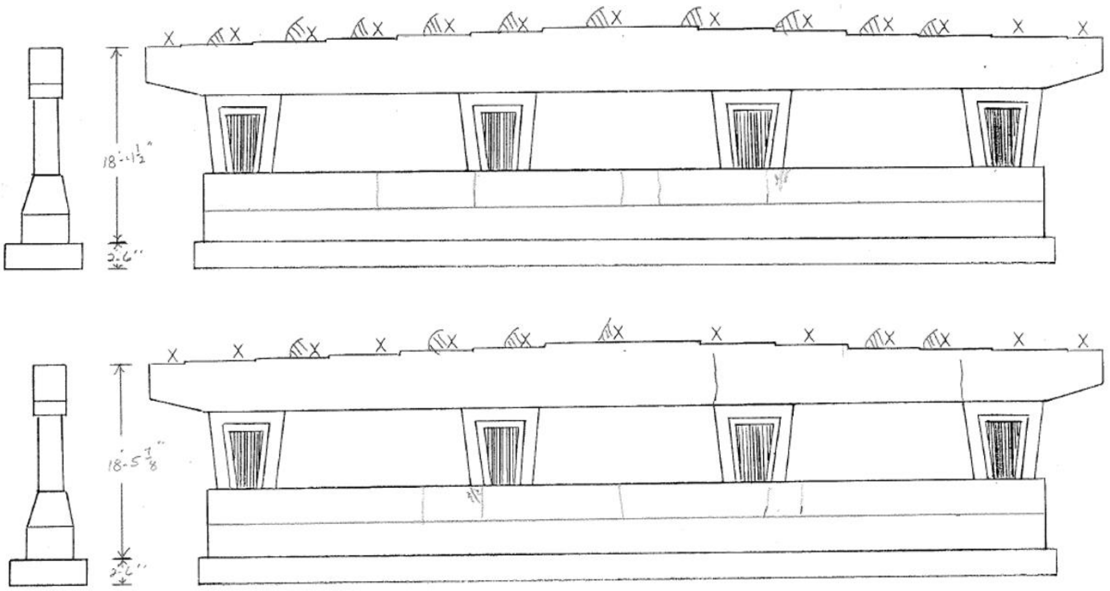

Figure 3.2. Inspection report sketch showing cracking in the cap beam of a frame pier in Dubuque, Iowa

This frame pier not only had a high length-to-height ratio (due in part to an integrated crash wall below the columns), but also had columns shaped and oriented to be stiffer with respect to the in-plane orientation of the frame pier. It is likely that some of the cracks reported were caused or worsened by shrinkage and temperature effects. The cracks in this frame pier occurred within the cap beam and originated from the column-to-cap connections of an exterior and interior column. The cracks did not penetrate the full depth of the cap beam and were small enough to not need repair.

The report of another frame pier, also located in Dubuque, noted cracking in the cap beam above the columns, as shown in Figure 3.3.

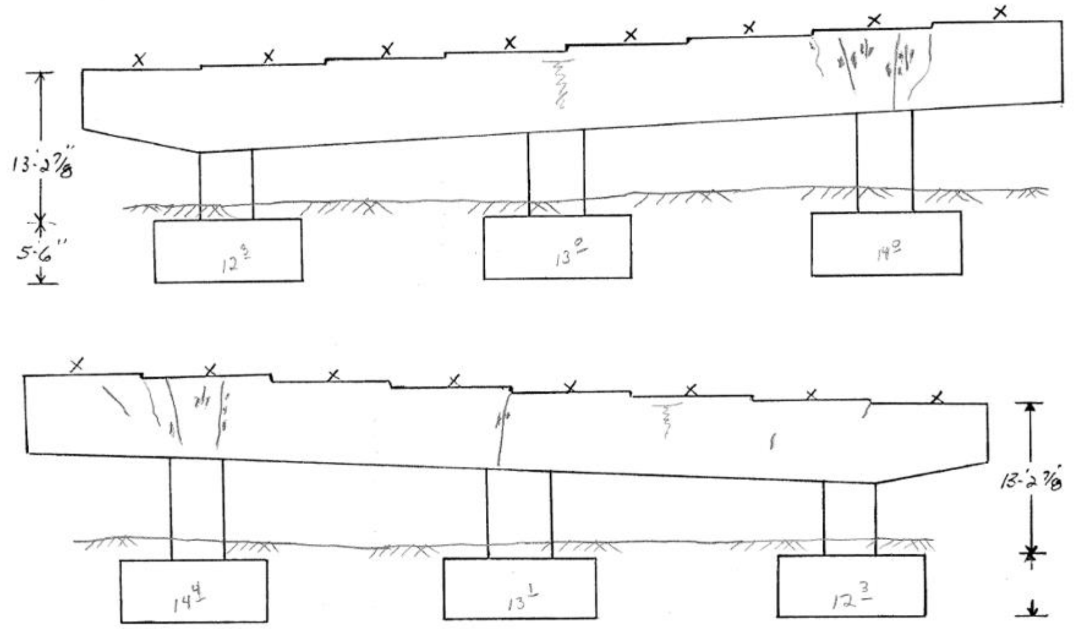

Figure 3.3. Inspection report sketch showing cracking in the cap beam of a frame pier in Dubuque, Iowa

In this case, the cracking was likely due to a combination of gravity loads and temperature and shrinkage effects. Cracks initiating from the top of the cap beam above the columns may be attributed to gravity loads, as negative moment is expected in the cap beams over the columns. However, cracks initiating from the bottom of the cap beam at the columns were likely caused or worsened by shrinkage and temperature effects.

In this frame pier, the inspection sketch noted multiple cracks initiating from the top of the column. Furthermore, two cracks were shown to extend to the bottom face of the cap beam. These two cracks were likely worsened by temperature and shrinkage effects since the bottom of the cap beam is expected to experience compression under gravity loads alone. The cracks were minor enough to not need repair.

Overall, the inspected frame piers appeared to perform adequately with regards to shrinkage and temperature effects. The cracks noted in the inspection reports were minor and did not degrade the structural integrity of the piers. It should be noted that, in addition to the base of the columns, another aspect that a visual inspection could not accurately examine is the foundations of the piers.

While the performed inspections and reviewed inspection reports suggest that frame piers in Iowa are adequately designed for shrinkage and temperature effects, these efforts offer little insight into the actual magnitude and progression of these effects. Instrumenting and collecting data from frame piers in the field would provide such insights. Additionally, field data are essential to accurately calibrate and validate the FE model developed in this study. Field data offers a holistic view of the structural behavior of a frame pier.

Data Collection

Sensor Information

The frame piers of two bridges were instrumented during construction and monitored in this study. The sensors used to monitor these frame piers were the GEOKON Model 4200 Series vibrating wire embedment strain gauges with 6 in. (153 mm) gauge lengths. These sensors are capable of recording both strain and temperature. The manufacturer recommends this sensor for use with bridge structures. The Model 4200 Series can record strain with a resolution of 1 microstrain and a range of 3,000 microstrain.

The sensors were fastened to reinforcing steel bars in accordance with recommendations from the manufacturer, as shown in Figure 3.4.

Figure 3.4. Sensor installation as recommended by manufacturer (left) and as installed in the field (right)

The location of each sensor was selected to capture temperature profiles of the members and the performance of the structure with respect to frame behavior caused by shrinkage and temperature effects. In particular, the ends of the exterior columns and the cap beam near the exterior columns were of most interest. Two sensors were placed on the interior legs of stirrups in the cap beam for each instrumented frame pier to measure the internal temperature of the structure. The remaining sensors were grouped within a member to act like a section cut through the member. All sensors began recording data just before the cap beam of the frame pier was poured and recorded data at a frequency of one reading per hour.

Sensor Installation

The sensors were installed onto the reinforcing steel bars of the frame piers following the manufacturer’s recommendations. This allowed the sensors to essentially record the strain of the rebars.

Given that the columns are erected first, the column sensors were installed first. When the column rebar cages were in place, the column sensors were installed with their cables routed to the tops of the columns and above the column concrete pour. When the cap beam rebar was in place, the cap beam sensors were installed. The sensor wiring was routed down through a conduit in a column. Each wire of each sensor was then connected to a data collection cabinet. A solar panel was also fastened to a column of the frame pier to power the data collection. Data collection began the day the cap beam sensors were installed, which was just prior to the cap beam pour. Data collected prior the cap beam pour were discarded, as further explained in the Data Processing section that follows.

The strain gauges were installed in planes, with each plane being the cross section of either a column or a cap beam. In general, four gauges were used in each plane, with one gauge at each corner. At a minimum, two gauges were used in each plane, with one at each face of the pier. The only exception to this was the gauges located on the inner legs of the stirrups, which were primarily intended to capture the internal temperature of the cap beam.

Data Processing

The values of primary interest of the collected field data were the time and date of each reading, the recorded temperature values of each reading, and the recorded strain values of each reading. Because the concrete and the strain gauges were made of different materials with different thermal coefficients, the recorded strains needed to be adjusted. For example, during the cold season, the steel will contract more than the concrete surrounding it under the same temperature drop. This will lead to more tension being recorded than is realistic. The strain gauge manufacturer provides the following equation (3.1) to correct for this thermal effect.

$$\varepsilon = (R_1 - R_0)B + (T_1 - T_0)(C_1 - C_0) \tag{3.1}$$

where ε is the final corrected strain, R_1 is the current strain reading, R_0 is the initial strain reading, B is a batch calibration factor taken as 0.975 for the model of gauge used, T_1 is current temperature reading, T_0 is the initial temperature reading, C_1 is the coefficient of thermal expansion of the steel gauge taken as 12.2 με per degree Celsius, and C_0 is the coefficient of thermal expansion of the concrete taken as 10.0 με per degree Celsius.

The initial strain and temperature are important inputs needed to correct strain values for temperature effects. These initial values were taken for each sensor one hour after the cap beam is poured. This was done to avoid using unreasonable initial values from when the gauges were exposed to direct sunlight prior to the cap beam being poured. Additionally, these initial values were taken early enough to avoid the effects of heat of hydration.

Data were collected before the initial values were removed, which resulted in the loss of some data in the columns. This loss of data was considered minimal as this removed data was incomplete. It was not feasible to begin recording data prior to the columns being cast on the construction sites. This partially unrecorded and removed early-age data from the columns was inconsequential for this study since the columns experienced no frame behavior prior to the cap beam being cast.

For in-plane forces, a frame can be simplified to a 2D analysis. As in-plane forces were the focus of this study, sensor pairs were averaged together to achieve a similar simplification. This process created 13 different averages from the data of 26 sensors, with each average representing a location on a 2D simplification of the frame pier.

This simplification benefited this study in three ways. First, this approach of averaging sensor pairs reduced the effect of out-of-plane forces caused primarily by contraction and expansion of the bridge superstructure. As the frame pier experienced out-of-plane forces, one sensor experienced tension while the sensor at the opposite face of the frame pier experienced compression. When strains from these gauges were averaged, these effects were canceled out.

Second, this approach of removed localized effects. For instance, if a portion of one face of a frame pier received direct sunlight during the day, averaging the gauges on that face of the frame pier with the corresponding gauge on the opposite face of the frame pier reduced the effects of localized temperature rise and corresponding localized expansion.

Third, this approach also made the collected data easier to understand by halving the number of data points.

A 24-hour moving average was taken of the averaged sensor pair data. This was done for two purposes. First, this process removed the short-term loading effects, such as vehicular loading or wind gusts. Second, this process again made the data easier to interpret, as diurnal fluctuations in temperature and strain were reduced. This was acceptable since concrete is an insulator and effects caused by the temperature changes of a single day or night were minor when compared to longer-lasting weather events.

Instrumentation of the 418 Woodbury Bridge

Bridge Information

The 418 Woodbury bridge, which is in Woodbury County, was the first of two bridges instrumented for this study. This bridge is located in Sioux City, Iowa, and carries the three southbound lanes of I-29 over Hamilton Boulevard (see Figure 3.5).

Figure 3.5. 418 Woodbury bridge

The 418 Woodbury bridge has no skew, which means volumetric changes of the superstructure have a negligible effect on the in-plane forces the frame piers experience. The west pier was instrumented due to its columns being slightly shorter, and thus stiffer, than the east pier. The plan view of the 418 Woodbury bridge is provided in Figure 3.6.

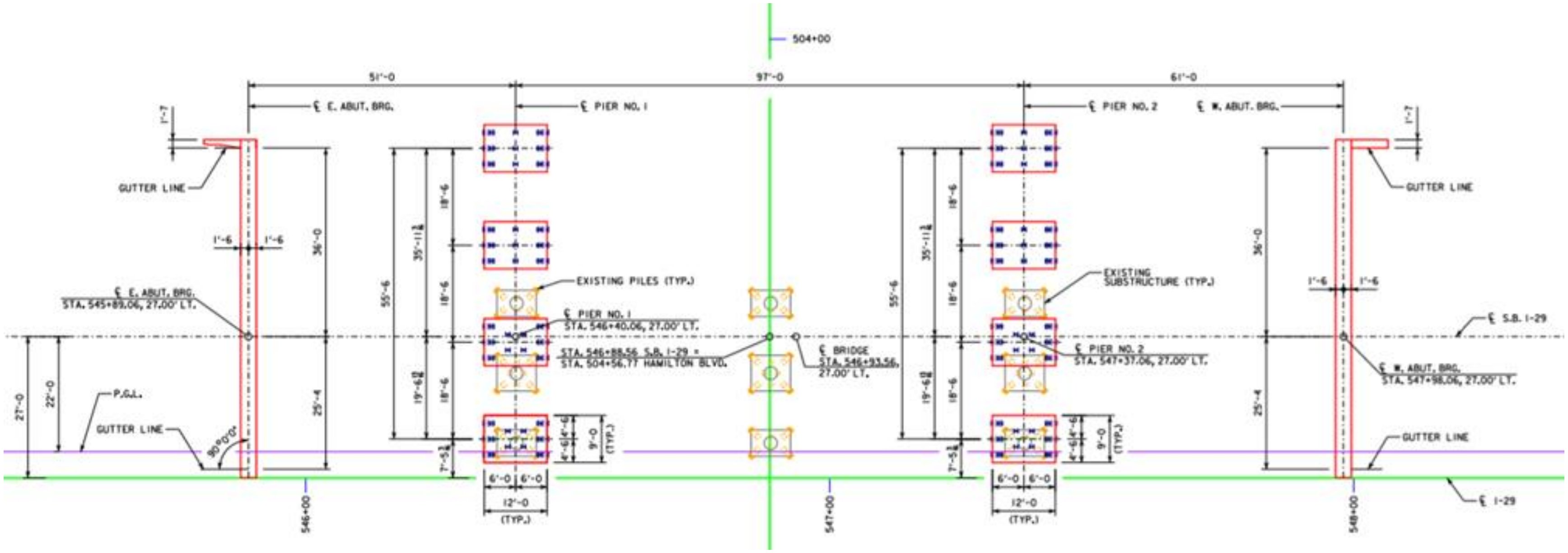

Figure 3.6. Plan view of 418 Woodbury bridge

The instrumented frame pier was composed of four columns 15 ft 7.75 in. tall and spaced at 18 ft 6 in. on center with an overall dimension of 55 ft 6 in. from the center of the exterior column to the center of the exterior column. The columns were all uniform in height and cross section. The column cross section was roughly rectangular, with overall dimensions of about 60 in. by 48 in. The foundation for each column consisted of a 3 ft 9 in. thick pier cap supported by steel piles. The cap beam of the frame pier had a depth of 4 ft and a width of about 4 ft. A unique feature of this frame pier was that the faces on the cap beam and columns were covered in a brick veneer. The instrumented frame pier was directly south of the frame pier of the bridge carrying the northbound lanes of I-29, which gives the visual effect of one single pier. The completed instrumented frame pier of the 418 Woodbury bridge is shown in Figure 3.7.

Figure 3.7. Instrumented frame pier of 418 Woodbury bridge

Construction of the 418 Woodbury bridge took place in the summer of 2019 as summarized in Table 3.2.

Table 3.2. Construction schedule for frame pier of 418 Woodbury bridge

Date	Days after Cap Beam Cast	Construction Activity
6/3/2019	-9	Column Pour
6/12/2019	0	Cap Beam Pour
6/15/2019	3	Cap Forms Removed
7/10/2019	28	Beams Placed on Piers
8/17/2019	66	Deck Pour Begins

The columns were poured early during the week of June 3. The cap beam was poured on June 12. Removal of the cap beam forms began on June 15. The beams were placed on the piers beginning July 10. The deck was poured on August 17. The only significant activity regarding the frame piers after the deck pour was the installation of the barrier rails.

Sensor Placement

The instrumentation arrangement for the 418 Woodbury bridge is shown in Figure 3.8 and Figure 3.9.

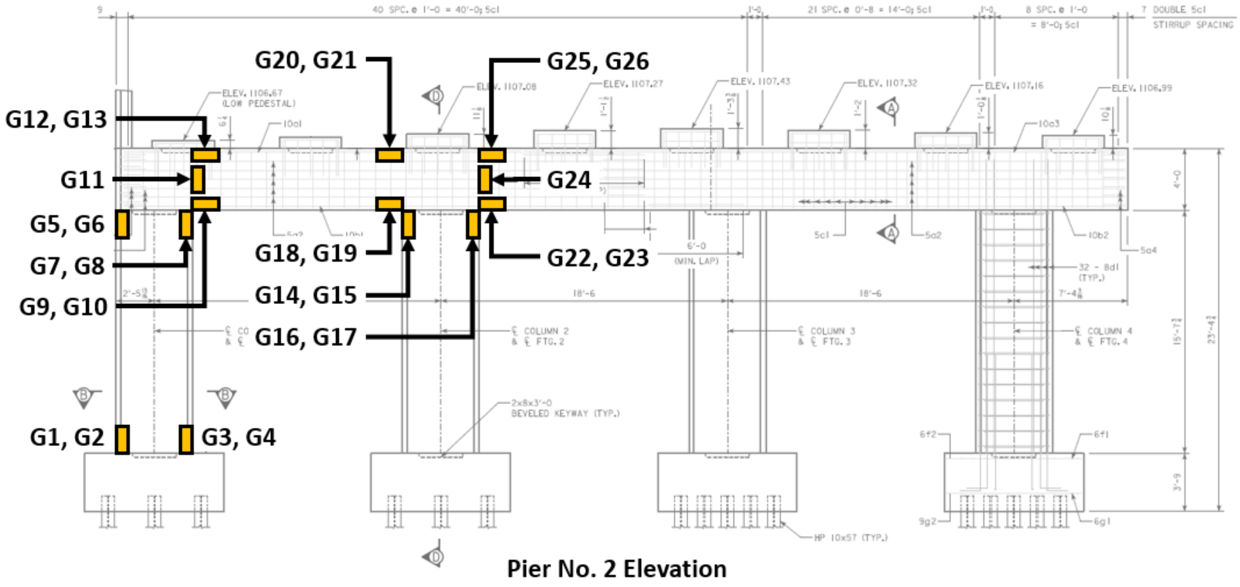

Figure 3.8. 418 Woodbury bridge sensor layout for instrumented frame pier

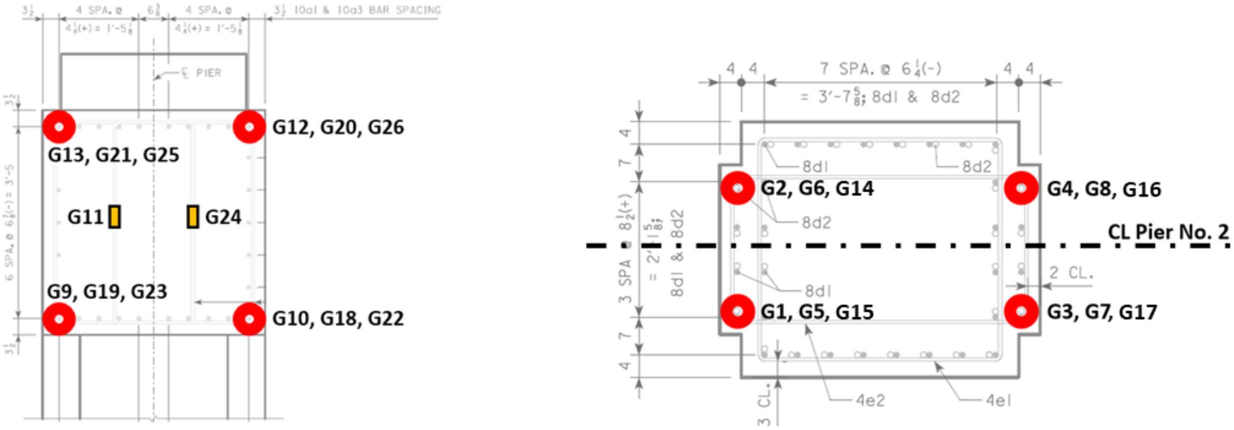

Figure 3.9. 418 Woodbury bridge sensor layout for cap beam (left) and columns right

A total of 26 sensors were installed in the west pier of the 418 Woodbury bridge. All of the sensors were located in the south half of the frame pier. Due to the general symmetry of the behavior of frame piers under volumetric changes, only half of the frame pier needed to be instrumented to accurately capture the response.

Eight sensors were located in the southernmost exterior column to capture strains at the base and top of the column. Four sensors were located in the southmost, interior column to capture the strains at the top of the column. The remaining 14 sensors were located in the cap beam. Four sensors were located above the interior face of the southmost, exterior column. Eight sensors were located above both faces of the southmost, interior column. The remaining two sensors were located near the center of the cap beam, on the inner leg of the stirrups. Examples of the sensors installed are shown in Figure 3.10.

Figure 3.10. 418 Woodbury bridge sensor placement at column base (left) and cap beam (right)

Instrumentation of the 318 Scott Bridge

Bridge Information

The 318 Scott bridge, which is in Scott County, was the second of two bridges instrumented for this study (see Figure 3.11).

Figure 3.11. 318 Scott bridge

This bridge is located in Davenport, Iowa, and carries the four lanes of Business 61, also known as West River Drive, over Rockingham Road. This bridge has a 12° skew, which means volumetric changes of the superstructure potentially affect the in-plane forces that the frame piers experience. The plan view of the 318 Scott bridge is provided in Figure 3.12.

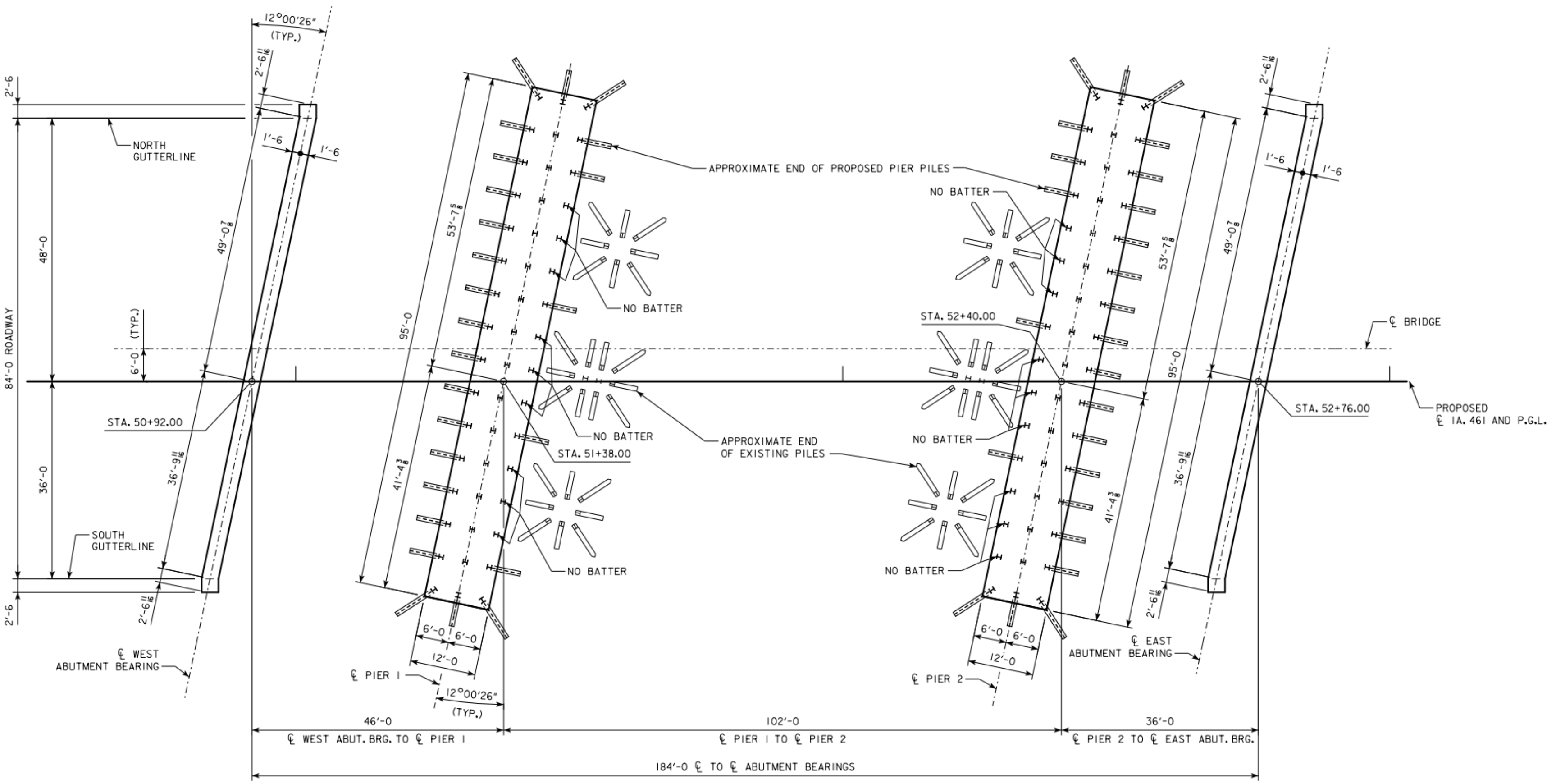

Figure 3.12. Plan view of 318 Scott bridge

The east pier was instrumented due to its columns being 2 ft 4 in. shorter, and thus stiffer, than the west pier. The instrumented frame pier had six columns 12 ft tall and spaced at about 16 ft 5.875 in. on center with an overall dimension of 82 ft 5.5 in. from the center of the exterior column to the center of the exterior column. The columns were all uniform in height and cross section. The column cross section was square, with a side dimension of 42 in. The foundation of the pier was a single 4 ft thick mat foundation with 48 steel piles, making the column bases stiffer than those of the 418 Woodbury bridge. The cap beam of the frame pier had a depth of 4 ft 6.5 in. and a width of 3 ft 6 in. The cap beam featured decorative concrete that extended 2 ft out from the faces and ends of the cap beam and had an average thickness of 10.5 in.

The 318 Scott bridge was also unique in that it had a crash wall. The crash wall that spanned between the columns was separated from the columns using a preformed joint material. The presence of the crash wall was not expected to affect column movement under the shrinkage and temperature effects of the frame pier. The completed instrumented frame pier of the 318 Scott bridge is shown in Figure 3.13.

Figure 3.13. Instrumented frame pier of 318 Scott bridge

Construction of the 318 Scott bridge took place in the summer of 2020 as summarized in Table 3.3.

Table 3.3. Construction schedule for frame pier of 318 Scott bridge

Date	Days after Cap Beam Cast	Construction Activity
6/12/2020	-24	Column Pour
7/6/2020	0	Cap Beam Pour
8/4/2020	29	Cap Forms Removed
8/24/2020	49	Beams Placed on Piers
9/24/2020	80	Deck Pour Begins

The columns were poured early during the week of June 12. The cap beam was poured on July 6. Removal of the cap beam forms began on August 4. The beams were placed on the piers beginning August 24. The deck was poured on September 24. The only significant activity in regard to the frame piers after the deck pour was the installation of the barrier rails.

Sensor Placement

The instrumentation arrangement of the 318 Scott bridge is shown in Figure 3.14 and Figure 3.15.

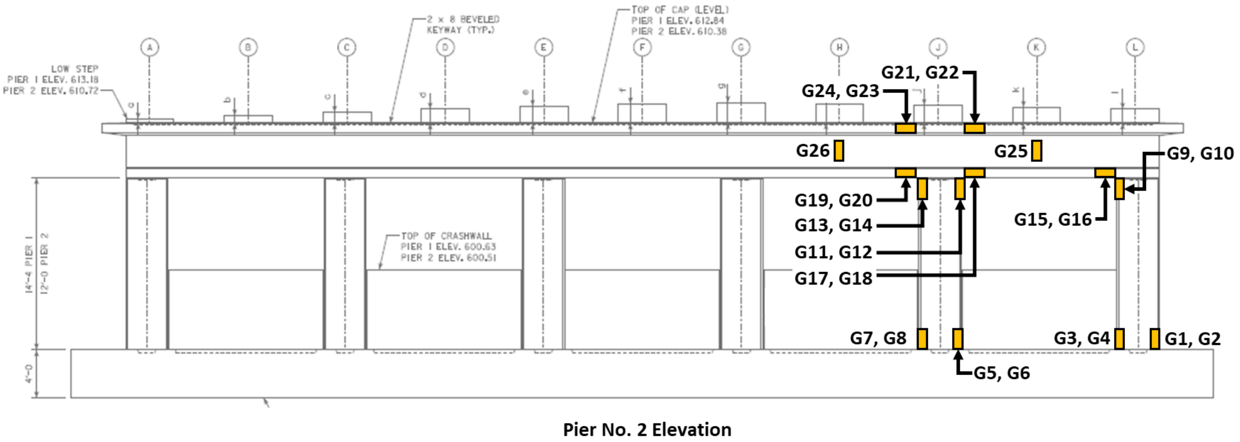

Figure 3.14. 318 Scott bridge sensor layout for instrumented frame pier

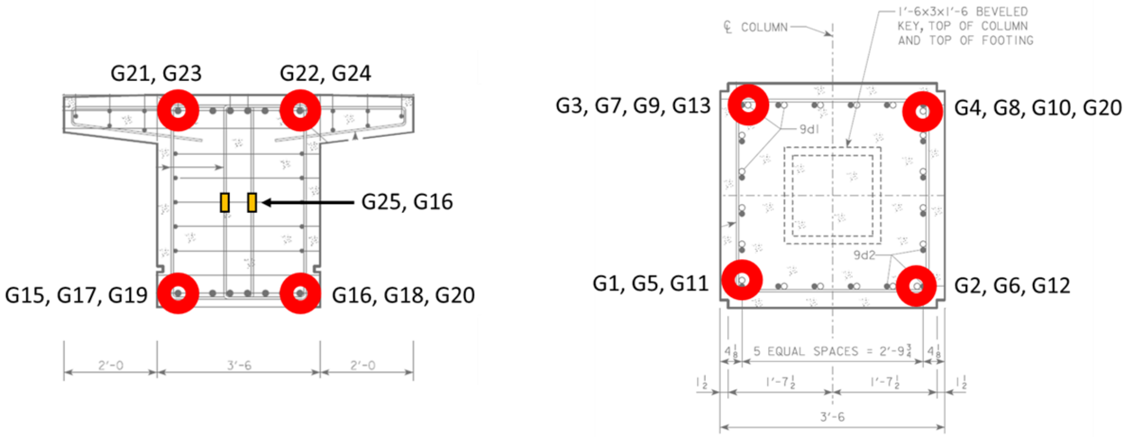

Figure 3.15. 318 Scott bridge sensor layout cap beam (left) and columns (right)

A total of 26 sensors were installed in the east pier of the 318 Scott bridge. All of the sensors were located near the northern end of the frame pier. Because the frame piers behave symmetrically under volumetric changes, and the highest forces are expected to occur near the exterior of most columns, only one end of the frame pier needed to be instrumented to accurately capture the response.

Six sensors were located in the northmost, exterior column to capture strains at the base and top of this column. Eight sensors were located in the northmost, interior column to capture the strains at the base and top of this column. The remaining 12 sensors were located in the cap beam. Two sensors were located above the interior face of the northmost, exterior column. Eight sensors were located above both faces of the northmost, interior column. The remaining two sensors were located near the center of the cap beam, on the inner leg of the stirrups. Examples of the sensors installed for the 318 Scott bridge are shown in Figure 3.16.

Figure 3.16. 318 Scott bridge sensor placement at column top (left) and cap beam (right)

Instrumentation Results for the 418 Woodbury Bridge

Data Overview

Data collection for the 418 Woodbury bridge began on June 12th, 2019, when the cap beam of the west frame pier was poured. The temperatures obtained are shown in Figure 3.17.

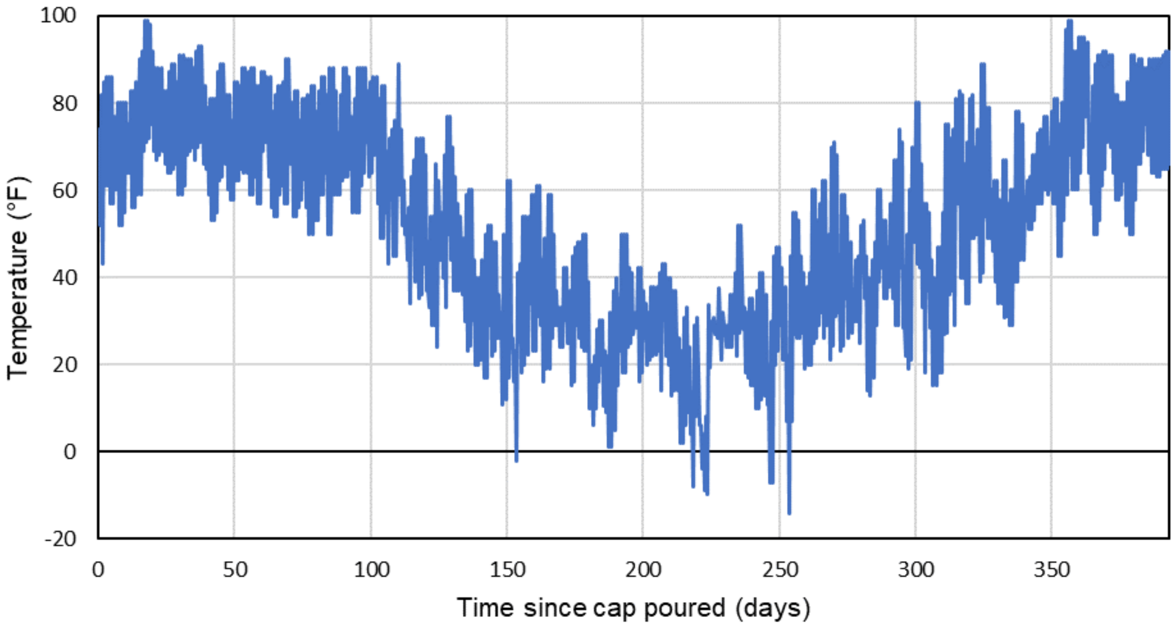

Figure 3.17. 418 Woodbury bridge temperature history during data collection period

The recorded high and low temperatures the day the cap beam was cast were 73.9°F and 52.0°F, respectively. The highest temperature recorded during the first summer after data collection began was 99.0°F. The coldest temperature recorded during the entire period of data collection was -14.1°F. The warmest temperature the second summer, and prior to the completion of data collection, was 99.0°F. This constitutes a 113.1°F temperature change over the period of data collection.

Temperature readings and strain readings for each of the 26 sensors in the 418 Woodbury bridge are provided in Figure 3.18 and Figure 3.19 respectively.

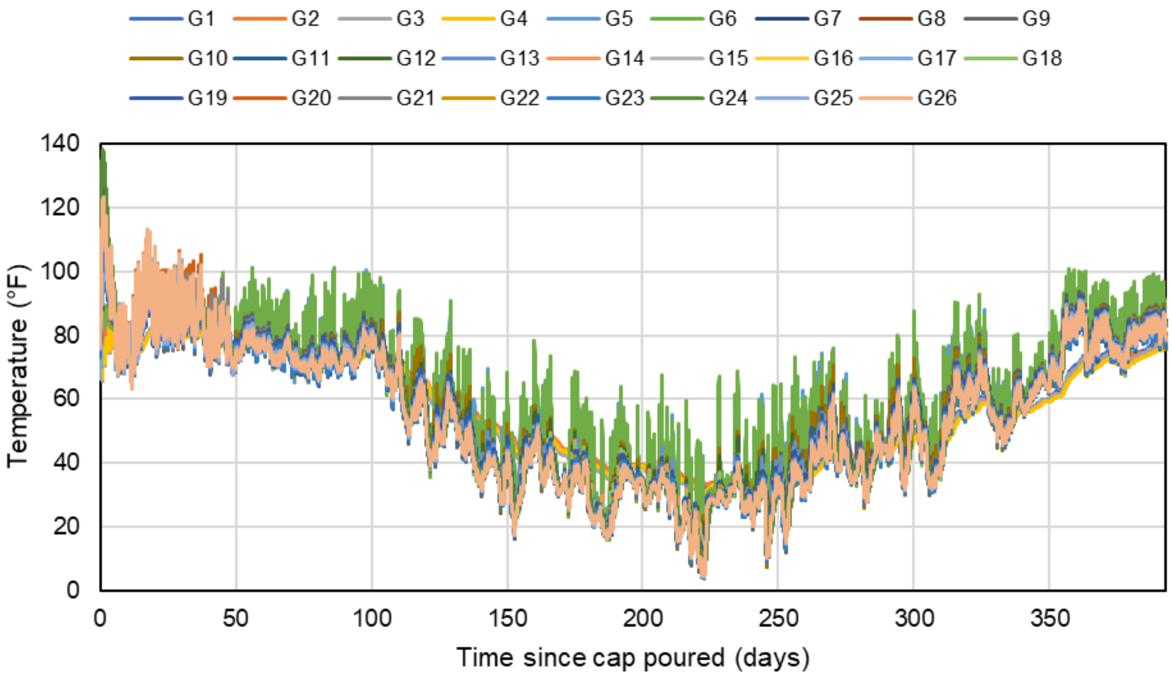

Figure 3.18. 418 Woodbury bridge temperature data collected from all sensors

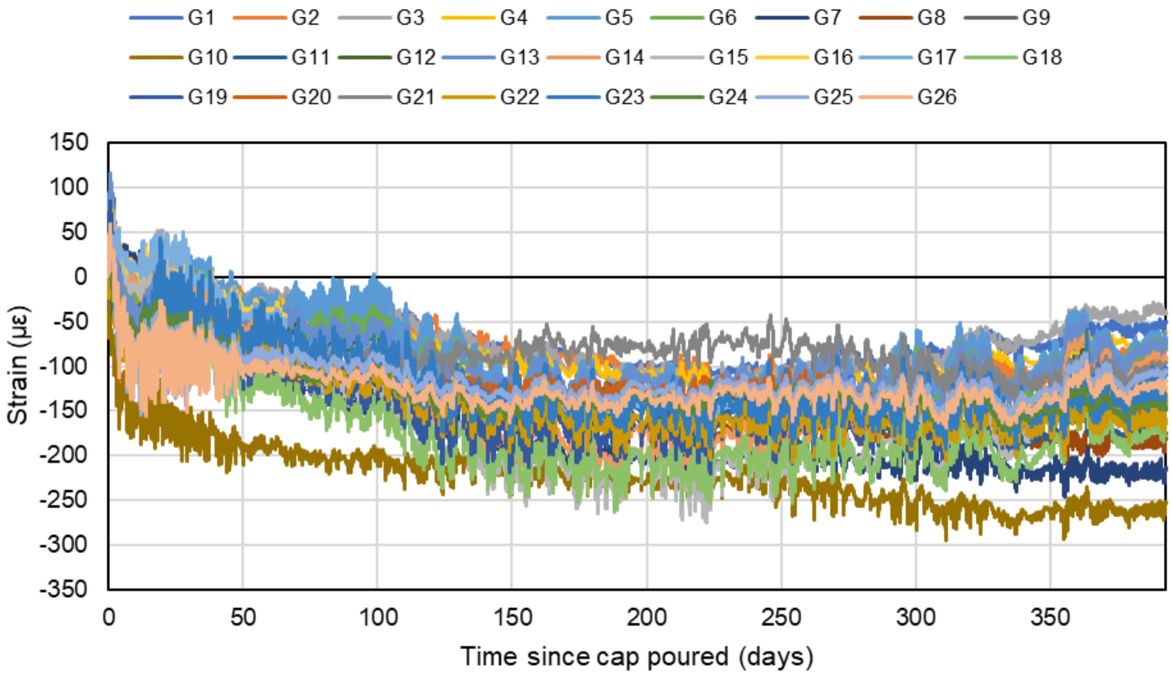

Figure 3.19. 418 Woodbury bridge strain data collected from all sensors

The recorded strains in Figure 3.19 have been corrected for the thermal effects as described in the data processing section. All sensors were determined to be functioning normally during the

13-month period of collected data. The effects of heat of hydration of the cap beam were captured. This phenomenon reached a maximum temperature of 138°F near the center of the cap beam at a concrete age of 15 hours. This phenomenon, as well as construction sequences, caused large changes in strain early on.

Diurnal temperature changes were observed throughout the structure but were most prominent early during construction. Sensors near the top surface of the cap beam experienced a maximum daily temperature change of up to 35°F before the superstructure of the bridge was installed and shielded the cap beam from the sun. However, once beams and formwork for the bridge deck were placed onto the frame pier, the diurnal temperature fluctuation significantly decreased. The maximum daily temperature change two months into the data collection period decreased to only 12°F, except for two sensors near the southern face of the exterior column. This was attributed to these two sensors being exposed to more sunlight during the day than any other sensors on the structure after the bridge deck was in place.

Looking at the recorded strain data, the maximum daily strain change at the top of the cap beam was about 100 microstrain. However, this phenomenon in the cap beam was reduced to a maximum of 40 microstrain for any given day once the beams and formwork for the deck were in place. This was primarily attributed to the beams and formwork reducing the amount of solar radiation and convection due to wind that the cap beam experienced.

Since the frame pier saw the most demand from temperature and shrinkage effects during the cold season, and after the bridge deck was in place, these diurnal fluctuations in strain were not critical to understanding the behavior of the frame pier. However, if the superstructure of a bridge was not installed prior to the cold season, these diurnal fluctuations in strain may become more notable.

Analysis of Collected Data

The collected data from pairs of sensors were averaged together to simplify the frame pier from three dimensions to two, as explained in the data processing section, to focus on the in-plane behavior of the frame pier. Through this method, data from the 26 sensors installed in the frame pier were reduced to 13 averaged pair locations, as shown in Figure 3.20.

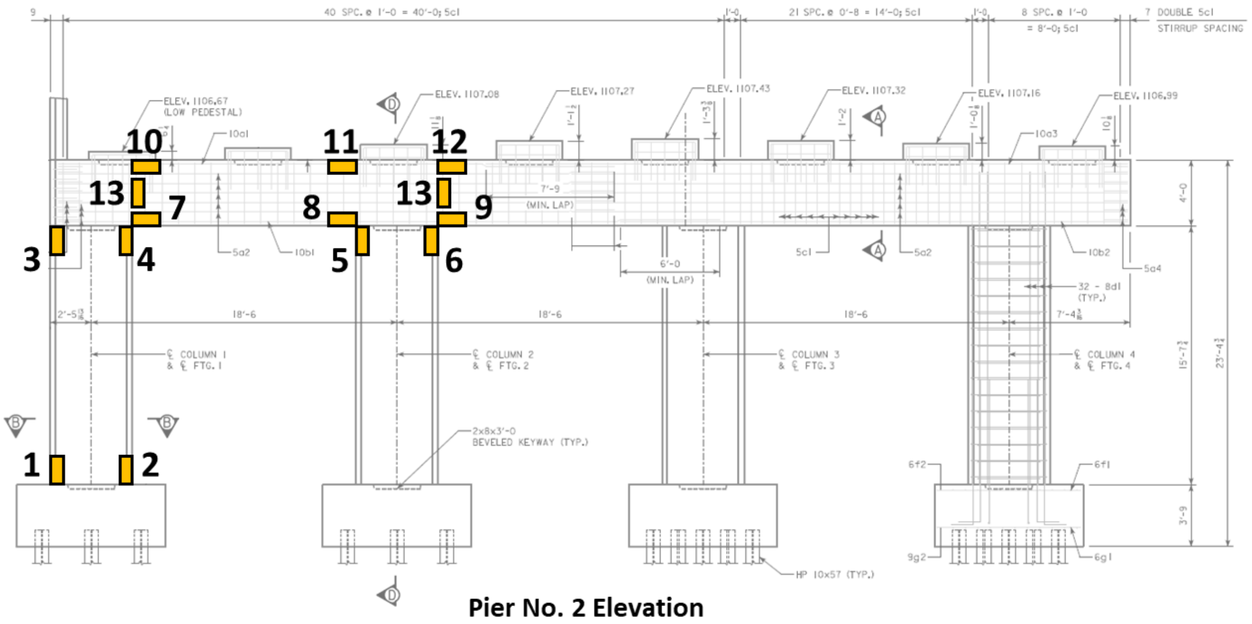

Figure 3.20. 418 Woodbury bridge averaged sensor pair locations in the instrumented frame pier

Furthermore, a 24-hr moving average of the data was taken to reduce the noise caused by diurnal temperature changes that had little effect on the susceptibility of the instrumented frame pier to temperature and shrinkage effects.

An overview of the strains recorded in the cap beam sensors are compared to those recorded in the columns in Figure 3.21.

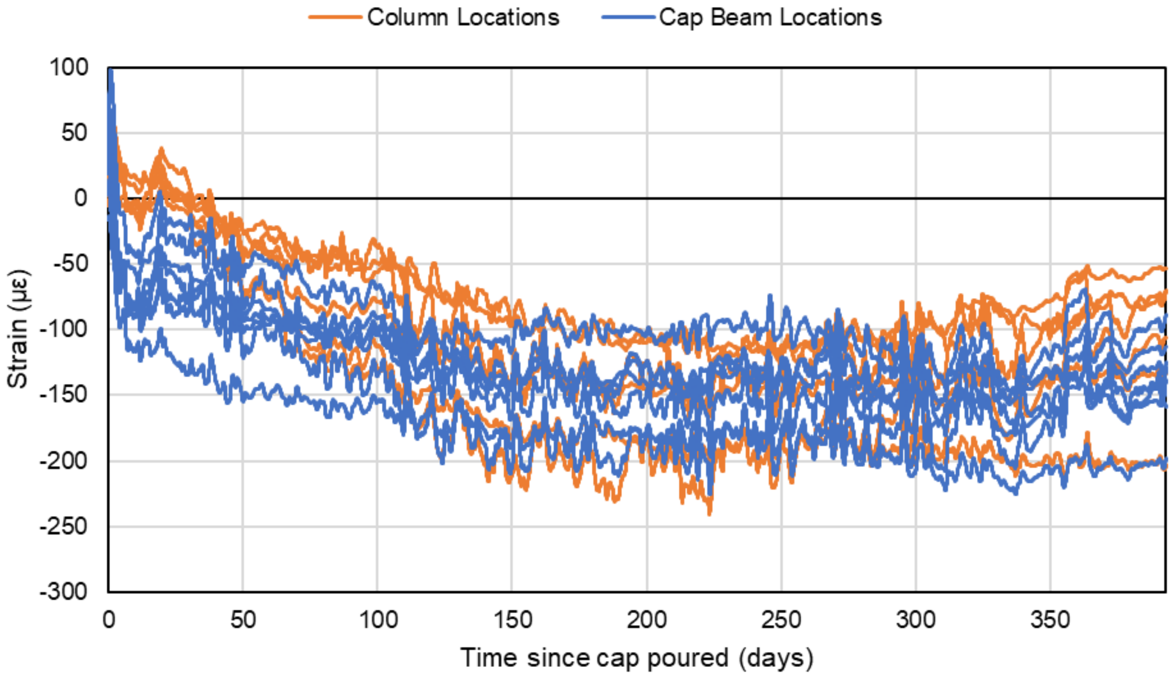

Figure 3.21. 418 Woodbury bridge strain data at averaged sensor locations

This comparison provided a high-level analysis of the behavior of the cap beam compared to that of the columns as the frame pier experienced shrinkage and temperature changes during the data collection period. The strain histories of both the column and cap beam locations were dominated by compressive behavior, with no recorded tensile strains after the early-age period of the frame pier. More early-age compressive strain could be observed in the cap beam locations. This was attributed to the start of data collection occurring weeks after the columns were cast.

For a lower-level analysis of the collected data, the strain histories of each location in the columns and the cap beam is provided in Figure 3.22 and Figure 3.23, respectively.

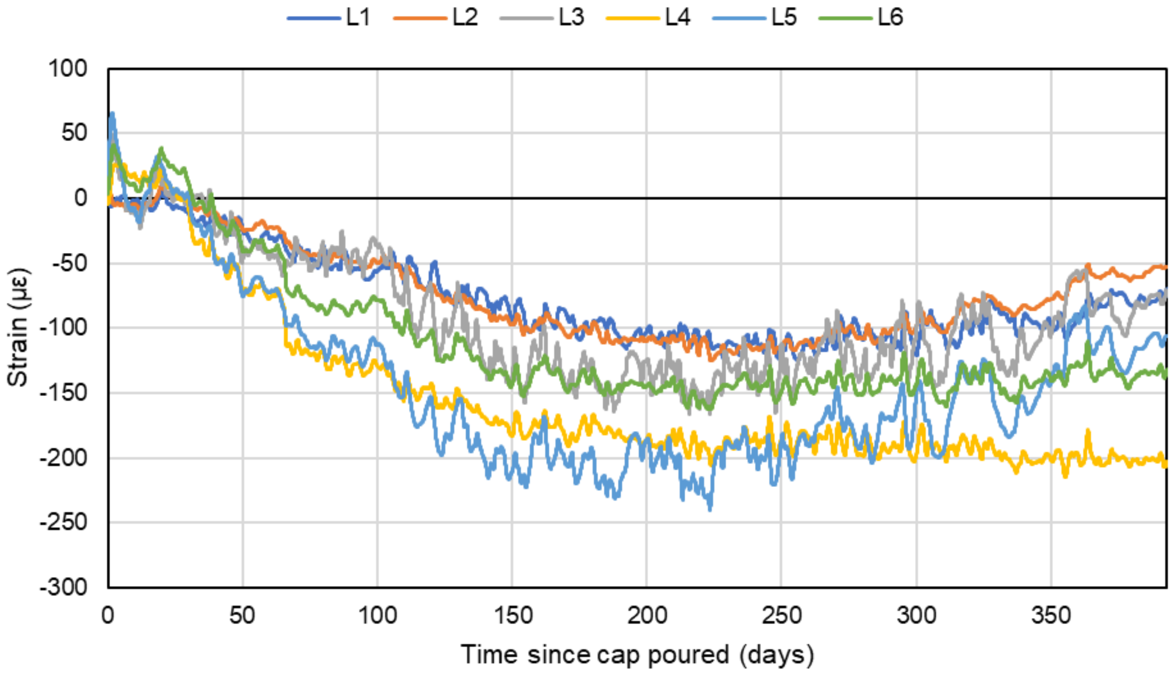

Figure 3.22. 418 Woodbury bridge column strain at averaged sensor locations

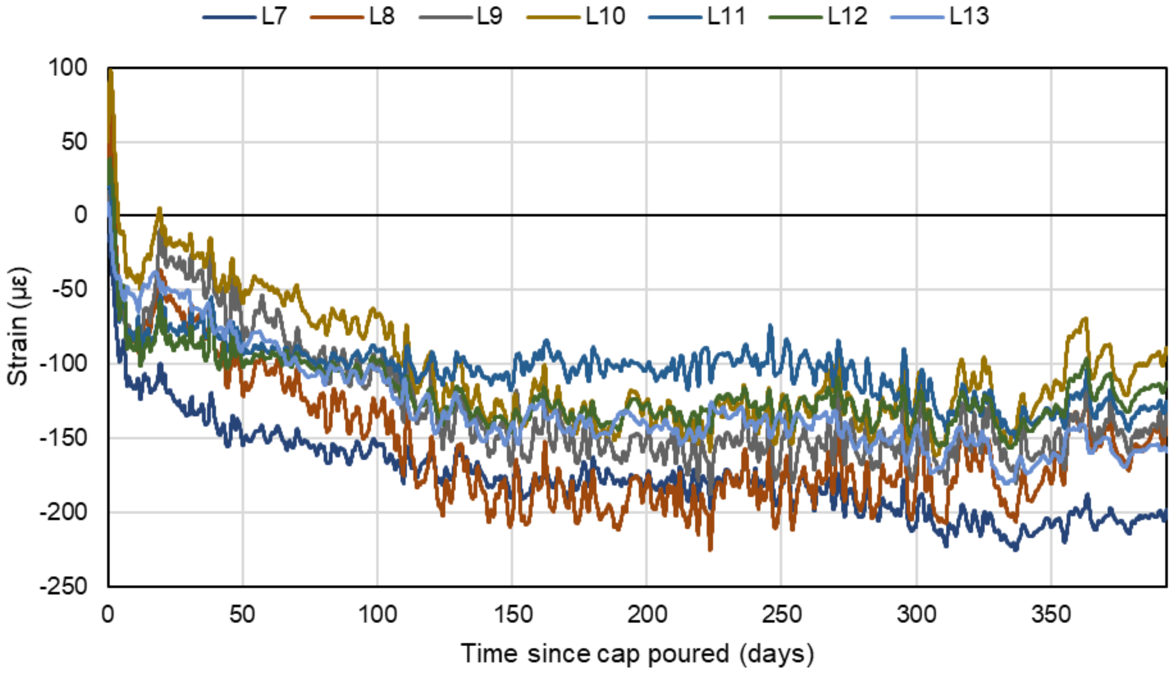

Figure 3.23. 418 Woodbury bridge cap beam strain at averaged sensor locations

These data were analyzed by focusing on two periods. The first period was the first 70 days after the cap beam was poured. This period is referred to as the early-age period of the frame pier. Due to the construction sequence of this bridge, for most of the early-age period, this frame pier was unloaded and was not covered by the superstructure of the bridge.

The added weight and shielding from sunlight that the superstructure provided when the bridge was complete caused the frame pier to behave differently. The period after the first 70 days is referred to as the operable life of the frame pier. The operable life period is of primary focus given the maximum temperature drop occurred during this period.

Tensile strain was only recorded during the early-age period of the frame pier. The highest tensile strain was recorded during heat of hydration of the cap beam. A second peak of tensile strain was observed in the strain histories on day 19, which was a particularly hot day with a high temperature of 99°F. The observed tensile behavior during the early-age period occurred at all locations relatively equally and was likely caused by localized expansion of the concrete and not frame behavior due to expansion of the cap beam, as compressive behavior would be observed at some locations. Therefore, this tensile stress was not deemed critical for this frame pier.

Throughout the operable life period of the frame pier, no sensor location experienced tensile strain. Both the largest compressive strain recorded, and the least compressive strain recorded, occurred in the columns. The maximum recorded compressive strain occurred at location 5, the top, interior face of the interior column with a magnitude of 231 microstrain. This strain occurred at the coldest point during the data collection, 222 days after the cap was cast. The second highest compressive strain occurred at location 8, which was in the cap beam directly above location 5.

Locations 4 and 7, both near the top, interior face of the exterior column, experienced high compressive strains as well. However, the strain histories of these two locations closely resembled that of a creep curve. The strain data of these sensor locations seem primarily dependent on time and not temperature. If a location was susceptible to frame behavior due to volumetric changes caused by shrinkage and temperature effects, the strain history would exhibit some dependence on temperature. Since locations 4 and 7 showed little to no dependence on temperature, these locations were likely not susceptible to temperature and shrinkage effects. For these locations, creep behavior due to gravity loading dominated their strain histories.

Comparing strains at the coldest and warmest times thereafter offered insight into which locations of the frame pier were most susceptible to volumetric changes. The locations where strains changed the most with temperature were the locations most susceptible to temperature effects, and thus shrinkage effects. Although shrinkage strain is not significantly dependent on temperature, the locations most susceptible to a temperature drop were identical to the locations most susceptible to shrinkage since both ultimately resulted in contraction of the cap beam.

Strains recorded at each location during the coldest point in time during data collection and the warmest point thereafter are provided in Figure 3.24.

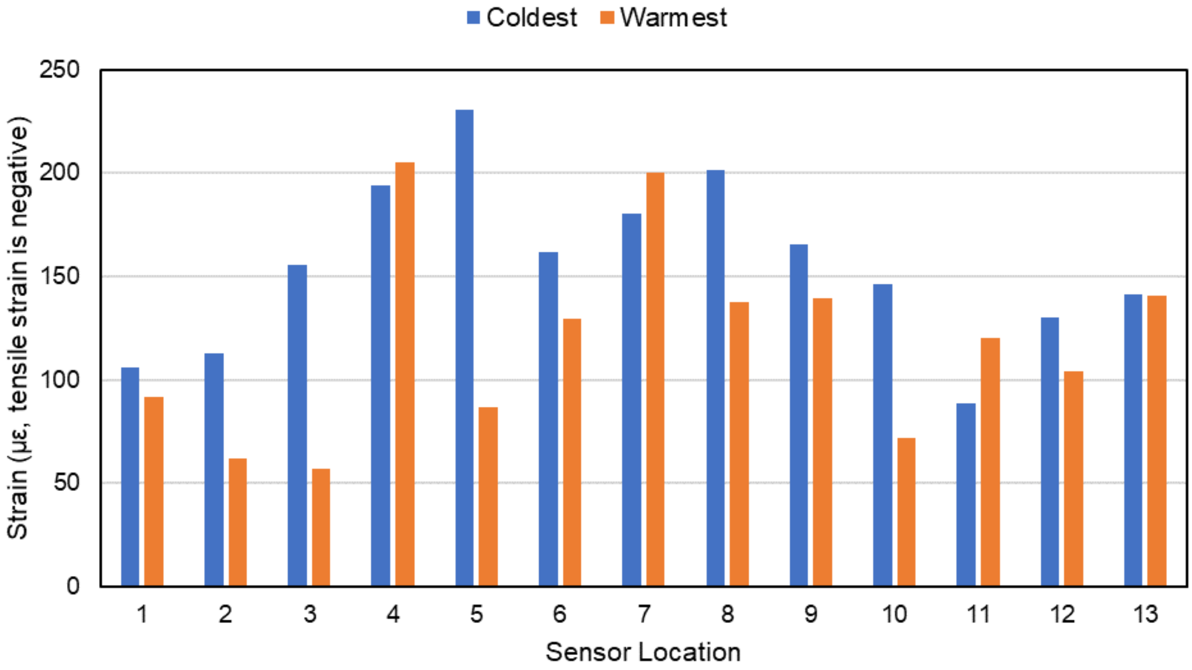

Figure 3.24. 418 Woodbury bridge strains at coldest point and warmest point thereafter

The change in strain at each location during the coldest point in time during data collection and the warmest point thereafter are provided in Figure 3.25, with positive values indicating more compressive strains occurred during the cold season versus the warm season thereafter.

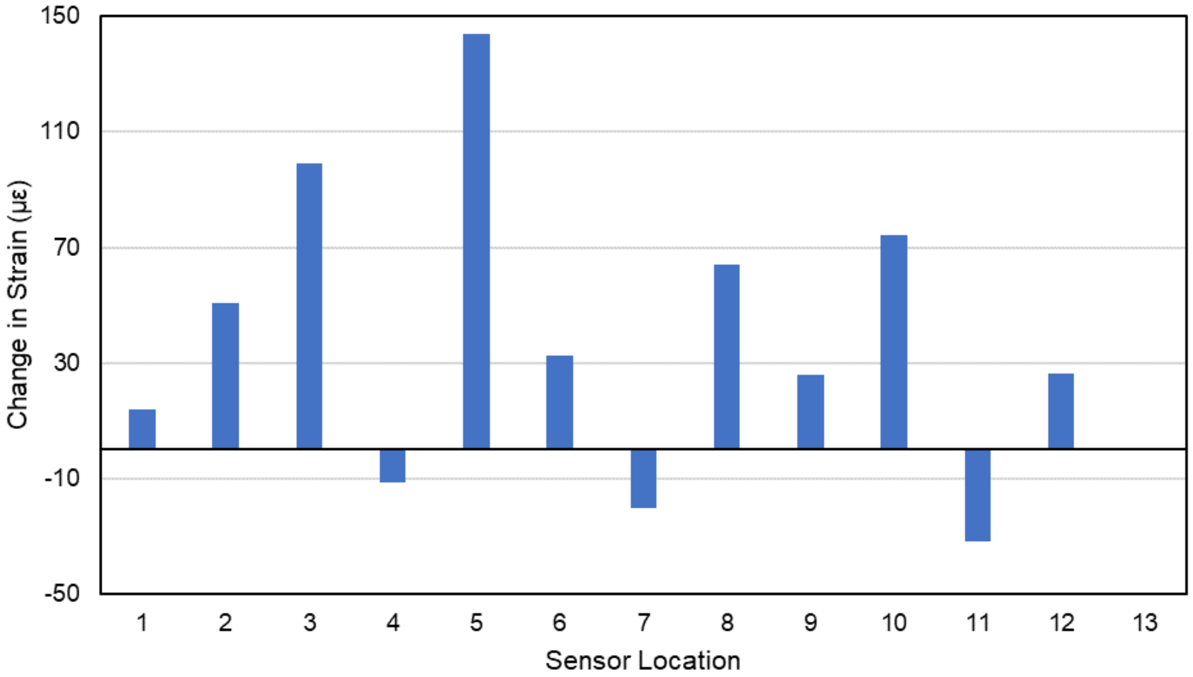

Figure 3.25. 418 Woodbury bridge change in strain between coldest point and warmest point thereafter

The change in strains between these two points in time was the most indicative of which locations were the most susceptible to temperature effects, and thus shrinkage effects. The more strain changed, the more susceptible a location was to shrinkage and temperature effects.

The most susceptible location was location 5, the top, exterior face of the interior column. This location experienced a change of strain of 144 microstrain, which was 45% higher than any other location. This location experienced an increase in compressive strain during the cold season. The second most susceptible location was location 3, the top, exterior face the exterior column. This location experienced a change of strain of 99 microstrain and experienced an increase in compressive strain during the cold season. The next three most susceptible locations were locations 2, 8, and 10, which experienced changes between 51 and 74 microstrain. These locations all experienced an increase in compressive strain during the cold season.

Three locations were noted to experience an increase in tensile strain during the cold season. However, their overall strain remained compressive. The most susceptible of these locations to tensile strain was location 11, which was at the top of the cap beam above the exterior face of the interior column. This location experienced a change of strain of -32 microstrain. Locations 7 and 4 experienced changes of strains of -20 and -11 microstrain respectively. These locations were both at the top, interior face of the exterior column, with location 4 in the column and location 7 in the cap beam.

While all strains recorded during the operable life period of the frame pier were compressive strains, it was important to observe where tensile strain behavior may happen. Tensile strain is generally more detrimental to concrete structures than compressive strain because it leads to cracking that can cause the structure's steel rebar to corrode (Shafei et al. 2012, Shafei and Alipour 2015a, Shafei and Alipour 2015b).

For the strain gauges installed on the rebar of this frame pier to have experienced tensile strain, they needed to first overcome the compressive shrinkage strain caused by the concrete. Furthermore, this frame pier was not considered susceptible to shrinkage and temperature effects. However, large tensile strains were expected in more susceptible frame piers based on damage noted in the inspection logs, as described in the previous Inspections section.

A common value taken for the crushing strain of concrete is 3,000 microstrain. Given that no tensile strain was recorded in the instrumented pier after the construction of this bridge, and the maximum recorded compressive strain was 231 microstrain or 7.7% of the crushing strain, this frame performed adequately under shrinkage and temperature effects.

Instrumentation Results for the 318 Scott Bridge

Data Overview

Data collection for the 318 Scott bridge began on July 6th, 2020 when the cap beam of the east frame pier was poured. Recorded temperatures are shown in Figure 3.26.

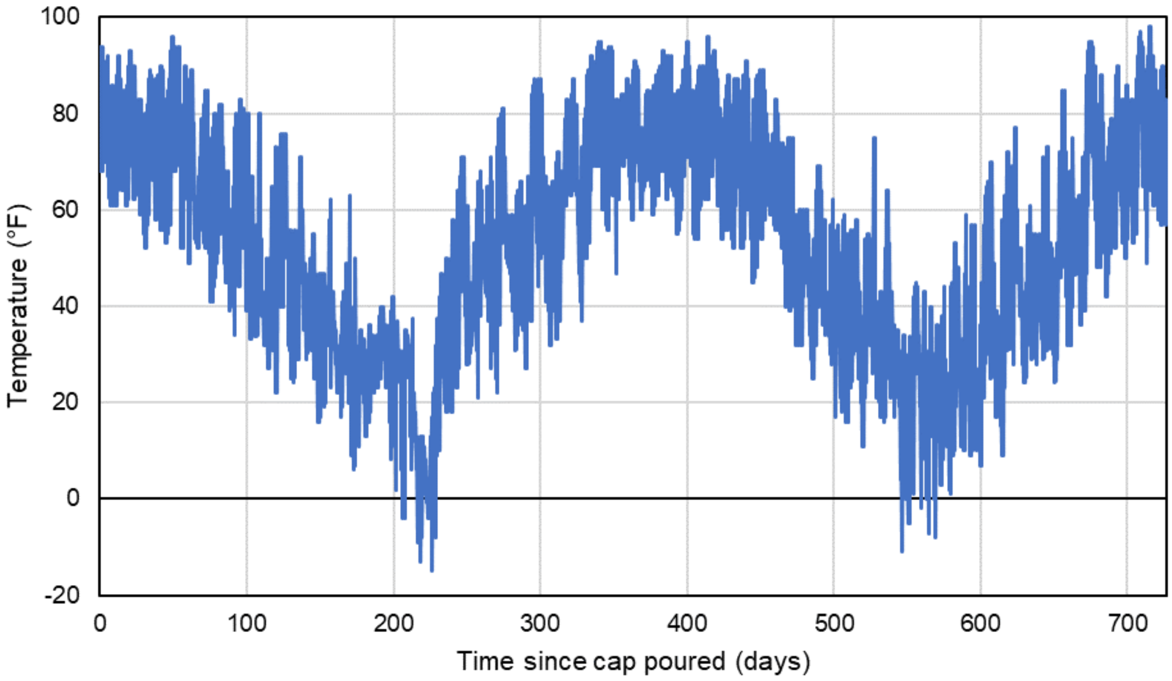

Figure 3.26. 318 Scott bridge temperature history during the data collection period

The recorded high and low temperatures the day the cap beam was cast were 93.9°F and 64.6°F, respectively. The highest temperature recorded during the first summer after data collection began was 96.1°F. The coldest temperature recorded during first cold season was -15.0°F. The warmest temperature the following summer was 96.1°F. The coldest temperature recorded during the second cold season was -11.0°F. The warmest temperature recorded the following summer and prior to the completion of data collection was 98.1°F. This constituted a 111.1°F temperature change the first year of data collection and a 109.1°F temperature change the second year of data collection.

Temperature readings and strain readings for each of the 26 sensors installed in 318 Woodbury are provided in Figure 3.27 and Figure 3.28, respectively.

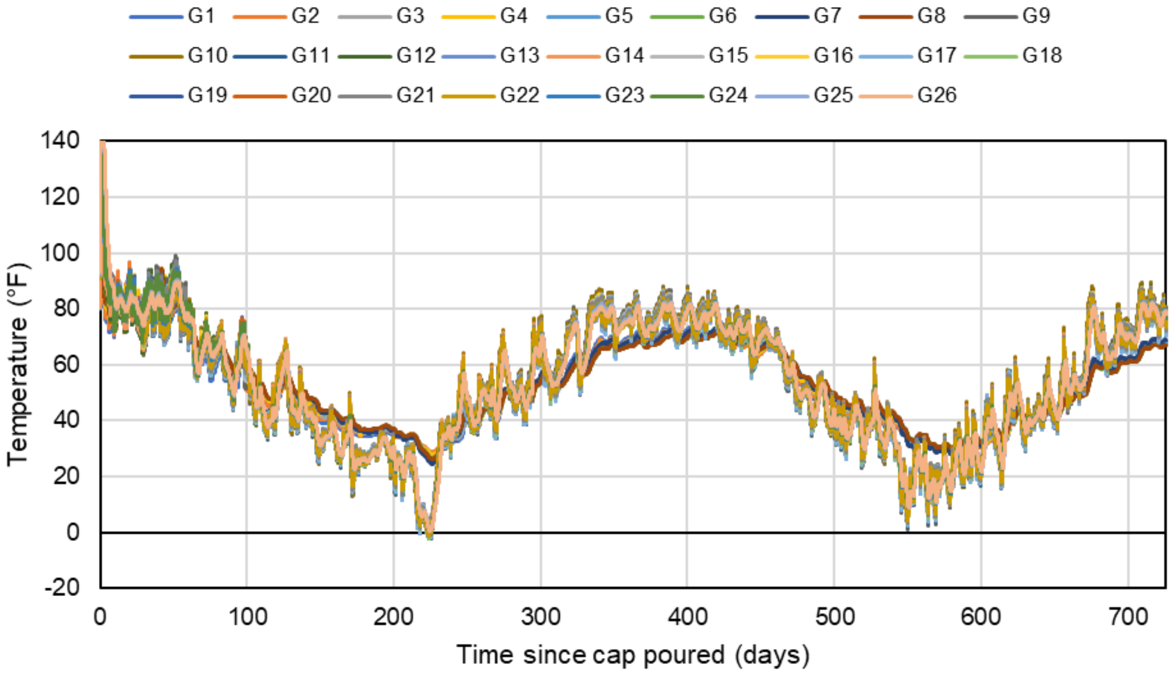

Figure 3.27. 318 Scott bridge temperature data collected from all sensors

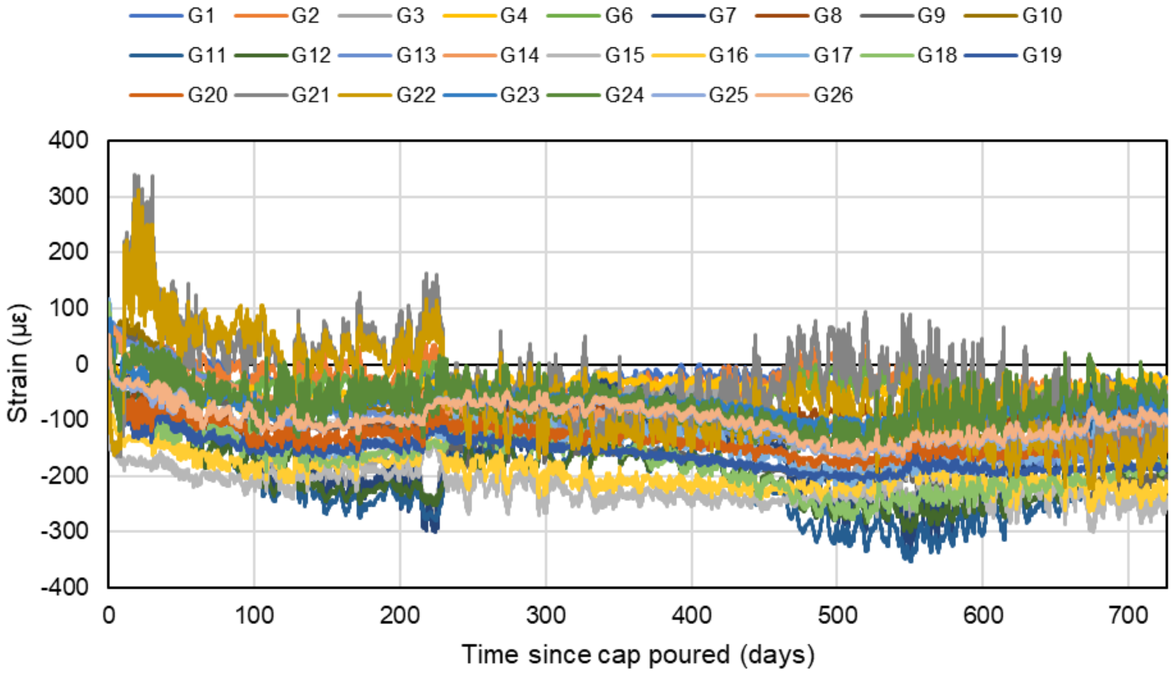

Figure 3.28. 318 Scott bridge strain data collected from all sensors

The recorded strains in Figure 3.28 have been corrected for the thermal effects as described in the data processing section. Sensor 5 recorded temperature but did not record strain during the data collection period. Furthermore, two sensors were found to have malfunctioned during the 24-month data collection period. Sensors 21 and 22, both located at the top, interior face of the interior column, experienced an increase in tensile strain of 300 microstrain on July 17th, 2020, 11 days after the cap beam was cast. This was a relatively large change in strain in the frame pier with no clear cause. There were no construction activities involving the instrumented frame pier that day, as the forms for the cap beam were not removed until August 4th, 2020. The effects of heat of hydration ended days prior to the occurrence of this large increase in tensile strain.

Additionally, none of the sensors near sensors 21 and 22 recorded any similar change in strain that day. It would be expected that those sensors' strain histories would reflect a large change in strain nearby. For example, if the tensile strain recorded was caused by the cap beam bending, the sensors at the top of the cap beam would record an opposite strain increase. However, no other sensors recorded any unusual changes in strains that day. For these reasons, the data from sensors 21 and 22 were discarded. The remaining 24 sensors functioned normally over the data collection period.

The effects of heat of hydration of the cap beam were captured. This phenomenon reached a maximum temperature of 164°F near the center of the cap beam at a concrete age of 23 hours. This phenomenon, as well as construction sequences, caused large, early changes in strain.

Diurnal temperature changes were observed throughout the structure but were most prominent early during construction. Sensors near the top surface of the cap beam experienced higher temperature fluctuations when the cap beam was exposed to the sun. However, once the beams and formwork for the bridge deck were placed on the frame pier, the diurnal temperature fluctuation significantly decreased.

Looking at the recorded strain data, the maximum daily strain change at the top of the cap beam was about 70 microstrain early on. However, this phenomenon in the cap beam was reduced to a maximum of about 30 microstrain for any given day once the beams and formwork for the deck were in place. This can be primarily attributed to the beams and formwork reducing the amount of solar radiation and convection due to wind that the cap beam experienced.

Given that the bridge frame pier saw the most demand from shrinkage and temperature effects during the cold season and after the bridge deck was in place, these diurnal fluctuations in strain were not critical to understanding the behavior of the frame pier. However, if the construction schedule of a frame pier did not have the superstructure of the bridge installed prior to the cold season, these diurnal fluctuations in strain may have become more notable.

Analysis of Collected Data

The collected data from pairs of sensors were averaged together to simplify the frame pier from three dimensions to two, as explained in the data processing section, to focus on the in-plane behavior of the frame pier. Through this method, data from the 26 sensors installed in the frame pier were reduced to 13 averaged pair locations, as shown in Figure 3.29.

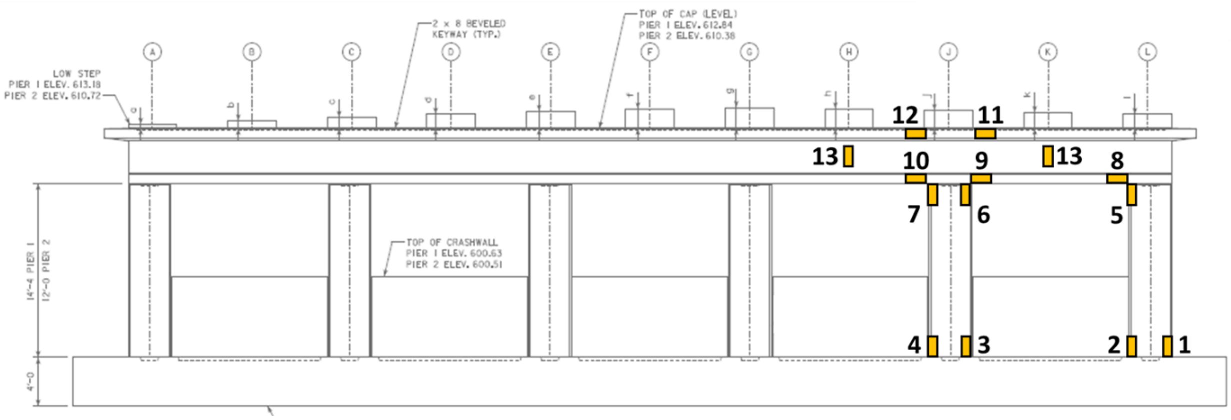

Figure 3.29. 318 Scott bridge averaged sensor pair locations in the instrumented frame pier

Furthermore, a 24-hr moving average of the data was performed to reduce the noise caused by diurnal temperature changes that have little effect on the susceptibility of the instrumented frame pier to shrinkage and temperature effects. Note that location 10 in Figure 3.29 is composed of the two sensors whose data were discarded due to a malfunction. Furthermore, location 3 was only composed of one sensor as sensor 5 did not record strain data, also due to a malfunction.

The strains recorded in the cap beam sensors are compared to those recorded in the columns in Figure 3.30.

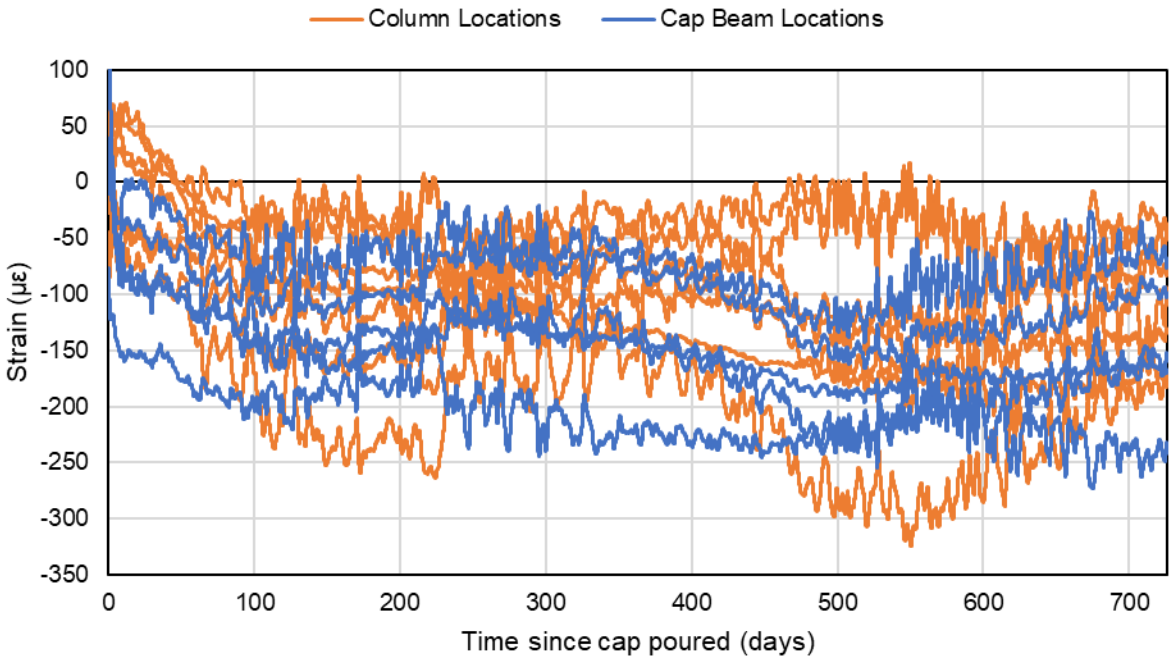

Figure 3.30. 318 Scott bridge strain data at averaged sensor locations

This comparison provided a high-level analysis of the behavior of the cap beam in comparison to that of the columns as the frame pier experienced shrinkage and temperature changes during the data collection period. Because the frame pier was constructed in the warm season and the effects of thermal contraction added to shrinkage, the cold seasons saw the highest strains recorded.

During the coldest point of the first year, at around 223 days after the cap beam was poured, the highest compressive strain and highest tensile strain both occurred in the columns. The maximum compressive strain in the columns at this point was more than twice that of the cap beam. Furthermore, while the columns experienced tensile strain, the cap beam did not. The minimum compressive strain recorded in the cap at this time was around 60 microstrain. Clearly, the maximum strains occurred in the columns during the first cold season.

During the coldest point of the second year, at around 550 days after the cap beam was poured, the maximum compressive strain and maximum tensile strain again occurred in the columns. Looking at the trends of the strain histories during the second year, the strains in the columns seemed to diverge at the coldest point and reach their maximum values. However, the strain histories of the cap beam seemed to converge and reduce in magnitude. This behavior also occurred in the first year but was more apparent in the second year. This behavior was expected, as the gravity loads on the cap beam created internal forces that negated those caused by the contraction of the cap beam.

While this behavior meant that the cap beam of the 318 Scott bridge was not the critical element with regards to shrinkage and temperature effects, it is important to note that behavior depended heavily on the geometry of the bridge. As noted in the inspections section, the only noted damage in inspection logs that may have been due to shrinkage and temperature effects occurred in the cap beam. Furthermore, if the construction schedule of a frame pier did not have the superstructure of the bridge installed prior to the cold season, the cap beam would likely see higher strains due to shrinkage and temperature effects.

For a lower-level analysis of the collected data, the strain histories of the locations in the columns and the locations in the cap beam are provided in Figure 3.31 and Figure 3.32, respectively.

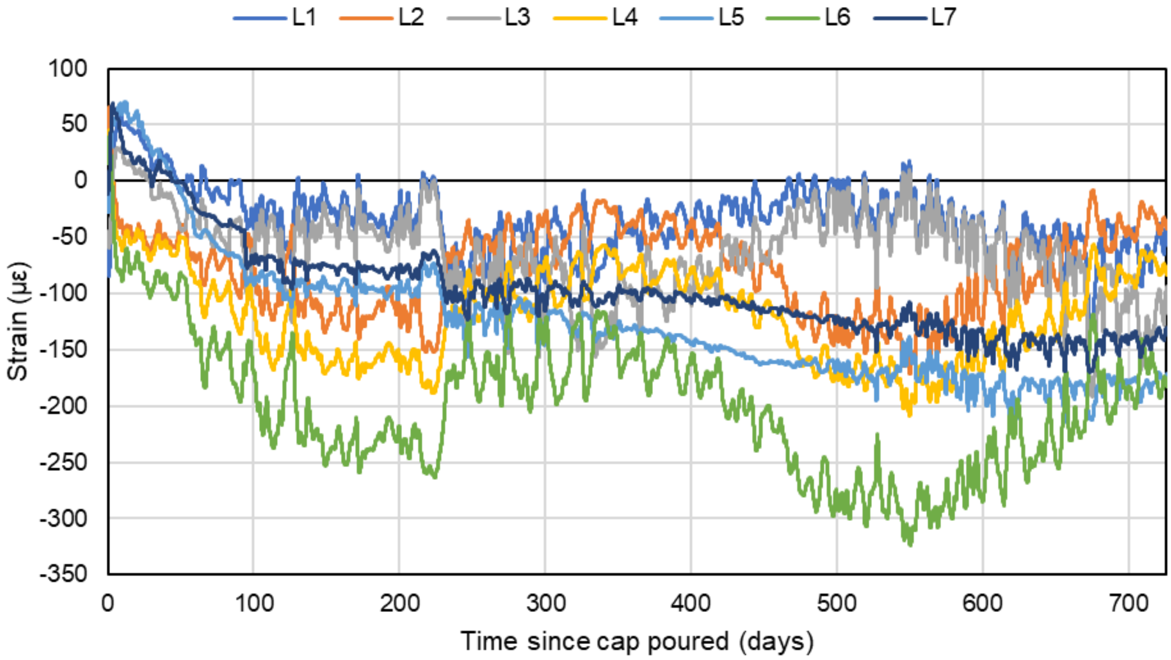

Figure 3.31. 318 Scott bridge column strain at averaged sensor locations

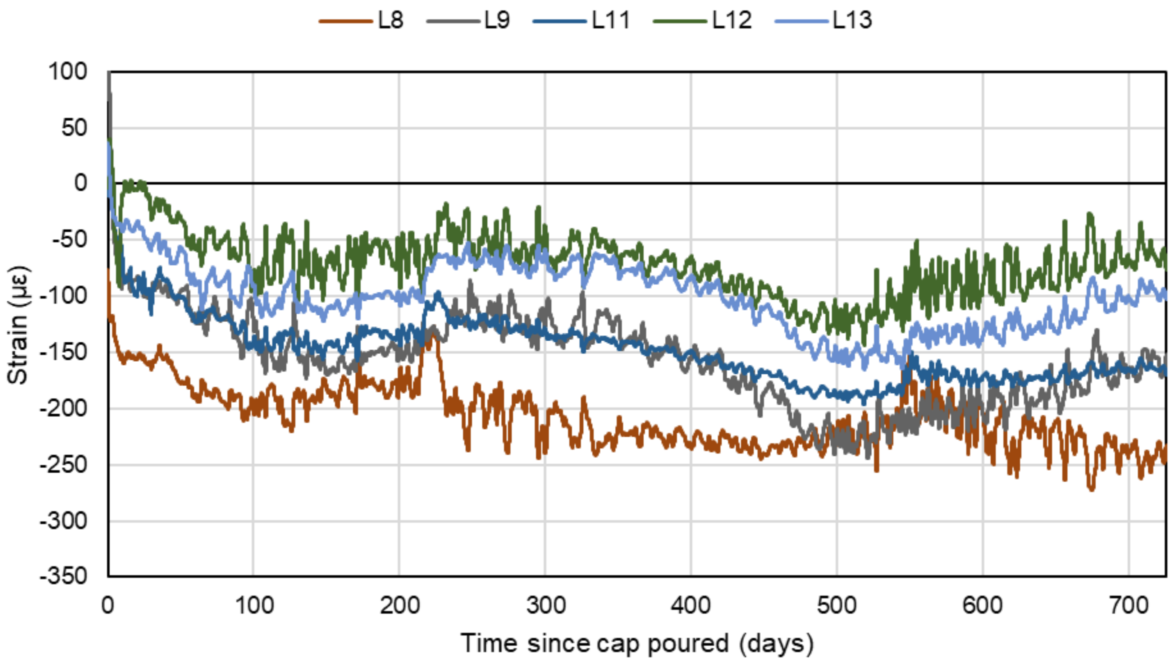

Figure 3.32. 318 Scott bridge cap beam strain at averaged sensor locations

These data were analyzed by focusing on two periods. The first period considered was the first 90 days after the cap beam was poured. This period is referred to as the early-age period of the frame pier. Due to the construction sequence of this bridge, for most of the early-age period this frame pier was unloaded and not covered by the superstructure of the bridge. The added weight and shielding from sunlight of the superstructure when the bridge was completed caused the frame pier to behave differently. The period after the first 90 days is referred to as the operable life of the frame pier. The operable life period was of primary focus since the maximum temperature drop occurred during this period.

The highest tensile strains occurred during the early-age period at 100 microstrain in the cap beam. This strain was recorded 18 hours after the cap beam was cast and could be attributed to the heat of hydration causing the cap beam to expand. Locations in the columns also experienced some tensile strain during the early age, peaking at 71 microstrain. This peak occurred 12 days after the cap beam was cast, after the heat of hydration had ended.

The strain could be attributed to a few causes: the lack of gravity loading on the frame pier, the rapid early-age shrinkage of the cap beam, and the data collection starting after some early-age shrinkage had already occurred in the columns, which likely induced unrecorded compressive strain. These early-age tensile strains were ultimately considered non-critical, as they occurred before the frame pier supported the superstructure and diminished with time. Furthermore, the maximum compressive strains did not occur during this early-age period.

The frame pier experiences its largest compressive strain during the operable life period. Tensile strain was also recorded during this period, when the frame pier was subjected to the coldest temperatures during the data collection. For the aforementioned reasons, the remaining data analysis focuses on the operable life period of the frame pier.

The observation of tensile strain outside of the early-age period was unlike that of the 418 Woodbury bridge, which experienced no tensile strain during its recorded operable life period. This can be attributed to the 318 Scott bridge having stiffer columns and a longer frame length. The maximum tensile strains were recorded during the second-year cold season and had magnitudes of 17 microstrain and 10 microstrain in locations 1 and 3, respectively. These two locations were at the bases of the columns, with location 1 at the exterior face of the exterior column and location 2 at the exterior face of the interior column. Tensile strain was likely only recorded at these locations since they were below grade and remained about 30°F warmer than locations above grade during the cold season. This allowed these locations to experience less localized, or free, strain due to pure thermal contraction rather than frame behavior.

During the first-year cold season, locations 5 and 7 were the next closest to experiencing tensile strain with a minimum compressive strain of 61 microstrain. However, the strain histories of these two locations resembled that of a creep curve. During the second-year cold season, these two locations experienced higher compressive strains at over 100 microstrain.

The maximum recorded compressive strain occurred in the second-year cold season. Likewise, the highest recorded tensile strain, outside of the early-age period, occurred during the second-year cold season. Furthermore, the trends observed during the second year reflect those of the first year but were more defined with higher magnitudes of strain. For these reasons, the second-year cold season was analyzed for locations susceptible to shrinkage and temperature effects.

The maximum compressive strain recorded occurred at location 6, the top, exterior face of the interior column. This location experiences a maximum compressive strain of 324 microstrain the second year. Location 6 also experienced the highest compressive strain the first year at 264 microstrain. Locations with similar strain histories to that of location 6 included locations 2 and 4, both at the bottom, interior faces of the columns. The similarities of the strain histories of these locations primarily included an increase in compressive strain during the cold season and a decrease in compressive strain during the warm seasons.

The maximum tensile strain, outside of the early-age period, occurred at location 1, the bottom, exterior face of the exterior column. This location experienced a tensile strain of 17 microstrain the second year. Location 1 also experienced the highest tensile strain the first year at 10 microstrain. Location 3, the bottom, exterior face of the interior column, had a similar strain history as location 1 and reached similar tensile strain values of 7 microstrain the second year and 1 microstrain the first year. The strain histories of both these locations showed an increase in tensile strain during the cold seasons and a decrease in tensile strain during the warm seasons.

Other locations with similar strain histories included locations 8 and 11. Locations 5 and 7 had somewhat similar strain histories, but their strain histories prominently resembled that of a creep curve. That is, these two locations consistently saw increasing compressive strain with time and experienced little change in their strains as temperature changed.

Comparing strains at the coldest point in time and warmest point in time thereafter offered insight into which locations of the frame pier were most susceptible to volumetric changes. The locations where strains changed the most with temperature were the locations most susceptible to temperature effects and thus shrinkage effects. Although shrinkage strain is not significantly dependent on temperature, the most susceptible locations to a temperature drop were identical to the most susceptible locations to shrinkage since both ultimately resulted in contraction of the cap beam.

Strains recorded at each location during the coldest point in time during data collection and the warmest point thereafter for both the first and second year of data collection are provided in Figure 3.33.

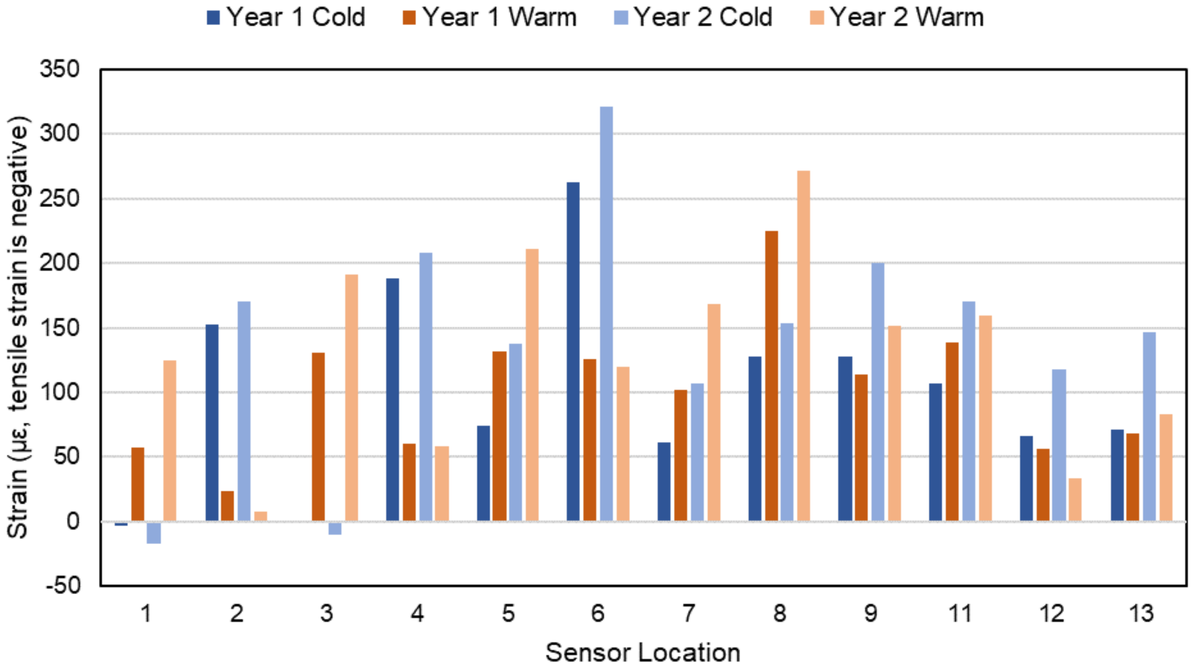

Figure 3.33. 318 Scott bridge strains at coldest point and warmest point thereafter

The change in strain at each location during the coldest point in time during data collection and the warmest point thereafter for both the first and second year of data collection are provided in Figure 3.34, with positive values indicating that more compressive strains occurred during the cold season than the warm season thereafter.

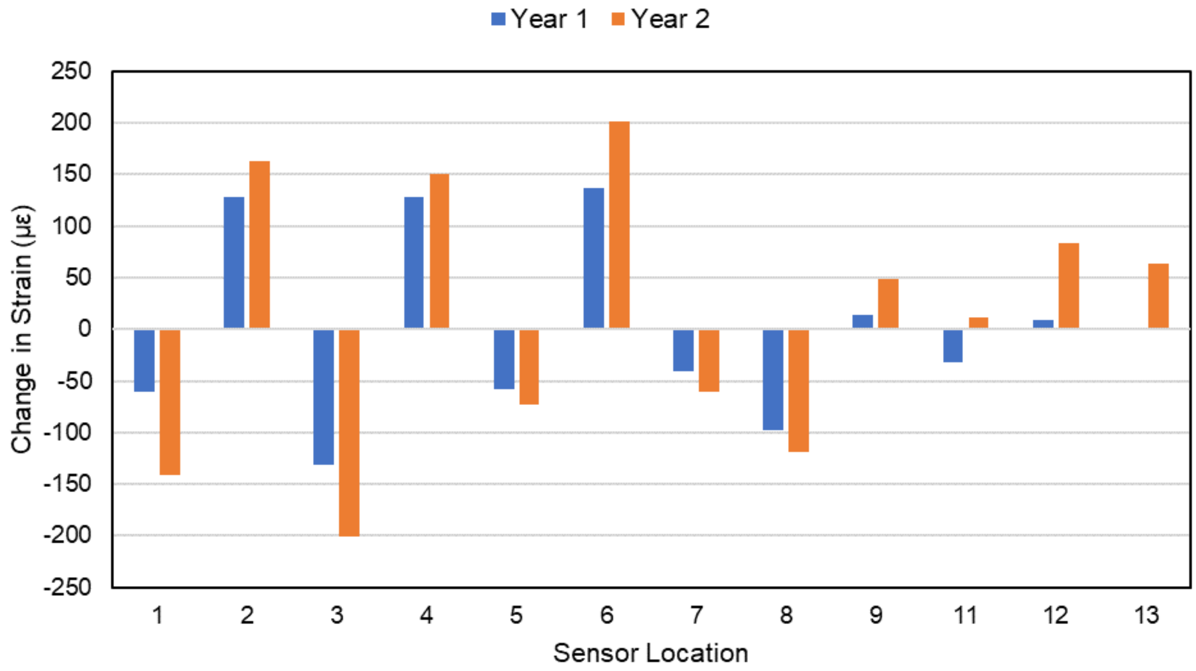

Figure 3.34. 318 Scott bridge change in strain between coldest point and warmest point thereafter

The change in strains between these two points in time are the most indicative of which locations were most susceptible to shrinkage and temperature effects. The greater the change in strain, the more susceptible a location was to shrinkage and temperature effects.

The most susceptible locations were locations 3 and 6. Location 3 was at the bottom, exterior face of the interior column and location 6 was at the top, exterior face of the interior column. Location 3 experienced a -201 microstrain change and location 6 experienced a 201 microstrain change. Of these two locations, location 3 was more susceptible since it experienced an increase in tensile strain during the cold season.

Locations 1, 2, 4, and 8 were more susceptible than the remaining locations. Of these locations, locations 2 and 4 experienced an increase in compressive strain during the cold seasons, while locations 1 and 8 experienced an increase in tensile strain during the cold seasons. Locations 2 and 4 experienced changes in strain of 162 microstrain and 150 microstrain respectively.

After location 3, location 1, the bottom, exterior face of the exterior column, experienced the next greatest increase in tensile strain during the cold seasons. This location experienced a change in strain of -142 microstrain. Despite only locations 1 and 3 experiencing tensile strain, there were locations that experienced an increase tensile strain during the cold season despite their overall strain remaining compressive. The most susceptible of these locations was location 8, the bottom of the cap beam above the interior face of the exterior column. This location experienced a change of strain of -119 microstrain. The other two locations were locations 7 and 5, which experienced a change in strain of -61 microstrain and -73 microstrain respectively.

Note the locations where tensile strain may occur given that tensile strain is generally more detrimental to concrete structures than compressive strain. This is because tensile strain leads to cracking that can lead to the corrosion of the steel rebar of the structure.

A common value taken for the crushing strain of concrete is 3,000 microstrain. Therefore, the maximum compressive strain recorded for this frame pier at 231 microstrain was 7.7% of the crushing strain. No observable cracks were discovered during the data collection period of this frame pier, despite some tensile strains being recorded. Therefore, this frame pier performs adequately under shrinkage and temperature effects.

CHAPTER 4. FINITE ELEMENT SIMULATIONS

Background

Multiple FE software packages were suitable for this study. Abaqus/CAE was selected based on its advanced and well-tested capabilities with modeling reinforced concrete (DeJong et al. 2021a, DeJong et al. 2021b, Karim and Shafei 2021, Karim and Shafei 2022, Shi et al. 2019, Shi et al. 2020c). Like many FE software packages, Abaqus does not natively support shrinkage, but it does support user subroutines that allow users to develop codes to implement behaviors not natively supported.

For example, user subroutines are commonly used to model a material that is not supported by Abaqus. Abaqus user subroutines have also been used to incorporate shrinkage and creep into models (Li et al. 2013, Bažant and Yu 2010, Purani 2013, Kasera 2014). This established usage of Abaqus to model shrinkage and its prevalence in the field of bridges made Abaqus appropriate for use in this study.

Incorporating Shrinkage and Creep Effects

Abaqus, like many other FE software packages available, does not offer built in support for shrinkage and creep. Instead, Abaqus offers user subroutines, which are user-developed programs, commonly written in the FORTRAN programming language, that run with Abaqus. It is common practice to apply shrinkage and creep strain to the model as a thermal strain (Li et al. 2013, Levy 2010, Purani 2013, Kasera 2014). For this purpose, the USDFLD and UEXPAN user subroutines that Abaqus provides were used to incorporate the shrinkage and creep model into the FE software. The shrinkage component of the thermal strain increment can be calculated according to equation (4.1).

$$\Delta\varepsilon_{sh} = \varepsilon_{current} - \varepsilon_{previous} \tag{4.1}$$

where $\Delta\varepsilon_{sh}$ is the shrinkage component of the strain increment, $\varepsilon_{current}$ is the total shrinkage strain for the current increment, and $\varepsilon_{previous}$ is the total shrinkage strain from the previous increment.

The creep component of thermal strain requires the current elastic strain at each material point. This was obtained using the state variables that are defined in the USDFLD user subroutine. The current increment time and total time of analysis are also used to calculate the creep component of thermal strain, which is defined for each principal direction according to equation (4.2).

$$\Delta\varepsilon_{creep} = \varepsilon_{elastic}\left(\phi_{current}\chi_{current} - \phi_{previous}\chi_{previous}\right) \tag{4.2}$$

where $\Delta\varepsilon_{creep}$ is the creep component of the strain increment, $\varepsilon_{elastic}$ is the current elastic strain, $\phi_{current}$ is the creep coefficient for the current increment, $\chi_{current}$ is the aging coefficient for the current increment, $\phi_{previous}$ is the creep coefficient for the previous increment, and $\chi_{previous}$ is the aging coefficient for the previous increment.

The total strain increment ($\Delta\varepsilon_{total}$) at each material point was calculated according to equation (4.3).

$$\Delta\varepsilon_{total} = \Delta\varepsilon_{creep} - \Delta\varepsilon_{sh} \tag{4.3}$$

The developed user subroutine could identify if the creep strain increment was caused by a tensile or a compressive stress. This allowed the user subroutine to appropriately calculate the creep strain increment for either tensile or compressive creep as necessary. Furthermore, the user subroutine allowed different casting times of concrete in the model. This capability allowed for the columns of a frame pier to be cast and exposed to shrinkage and creep before the cap beam.

Incorporating Temperature Effects

Thermal Properties

Structures exposed to the environment experience heat loss and gain through four primary sources: conduction with the ground, convection with the ambient air, radiation with the ambient environment, and solar radiation from the sun. To accurately model heat loss and gain from each source, the thermal properties of the structure are crucial.

Key thermal properties of any material include thermal conductivity, specific heat, and density. Additionally, the solar absorption of the material and emissivity of the material are important for modeling solar radiation and radiation heat loss/gain, respectively. Since the steel reinforcement composes a very small volume of the total structure, only the concrete is considered in the heat transfer analysis. Recommended thermal properties of the concrete are summarized in Table 4.1.

Table 4.1. Thermal properties of concrete

Thermal Property	Value	Source
Thermal Conductivity	1.31 W/(mK)	ACI 122 2002
Specific Heat	920 J/(kgK)	ACI 122 2002
Solar Absorptivity	0.60	Mills 1999
Emissivity	0.91	Mills 1999

Note that these values are recommended for general use and were later calibrated to field data for improved accuracy.

Heat flow due to convection can be expressed according to equation (4.4).

$$Q_{conv} = h(T_0 - T_{ambient}) \tag{4.4}$$

where Q_{conv} is the heat flow due to convection (W/m^2), h is the convection coefficient (W/m^{2}K), and $(T_0 - T_{ambient})$ is the difference in temperature between the surface of the material and the ambient air (K). The convection coefficient can be complex to calculate, as the coefficient depends on the Reynolds number and the temperature difference between the surface of the material and the ambient air (Mills 1999). However, empirical equations can calculate the convection factor for a generic surface depending only on wind speed (Bentz 2000, Karahan and Kalenderli 2011, Hwang and Jiang 2003). Equations (4.5) and (4.6) are used to calculate the convection coefficient (Bentz 2000).

$$h = 5.6 + 4.0u \qquad for\ u \leq 5\ m/s \tag{4.5}$$

$$h = 7.2 + u^{0.78} \qquad for\ u > 5\ m/s \tag{4.6}$$

where h is the convection coefficient (W/m^{2}K) and u is the wind speed (m/s).

These equations agree well with similar equations (Karahan and Kalenderli 2011, Hwang and Jiang 2003).

Heat flow due to solar radiation can be expressed according to equation (4.7).

$$Q_{solar} = \gamma Q_{irr} \tag{4.7}$$

where Q_{solar} is the heat flow due to solar radiation (W/m^2), γ is the solar absorptivity of the material as defined in Table 4.1, and Q_{irr} is solar irradiance (W/m^2). Solar irradiance only occurs during daylight hours and fluctuates with the weather and seasons. Clean Power Research partnered with University at Albany to provide a detailed solar irradiance database called SolarAnywhere. Hourly solar irradiance values from this database were used in the current FE model.

Heat flow due to radiation to/from the ambient environment can be expressed according to equation (4.8).

$$Q_{rad} = \sigma\varepsilon\left(T_0^4 - T_{sky}^4\right) \tag{4.8}$$

where Q_{rad} is the heat flow due to radiation (W/m^2), σ is the Stefan-Boltzmann constant (5.67×10^{-8} W/m^2/K^4), ε is the emissivity of the material as defined in the previous Table 4.1, T_0 is the surface temperature of the concrete, and T_{sky} is the temperature of the sky (K) which is assumed to be the same as the ambient air temperature.

Temperature Data

Weather data must be incorporated into a heat transfer analysis to accurately obtain a temperature field time history. These weather data include temperature, wind speed, and solar radiation. For the model validation with field data, actual weather data were used whenever possible. The exact temperatures for each day were used. Additionally, humidity and wind speed were averaged for the time period considered. Solar radiation was estimated based on historical records of the locations for the instrumented structures.

For the parametric studies, average weather data were used for each month of the year to avoid skewing the necessary weather data to the anomalies of any given year. Average daily high and low temperatures for each month from the National Oceanic and Atmospheric Administration (NOAA) were used (Arguez et al. 2010). The average temperature data from NOAA were calculated from 30 years of historical data from the Des Moines International Airport.

The solar radiation and wind speed data were obtained from SolarAnywhere, a software product that provides a databank of solar data. These data were calculated from visible and infrared satellite data and algorithms developed in collaboration with the University at Albany in New York (Perez et al. 2010).

To avoid anomalies, the hourly data from SolarAnywhere were averaged for each month. Given that wind speed varies more at night than during the day, wind speed values were averaged from the highest and lowest temperatures of the day. Additionally, solar irradiance only occurs with daylight, so a zero irradiance was applied during increments corresponding with the lowest temperature of a day.

To maintain computational efficiency, weather data were applied to the FE model in 12-hr increments during analysis. This compared well to weather data applied in 1-hr increments. Each 12-hr increment alternated between a day’s highest and lowest temperatures. Solar radiation was only applied during increments that corresponded to a day’s highest temperature. Additionally, wind speed data were applied uniquely during a day’s highest and lowest temperatures, given that less wind occurs at night.

Modeling in Abaqus

For computational efficiency, separate analyses were performed to account for heat transfer and stress. The resulting temperature field time history from the heat transfer analysis was applied to the 3D stress analysis to allow accurate thermal strains to develop due to temperature change. Running two analyses instead of one coupled thermo-displacement analysis reduced the number of unknowns and memory needed to run each analysis.

Abaqus supports heat flow due to convection through a surface film condition interaction, in which the film coefficient is equivalent to the convection coefficient and the sink temperature is equivalent to the ambient air temperature. Heat flow due to solar radiation can be performed in

Abaqus through a surface heat flux load with a magnitude equal to the heat flow due to solar radiation. Heat flow due to radiation is supported in Abaqus through a surface radiation interaction that accepts an emissivity value of the surface and an ambient temperature.

For model validation, the full temperature field time history was passed to the stress analysis, as previously described. This method provided the most accurate thermal profile within the members and was necessary to model with the accuracy needed to compare with field data. However, this method often caused convergence issues with the FE simulations. Therefore, for the remaining parametric studies, the temperature field time history was considered uniform for each member at any point in time, which was identical to how the selected shrinkage model applied shrinkage strain. The uniform temperature time histories were calculated by averaging the cross-sectional temperature at the center of each member. This simplification allowed the FE analysis to successfully run a much greater range of structural configurations.

Material Definitions

Concrete Material Definition

Strength Development

An important aspect in time sensitive analyses is the strength development of the concrete. The strength development affects the stiffness of the concrete in addition to the strength since the modulus of elasticity of concrete is dependent on its strength. Equation (4.9) is used to predict strength development of concrete according to ACI 209 (2008).

$$f_{c,t} = f_{c,28}\frac{t}{\alpha+\beta t} \tag{4.9}$$

where $f_{c,t}$ is the mean compressive strength of the concrete at an age of t days, $f_{c,28}$ is the 28-day mean compressive strength of the concrete, and α and β are constants dependent on cement type and curing method. The typical range of the α coefficient is from 0.05 to 9.25, and the typical range of the β coefficient is from 0.67 to 0.98.

The α and β coefficients in equation (4.9) were selected to match the strength development of concrete samples taken from a frame pier in Iowa during its construction. Six samples were collected, and their compressive strengths were tested at ages of 7 days and 28 days to capture the strength development of the concrete. A value of 2.5 was chosen for α and a value of 0.85 was chosen for β. Figure 4.1 shows a plot of equations (4.9) with calibrated coefficients compared to the experimentally obtained strengths of the concrete samples.

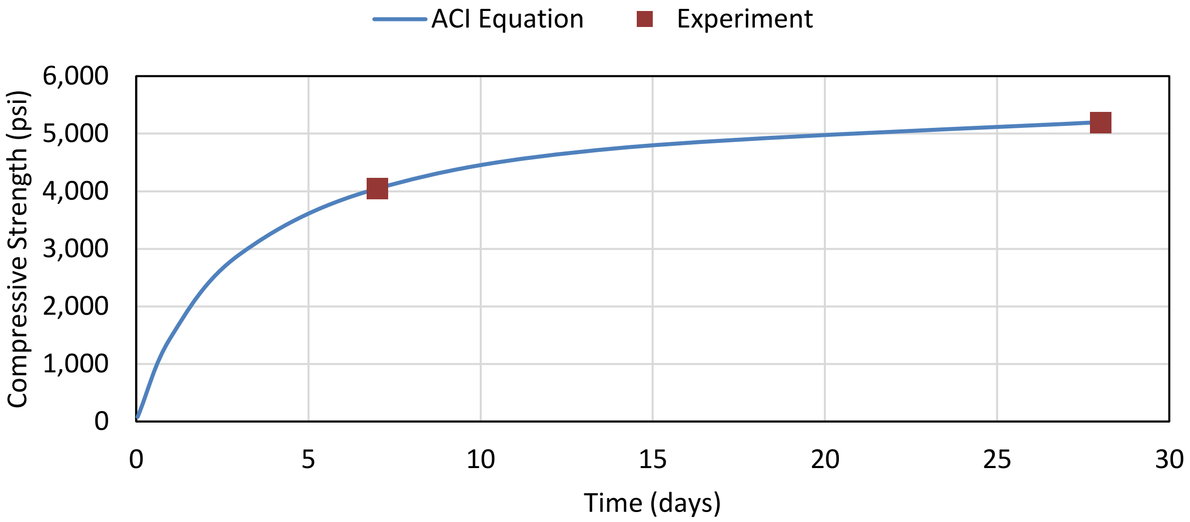

Figure 4.1. Calibrated strength development equation in comparison to recorded data

The strength development equation is used to account for both concrete strength and stiffness varying with time. The modulus of elasticity is calculated based on concrete strength according to equation (4.10) (ACI 318 2014).

$$E_c = 57{,}000\sqrt{f_c'} \tag{4.10}$$

In equation (4.10), E_c is the modulus of elasticity of the concrete in psi and f_c' is the compressive strength of the concrete in psi.

Abaqus allows material properties to depend on field variables. A field variable in the model is defined as the current value of total time of the analysis for each increment. Material properties, such as the modulus of elasticity or entire stress-strain curves, can then be input in tabular form dependent on time by using a field variable. Abaqus linearly interpolates between defined values as necessary when a property is defined based on field variables. Based on the calibrated strength development equation (equation (4.9)), several time points were selected to model the strength development of the concrete. The ages selected for Abaqus to use for linear interpolation were 1 hour, 1 day, 3 days, 7 days, 14 days, and 28 days. The strength development curve relying on linear interpolation for the development of the compressive strength and elastic modulus of the concrete are presented in Figure 4.2 and Figure 4.3, respectively.

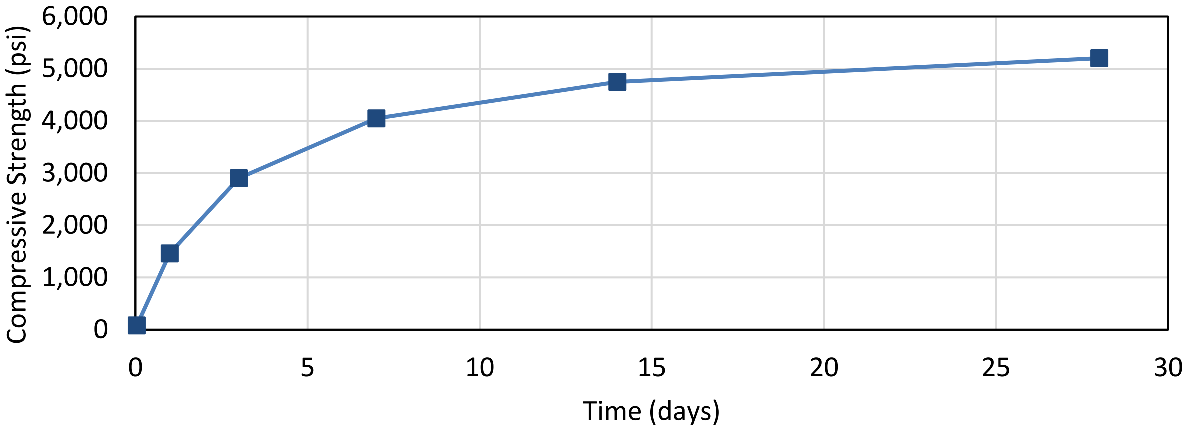

Figure 4.2. Strength development of concrete

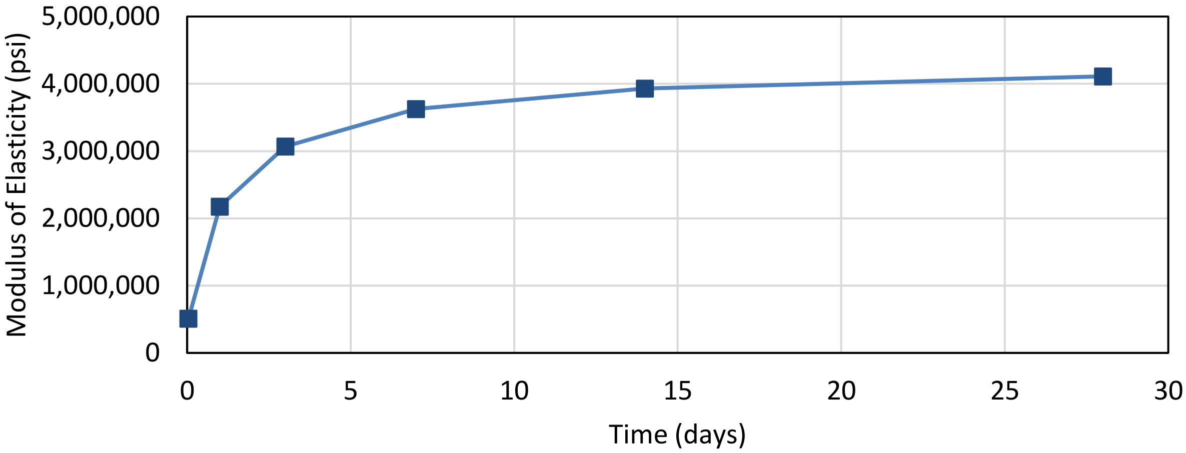

Figure 4.3. Modulus of elasticity development of concrete

The only remaining material property not previously defined in the heat transfer analysis was the coefficient of linear thermal expansion of the concrete. Using field data and recommended values in the literature, a value of 10.8×10^{-6} / °C was used as the coefficient of linear thermal expansion of the concrete (Mills 1999).

Inelastic Behavior

Modeling concrete in FE software is complex due to the nonlinear behavior of concrete in both tension and compression. Abaqus offers three methods for modeling the inelastic behavior of concrete: the smeared crack model, the brittle cracking model, and the concrete damaged plasticity model. All three models are intended for use on concrete materials at low confining pressures.

The smeared crack model can model the inelastic behavior of concrete under both compression and tension. However, cracking is assumed to be the dominant component of inelastic behavior, while compressive behavior is notably simplified for computational efficiency in the smeared crack model. Furthermore, the smeared crack model is intended for monotonic straining (Abaqus 2008).

The brittle cracking model, like the smeared cracking model, assumes cracking is the dominant inelastic behavior of the concrete. However, unlike the smeared crack model that accounts for some nonlinearity in the compressive behavior, the brittle cracking model treats any compression as purely elastic. A benefit of this model is that it offers a brittle failure criterion which can remove elements from the mesh (Abaqus 2008).

The concrete damaged plasticity (CDP) model is the most robust of the three models because it can handle variable loading and does not assume that cracking is the primary nonlinear behavior. This model accounts for damage in both compression and tension by reducing the stiffness of the concrete. This makes the CDP model a well-suited for general use. Since variable loading was part of this study, deriving from seasonal and daily temperature fluctuations, the CDP model was used in the current study (Abaqus 2008).

In the CDP model, the inelastic stress-strain behavior of the concrete was input in tabular format for both compression and tension behavior. The stress-strain curves were calculated according to Hsu and Hsu (1994). For compression, the nonlinear behavior of concrete includes both strain hardening and strain softening of the concrete to account for crushing. For tension, the nonlinear behavior only consists of strain softening due to the cracking behavior of concrete. The nonlinear behavior of the concrete needed to be input for various ages of the concrete to account for the strength development of the concrete. The stress-strain curves for all ages considered are presented in Figure 4.4 and Figure 4.5 for the compressive and tensile behavior, respectively.

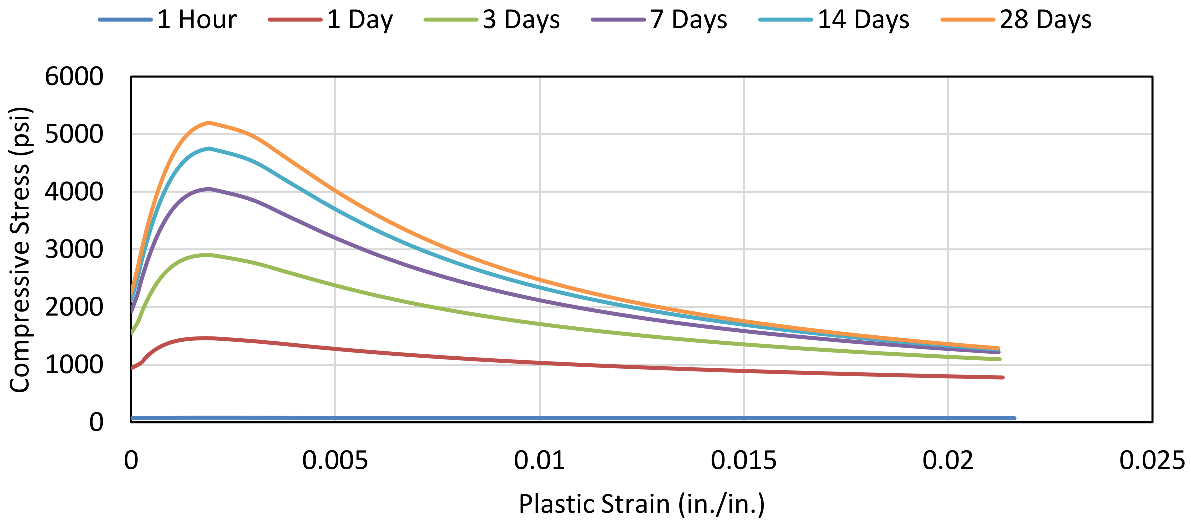

Figure 4.4. Stress-strain input for compressive behavior of concrete

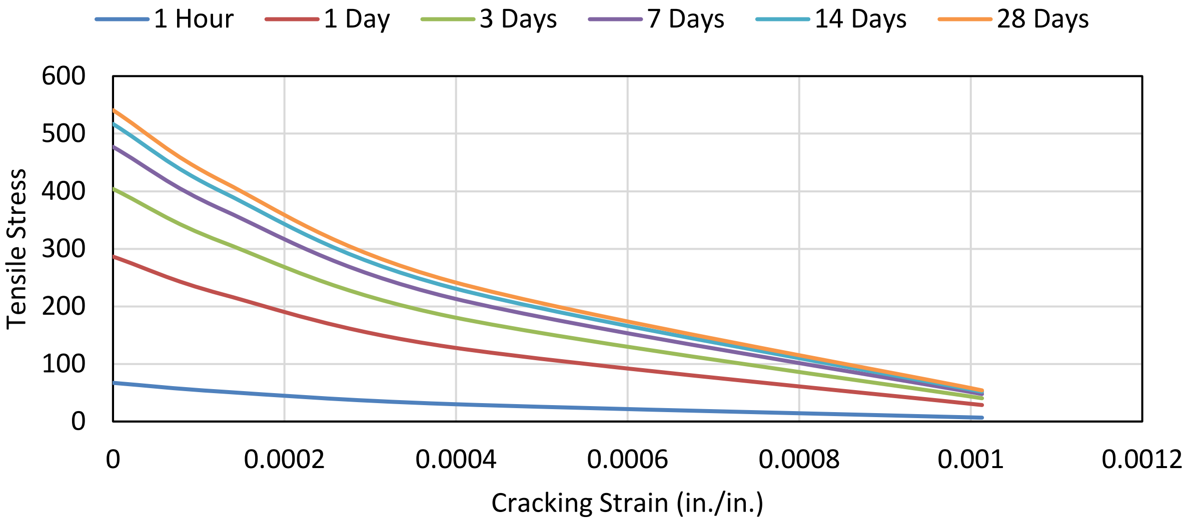

Figure 4.5. Stress-strain input for tensile behavior of concrete

The CDP model supports damage parameters. Under variable loading, damage parameters reduce the stiffness of the concrete due to damage caused by previous loading. Damage parameters are critical to accurately capture the behavior of concrete due to variable loading. A damage parameter of unity represents complete loss of strength, while a value of zero represents undamaged concrete (Sümer and Aktaş 2015). The damage parameters can be defined based on stress-strain data for the concrete and are defined as the cracking strain or inelastic strain over total strain for tension or compressive damage, respectively (Wahalathantri et al. 2011). Damage parameters are incorporated by Abaqus as defined in equations (4.11) and (4.12) for tension, t, and compression, *c* (Abaqus 2008).

$$\sigma_t = (1 - d_t)E_o\left(\varepsilon_t - \tilde{\varepsilon}_t^{pl}\right) \tag{4.11}$$

$$\sigma_c = (1 - d_c)E_o\left(\varepsilon_c - \tilde{\varepsilon}_c^{pl}\right) \tag{4.12}$$

where σ is the stress, d is the damage parameter, E_o is the undamaged modulus of elasticity, ε is the total strain, and $\tilde{\varepsilon}^{pl}$is the equivalent plastic strain. Due to the generally monotonic straining the models in this study experienced and the fact that tensile plastic strain was expected to occur more prominently than compressive plastic strain in concrete, only the tensile damage parameters were used in the current study. The tensile damage parameters were also beneficial to include since they helped visualize cracking in the concrete.

In addition to the stress-strain data, the CDP model needs several parameters to be defined. The ratio of the second stress invariant on the tensile meridian to that on the compressive meridian at initial yield must be defined and has a recommended value of 0.667. The dilation angle accounts for the increase in plastic volume once the concrete begins behaving inelastically under pressure. The eccentricity value represents the eccentricity of the plastic potential and has a recommended value of 0.1. The ratio of initial equibiaxial compressive yield stress to initial uniaxial compressive yield stress has a recommended value of 1.16. The viscosity parameter alters the damage zone, with a larger value diffusing the damage zone over a larger space (Michał and Andrzej 2015, Sümer and Aktaş 2015, Abaqus 2008).

The viscosity parameter of the CDP model represents relaxation time and allows for viscous regularization of the model. Viscous regularization is a useful tool for solving convergence issues with the CDP model that arise in the softening regime of the material. According to the Abaqus user manual, as long as the viscosity parameter remains small in comparison to a typical time increment, the results of the analysis should be accurate (Abaqus 2008).

The typical time increment of the analyses performed for this study are much larger than the default for a static analysis. Even though all the analyses performed in this study are static, time must be considered to appropriately account for shrinkage and creep effects. Therefore, the time steps in this study are several times larger than the default time step of unity. This allows for substantially larger viscosity parameter values to be used than in other studies while still achieving accurate results from the model.

Through sensitivity analysis, values for the viscosity parameter and angle of dilation of the model that offer good convergence as well as accurate results were selected. The default value of the angle of dilation was found suitable. However, the default value of zero for the viscosity parameter was not used and instead a small value was used (in comparison to a typical time increment of each model).

Steel Material Definition

Steel material was needed for the reinforcement bars embedded in the concrete. The steel had a modulus of elasticity of 29,000 ksi, a yield stress of 60 ksi, and a Poisson’s ratio of 0.30. The inelastic behavior of the steel was considered bilinear, as shown in Figure 4.6.

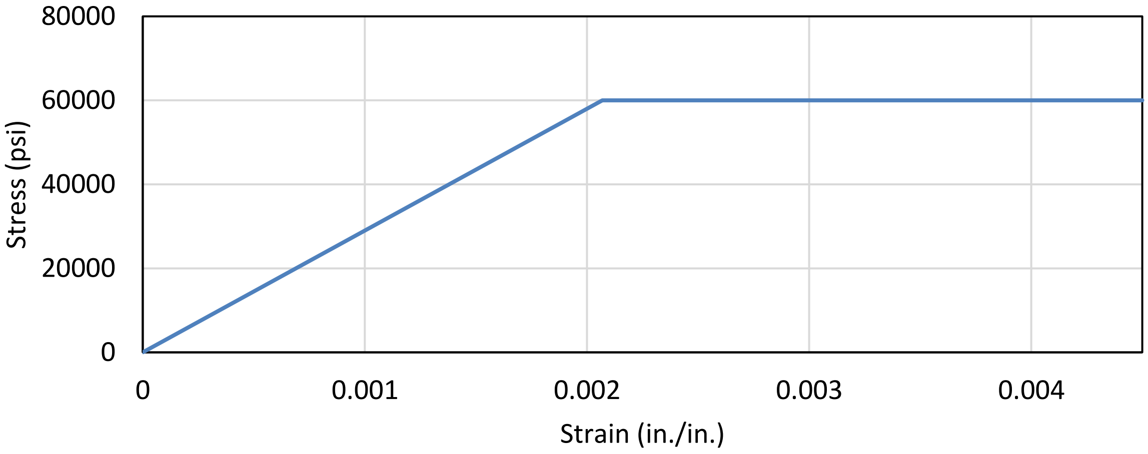

Figure 4.6. Inelastic behavior of streel material

Finally, a value of 11.7 × 10^{-6}/°C was used as the coefficient of linear thermal expansion of the steel.

Boundary Conditions, Interactions, and Dead Load

Boundary conditions are important, especially for structures that experience volumetric changes. If a fixed boundary condition is applied to the surface of a member that experiences volumetric changes, the boundary condition will fully restrain the surface that it is applied to and cause a substantial stress concentration. This stress concentration is generally unrealistic, as is the case for columns attached to a pile cap since the pile cap would also experience some level of volumetric change as well.

To avoid an unrealistic stress concentration, the base of each column was coupled to a reference point through a structural distributing coupling. This approach allowed any boundary condition with various levels of fixity to be applied to the reference points while allowing the column bases to expand and contract as necessary, therefore avoiding unrealistic stress concentrations.

According to the Iowa DOT BDM (2018), the column bases of frame piers are not fully fixed when piles are used for the foundation. Since piles are a common foundation choice for piers, the appropriate rotational stiffness needed to be accounted for in the model. This was achieved using springs. The reference points that were coupled to the column bases were fixed for every degree of freedom except in-plane rotation. A spring element was then applied to each reference point and connected to the ground. The active degree of freedom of the springs was set to in-plan rotation of the columns and a rotational stiffness was input. The rotational stiffness is calculated according to equation (4.13), as defined by the Iowa DOT BDM (Iowa DOT Office of Bridges and Structures 2018).

$$J = \frac{E_p I_p}{L_p} \tag{4.13}$$

where J is the rotational stiffness (kip-in./rad), E_p is the modulus of elasticity of the piles, I_p is the moment of inertia of the pile group (in.^{4}), and L_p is the effective pile length taken as 75% of the actual pile length for bearing piles and 50% of the actual pile length for frictional piles.

Stiff plates were attached to the bases of the columns. These stiff plates prevented high localized strains in the columns, and thus greatly improved the stability of the model. The stiff plates were subjected to the same thermal and shrinkage strains as the concrete they were applied to in order to avoid localized stress concentrations at the contact between the concrete and plates. The stiff plates did not experience the same Poisson's effect that the columns did. However, the inclusion of the stiff plates was found to improve convergence of the model, even without the inclusion of Poisson's effect in the material definition of the plates. The reinforcing steel was modeled as an embedded region within the concrete, as recommended for use with the CDP model (Abaqus 2008). An example of the embedded rebar in a model with 20 ft columns is presented in Figure 4.7.

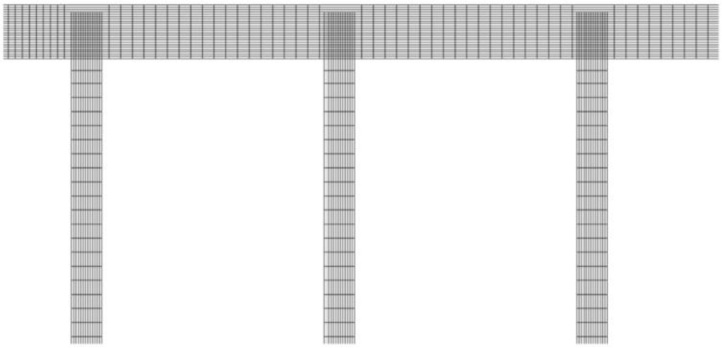

Figure 4.7. Embedded steel members

Dead load from the superstructure was applied to the cap beam of any modeled frame pier as a vertical pressure load that was applied to certain areas on the top surface of the cap beam. The areas where the pressure load was applied represented the beam seats of the cap beam, which are where the dead load of the super structure is transferred to the cap beam. An example of the locations of the application of superstructure dead load to a frame pier with 20 ft tall columns is presented in Figure 4.8.

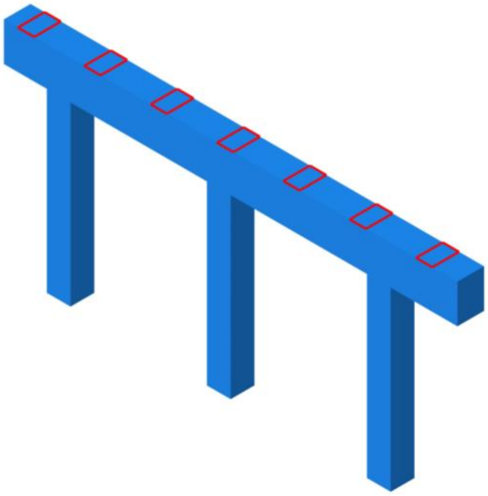

Figure 4.8. Locations of application of superstructure dead load

The additional stiffness added to the cap beam by the superstructure was assumed to be small and safely neglected. This was supported by observing small variation in vertical displacement along the length of the cap beam in many of the analyses performed in this study.

Mesh

Elements

Three-dimensional hexahedron elements are preferred in analysis due to their capability to provide accurate results with reasonable computational demand in many general use cases.

Therefore, the DC3D8 and C3D8R Abaqus element types were used for the concrete in heat transfer and 3D stress analyses, respectively. These element types were 8-node linear bricks that used reduced integration. For the one-dimensional rebar, the T3D2 Abaqus element type was used in the 3D stress analysis. This element type was a 2-node linear 3D truss that is recommended for use with the CDP model (Abaqus 2008).

Mesh Sensitivity

A comprehensive mesh sensitivity analysis was performed to ensure accurate results and maintain computational efficiency. Several measures of structural response were recorded to identify convergence of the results regarding mesh size: the reactions at the column bases, maximum stress in the steel reinforcement, maximum strain in the concrete, and maximum displacement of the column tops. The structure was determined to converge at a mesh size of two in. with hexahedron elements. However, for long asymmetric frame piers with large members, which were modeled in this study, this mesh size would impose great computational cost. Therefore, another set of analyses were performed while increasing the mesh size at locations of the structure away from areas of interest. Through an iterative process, it was determined that only the tops of the columns and the regions of cap beam above the columns (and extending beyond the column faces) needed a 2 in. mesh. The remaining areas of the structure were assigned a 4 in. mesh, which was determined to maintain accurate results and provide computational efficiency. The final selected mesh size is provided in Figure 4.9 for frame pier with 20 ft tall columns.

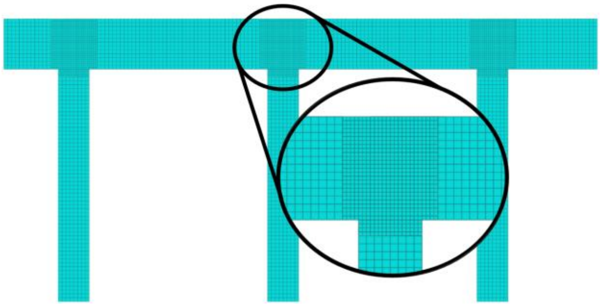

Figure 4.9. Final mesh configuration

Model Validation

An FE model of the instrumented frame pier of 418 Woodbury was created to validate the FE model. The geometry of the developed FE model of the instrumented frame pier is presented in Figure 4.10.

Figure 4.10. The finite element model of the instrumented frame pier

This model was further calibrated and validated through a comparison with field collected data. This comparison ensures that many aspects of the model were accurately represented, such as thermal properties, boundary conditions, joint interactions, nonlinear behavior, shrinkage strain, and creep strain. Two months of field data, beginning when the cap beam was cast, validated the numerical model. It was estimated that 43% of the expected ultimate shrinkage strain that the instrumented frame pier would experience occurred during this two-month period, based on the ACI shrinkage model. This shrinkage estimate considered an average humidity of 70% for a typical year in Iowa for calculating ultimate shrinkage and 78% for the predicted shrinkage during the two-month period (based on actual weather data). Environmental conditions and construction loads were applied to the model following the construction timeline of the instrumented frame pier shown in Table 4.2.

Table 4.2. Construction schedule for instrumented frame pier

Day	Construction Progress
0	Cap Beam Poured
10	Column Foundations Backfilled
25	First 4 Center Span Beams Placed
26	First 4 End Span Beams Placed
27	Final 4 Center Span Beams Placed
28	Final 4 End Span Beams Placed
54	Deck Formwork and Rebar Placed
63	Deck Poured
86	Half of South Barrier Rail Poured
89	Remaining Half of South Barrier Rail Poured
96	North Barrier Rail Poured

The results of the heat transfer analysis were compared with the field data. Modifications were made to the thermal properties of the concrete and some of the weather data. Only approximated weather data were modified (e.g., thermal radiation), and actual weather data were untouched (e.g., temperature data).

The thermal conductivity of the concrete was slightly increased to allow larger temperature fluctuations to occur within the cap beam, which better aligned the model to the field data. Additionally, special care was taken when modeling the temperature at the bottom of the column by considering the thermal effect of the backfill. Although the overall structural behavior of the structure was not significantly affected by the temperature of the columns below ground level, the thermal strain must be precise to accurately match the model results to the field data.

The heat of hydration was not modelled, as it was assumed to not affect the structural behavior of the frame pier due to the very early-age of the concrete when it occurs. The final temperature results of the model at key locations of the structure were compared to field data in Figure 4.11 through Figure 4.15.

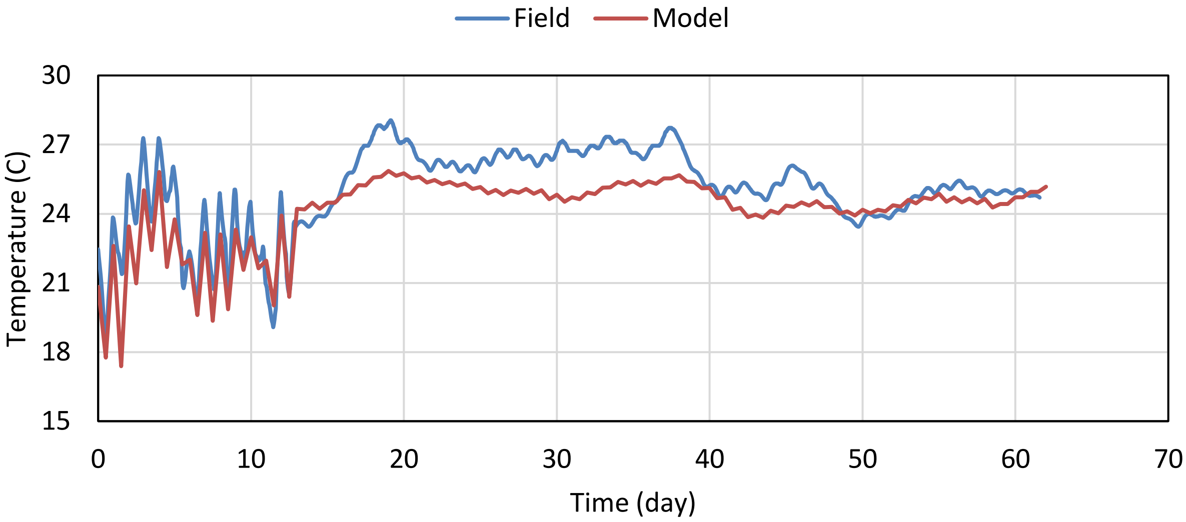

Figure 4.11. Thermal comparison between field data and the model at base of column

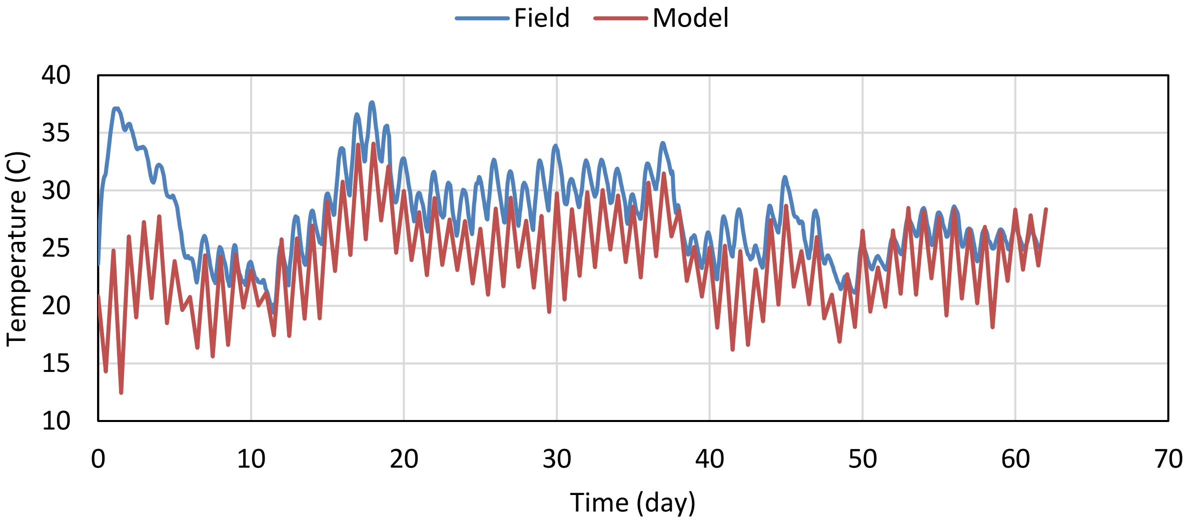

Figure 4.12. Thermal comparison between field data and the model at top of column

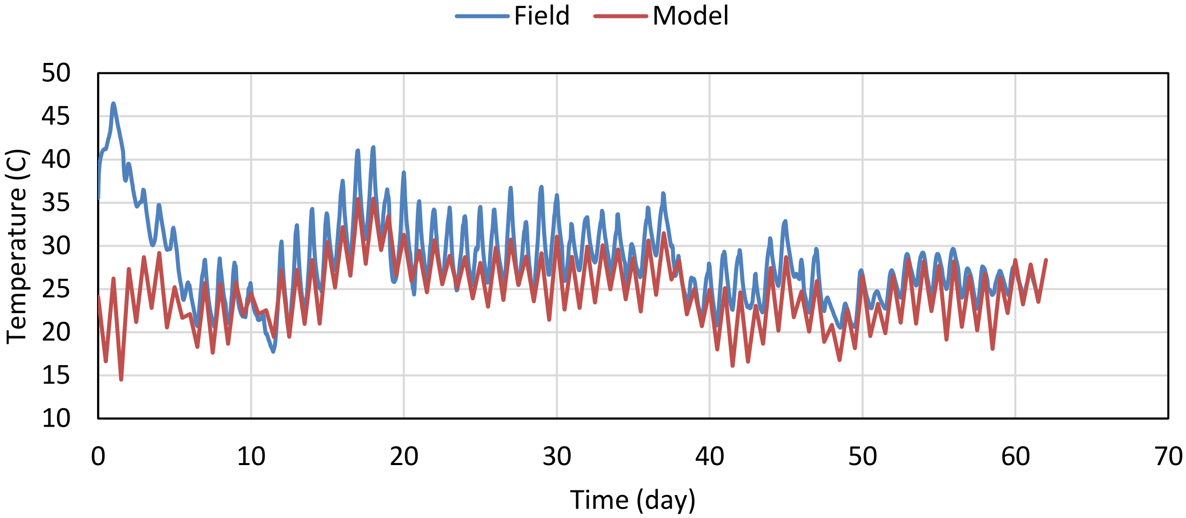

Figure 4.13. Thermal comparison between field data and the model at bottom of cap beam

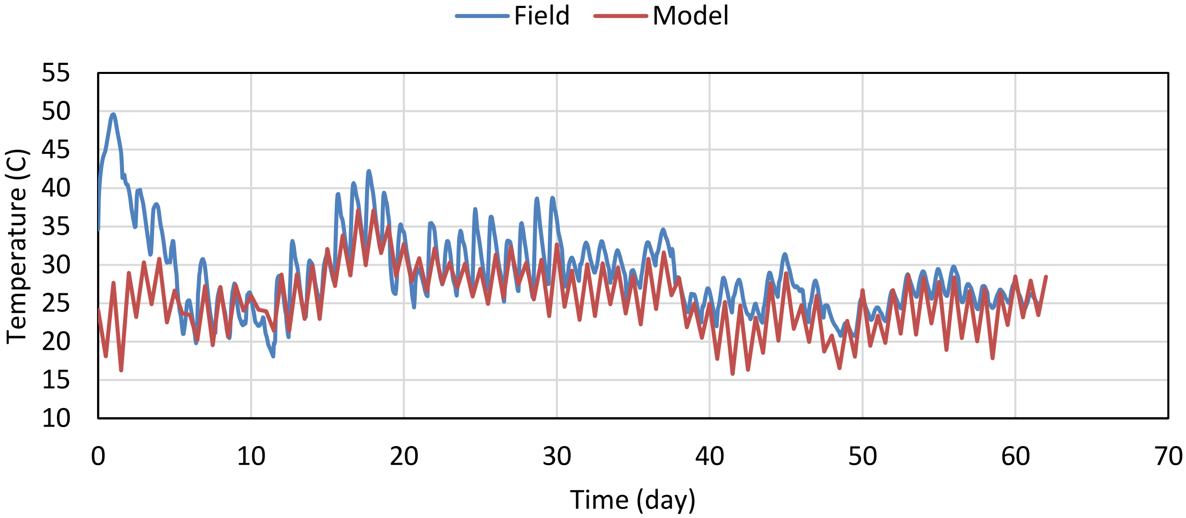

Figure 4.14. Thermal comparison between field data and the model at top of cap beam

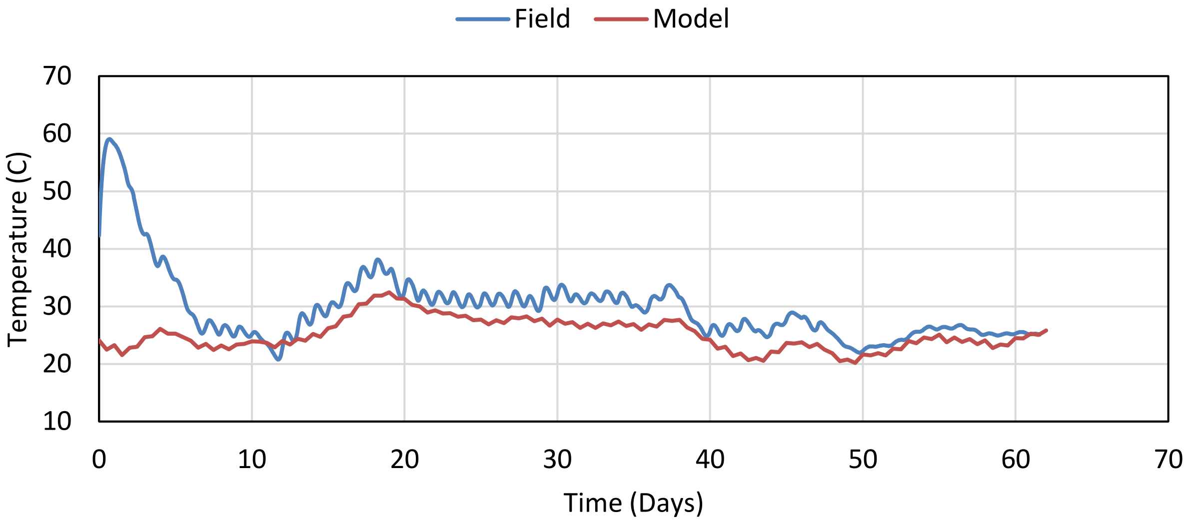

Figure 4.15. Thermal comparison between field data and the model near center of cap beam

Overall, these results show that the thermal gradients generated in the model were realistic to what occurred in the field, and thus appropriate for use in analysis. The developed thermal profiles of the model during the night and day at the end of the two-month period are presented in Figure 4.16.

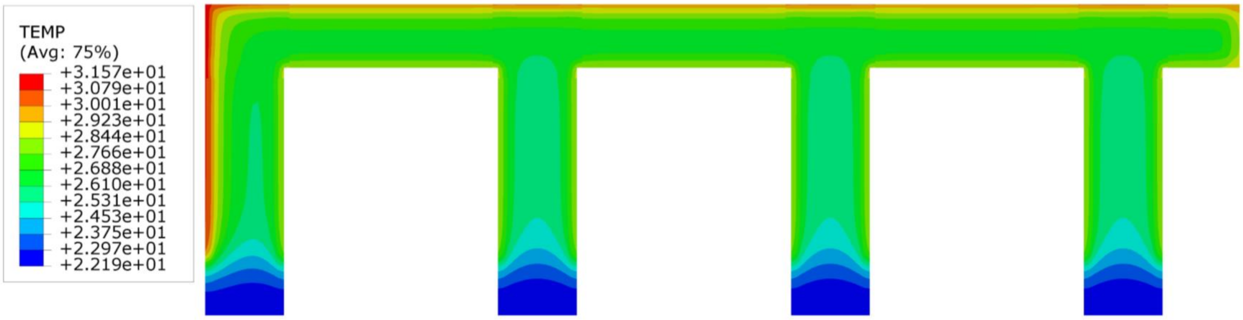

Day

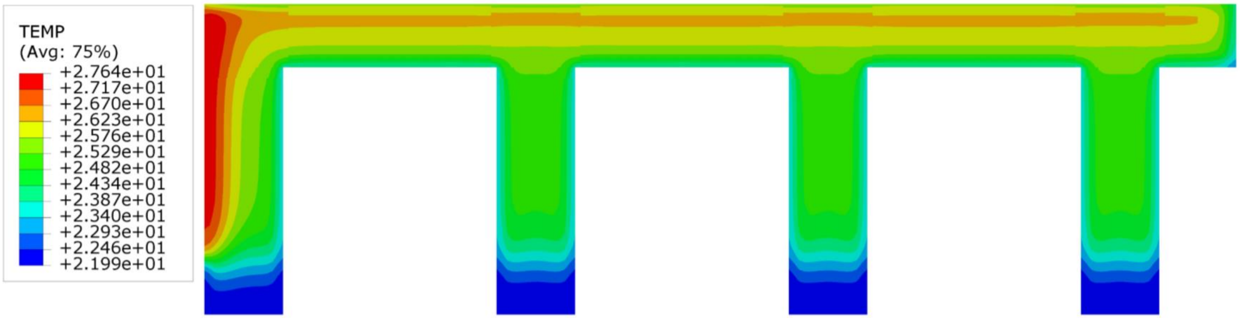

Night

Figure 4.16. Thermal simulated thermal profiles during the day and at night

The results of the 3D stress analysis were compared with field data. Parameters of interest when comparing theses data sets included the rotational stiffness of the column bases, the connection between the cap beam and column tops, and the application of superstructure dead load. All these parameters were approximated or simplified due to lack of resources or modeling requirements.

Generally, the structural behavior of the model matched well to the field data, as presented in Figure 4.17 through Figure 4.21.

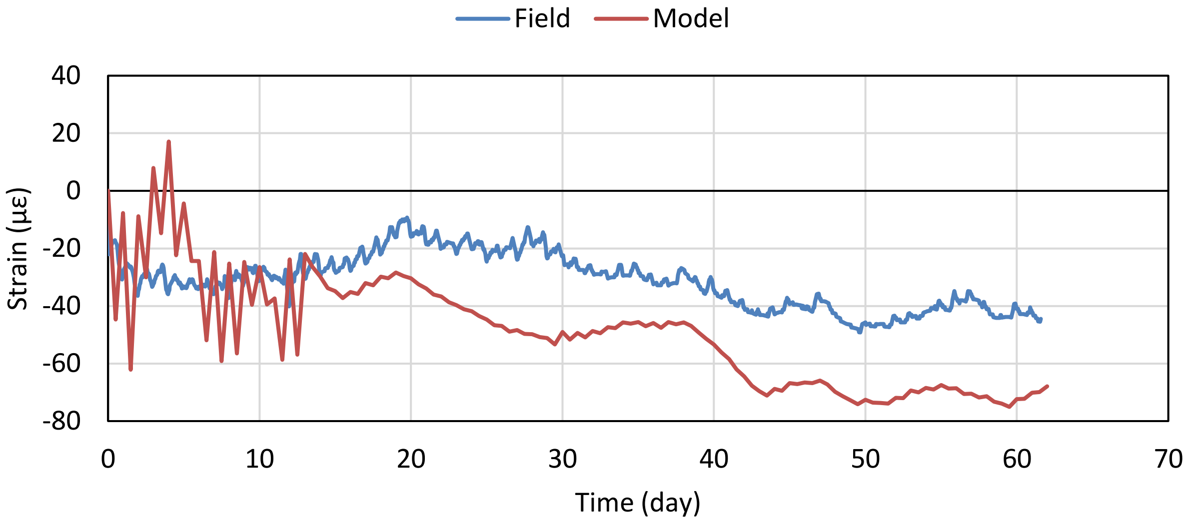

Figure 4.17. Strain comparison between field data and the model at base of column

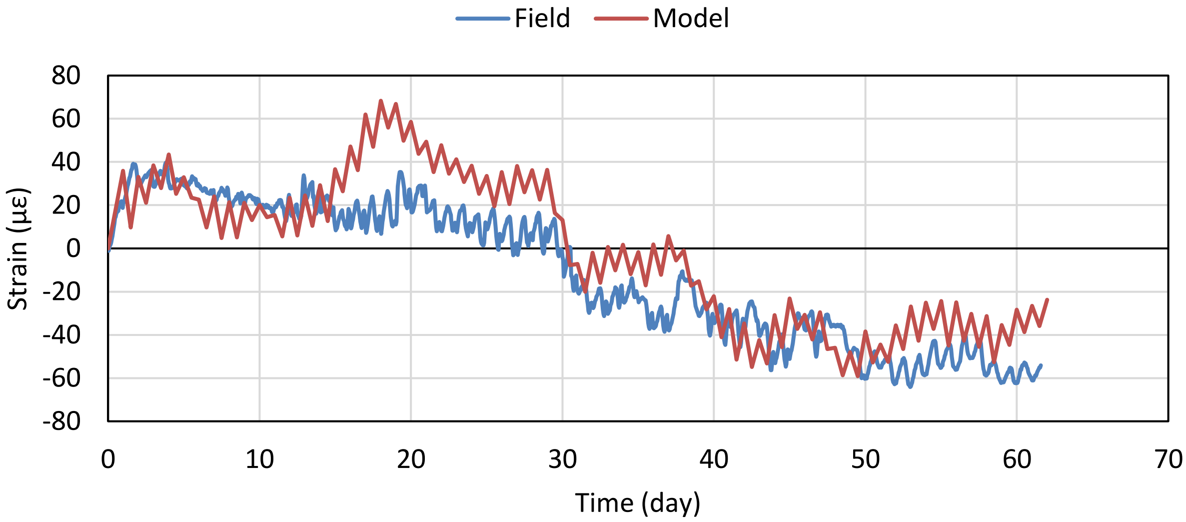

Figure 4.18. Strain comparison between field data and the model at top of column

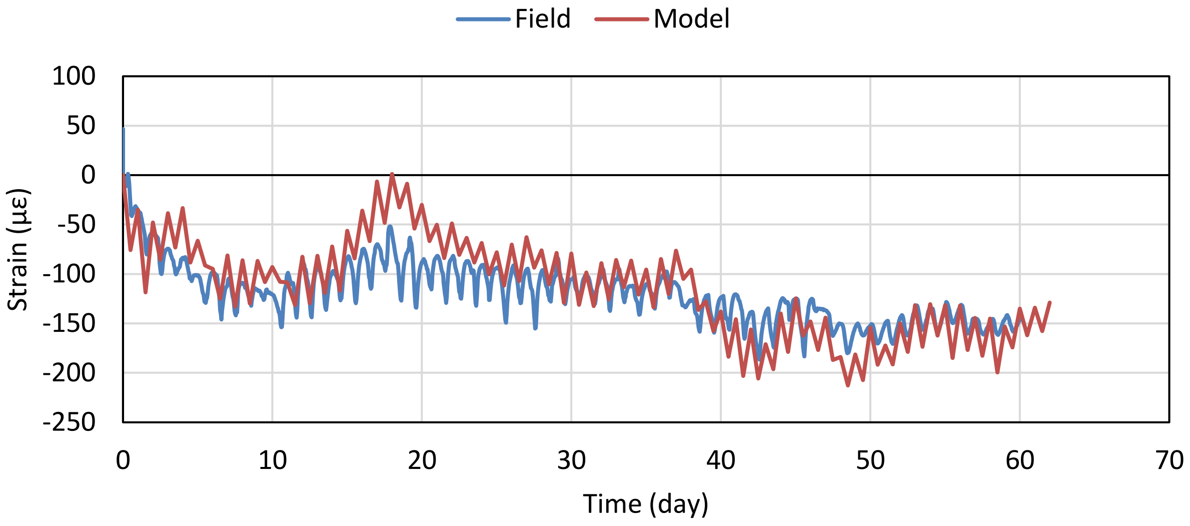

Figure 4.19. Strain comparison between field data and the model at bottom of cap beam

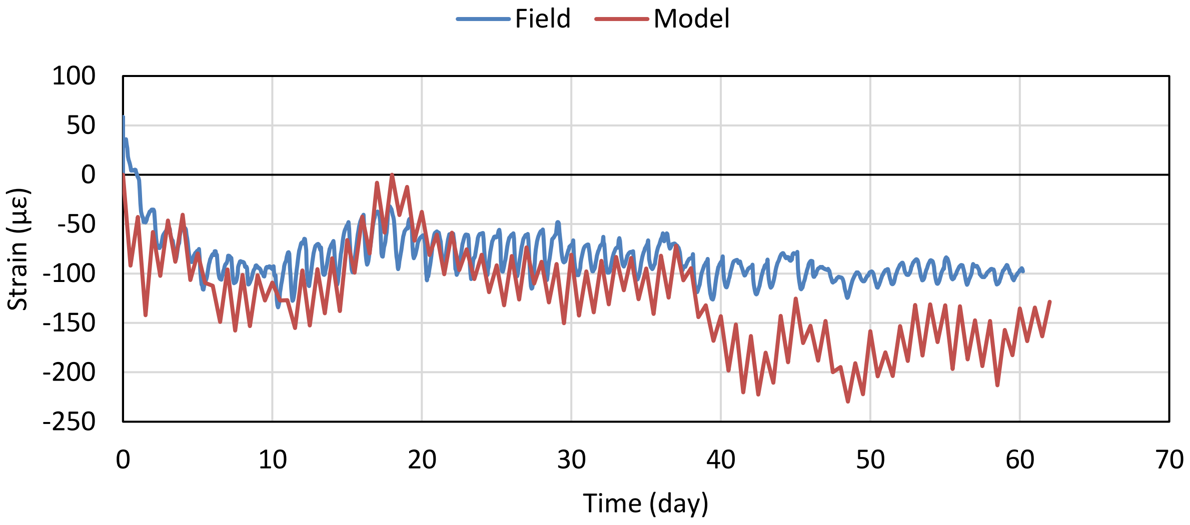

Figure 4.20. Strain comparison between field data and the model at top of cap beam

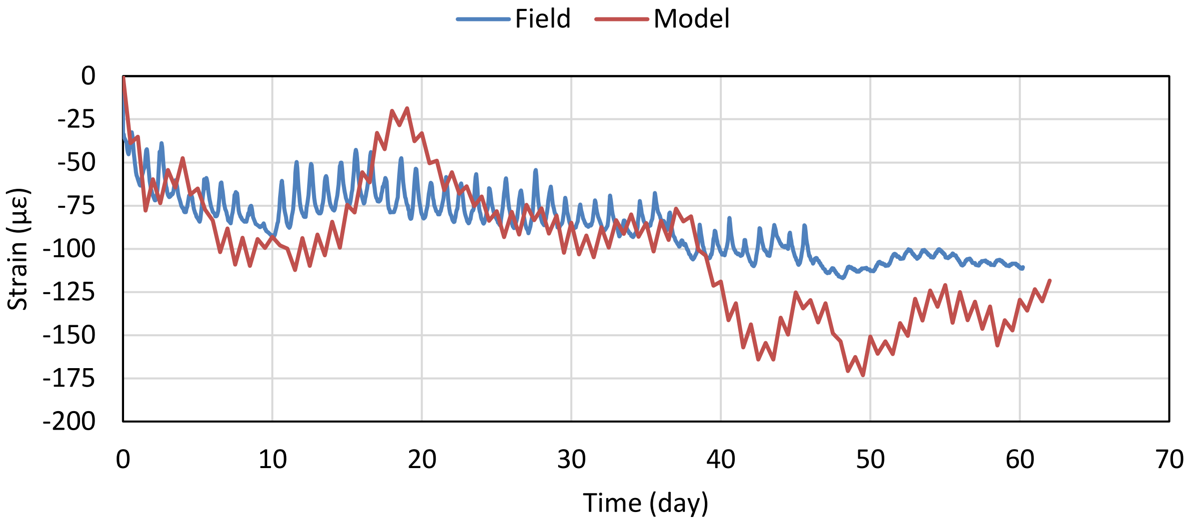

Figure 4.21. Strain comparison between field data and the model near center of cap beam

The displacement of the structure is visualized in Figure 4.22.

Figure 4.22. Displacement results of the FE model

The most notable discrepancy between the model and field data occurred at the column base. One reason for this discrepancy is that the initial temperature at the column was assumed uniform throughout the entire column. However, the column was cast several days before the cap beam was cast and thus developed a thermal profile. Rather than attempting to recreate this complicated thermal profile, a uniform temperature distribution was used, which mostly represents the temperature at the top of the column.

Another reason for the discrepancy was that the column base was exposed to a substantially different humidity than the rest of the pier since the column base was backfilled 10 days after the cap beam was poured. Burying concrete beneath soil will reduce the amount of shrinkage that occurs since moisture in the soil prevents the concrete from drying. Since the model did not consider this phenomenon, it was expected to simulate more shrinkage at the column base and thus more compressive strain. These two rationales explain why the model overestimated the compressive strain at the column base. This discrepancy was localized and not expected to affect the holistic structural behavior of the frame pier.

The remaining, less significant discrepancies between the model and field data included the model experiencing larger overall fluctuations in strain and a difference in the amplitude of diurnal strain at certain times. One reason for these variations was that the model considered the cap beam and columns to be monolithic, when there was actually a cold joint between these members.

The effect of altering the rotational stiffness at the column bases was investigated to improve the accuracy of the model. However, it was discovered that only very large changes in the rotational stiffness noticeably affected the results. Therefore, no modifications were made to the rotational stiffness from that predicted by equation (4.13) in the current study.

The long-term behavior of the model was found to match well with the field data. The long-term behavior was most important as that was when effects from temperature and shrinkage were most prominent several months after construction. Despite not having a full year of data collected at this point, the end of the two-month period of data was still observed closely.

Apart from the column base, the average strain of all the critical locations of the structure at the end of the considered time period were within 2.5% of the average strain of the field data. Considering that “it would be unrealistic to expect results from prediction models to be within plus or minus 20% of the test data for shrinkage” (ACI 209 2008), this small margin of error between the model and field data shows that the model accurately predicted the behavior of frame piers under temperature and shrinkage effects.

CHAPTER 5. PARAMETRIC STUDIES

Effects of Time of Casting

Purpose

Frame piers can be constructed throughout much of the year in Iowa. However, extremely cold times may be avoided since casting concrete in cold weather requires heating to protect the freshly poured concrete. The initial temperature at the time of casting is fundamental to the development of forces due to temperature. The combined effect of seasonal fluctuations in temperature and shrinkage are important and depend heavily on casting time. Therefore, the effect of casting time was investigated to identify a worst-case casting time, which was used throughout all remaining parametric studies.

Preliminary Analysis

An analytical investigation was performed prior to a more comprehensive FE analysis. The goal of this simplified analysis was to identify the most critical times of the year to cast a frame pier. The critical casting times identified in this preliminary analysis were then further investigated in a comprehensive FE analysis.

A yearlong shrinkage strain history was calculated according to the calibrated ACI shrinkage model, as shown in Figure 5.1.

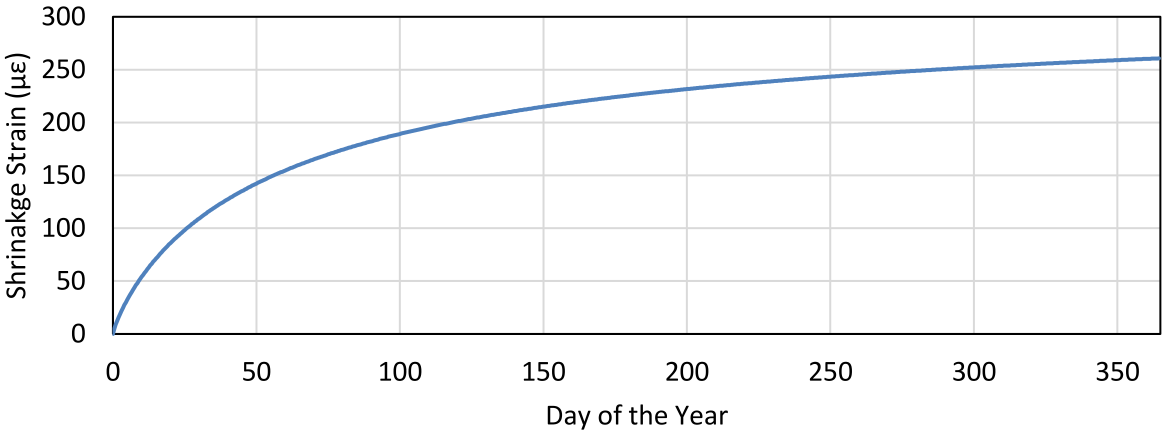

Figure 5.1. Shrinkage time history

Due to limitations of the shrinkage model, the relative humidity was assumed constant and a recommended value of 70% relative humidity was used (Iowa DOT Office of Bridges and Structures 2018). This assumption led to seasonal and daily weather effects having no effect on shrinkage strain. However, thermal strain is dependent on weather. The weather data time histories were used in a heat transfer analysis to obtain a time-dependent temperature field. Since the cap beam of a frame pier is the primary cause of restraint, an average temperature time history was obtained from the heat transfer analysis representing the cross section of the cap beam, as visualized in Figure 5.2.

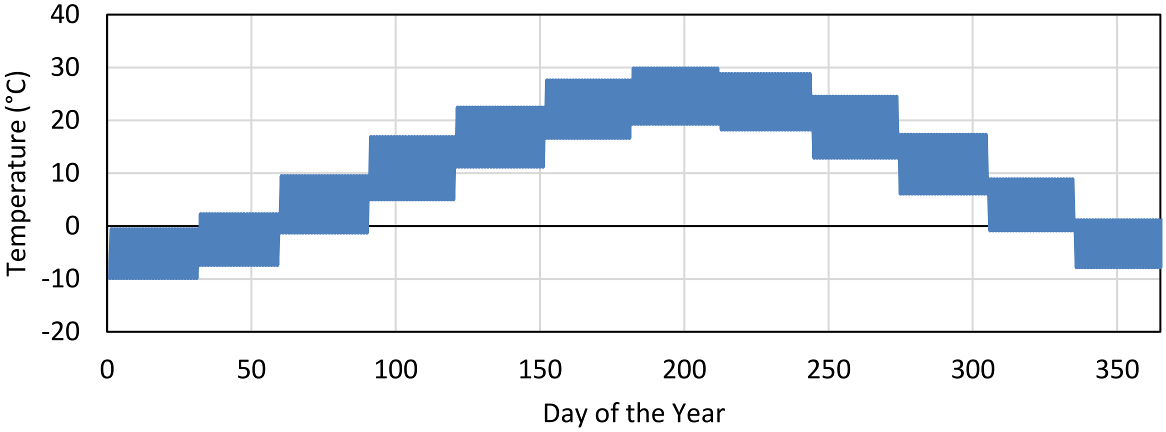

Figure 5.2. Temperature time history

A MATLAB script was developed to calculate the maximum and minimum strains the concrete would experience during the first year after casting considering shrinkage and thermal strain. The script calculated a strain time history due to the combination of thermal and shrinkage strain based upon a specified casting time. A total of 365 different casting times were considered, with initial temperatures equal to the average of the high and low temperatures of each day. For each casting time considered, the strain time histories were summarized by maximum compressive strain, maximum tensile strain, and the ages of concrete when each maximum strain occur.

A limitation to this approach was that creep strains were not considered. Additionally, loss of stiffness from previous strains before the maximum and minimum strains occur was neglected in this preliminary analysis. These limitations aside, the script was suitable to detect whether expansive strain or contraction strain was more critical and identify critical times of casting to further explore in a detailed FE analysis.

The results of this analysis made it clear that contraction strain was much more critical than expansive strain. As seen in Figure 5.3 and Figure 5.4, the compressive strain could reach a magnitude of around 570 microstrain, while the tensile strain can only reach a magnitude of about 90 microstrain.

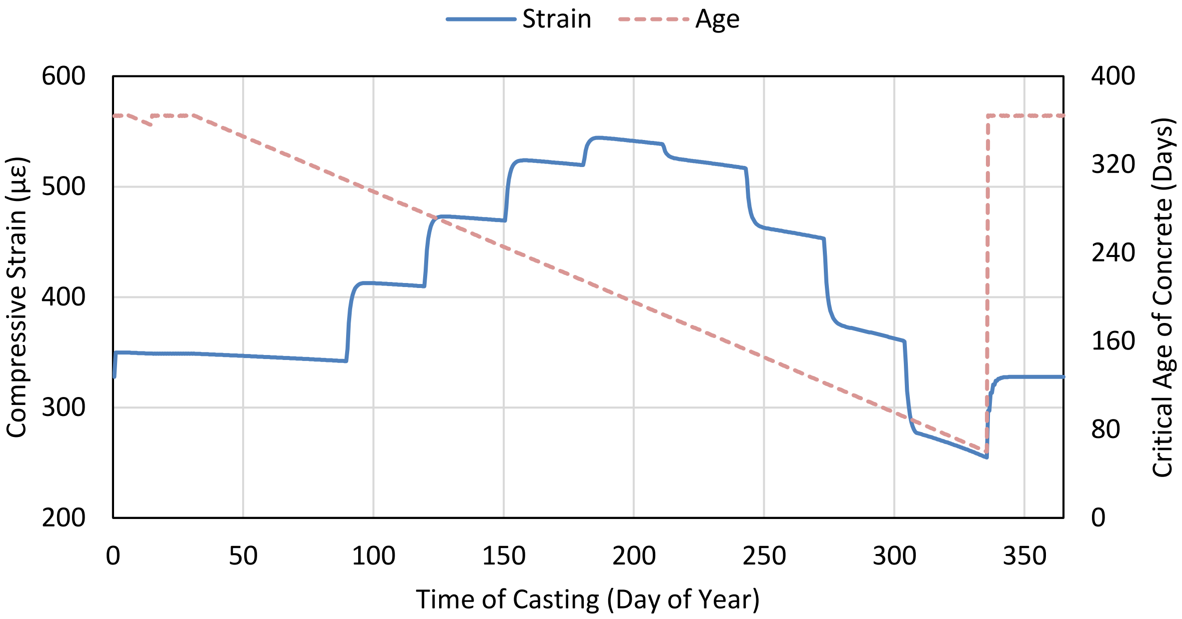

Figure 5.3. Analytically calculated maximum compressive strain for every casting time

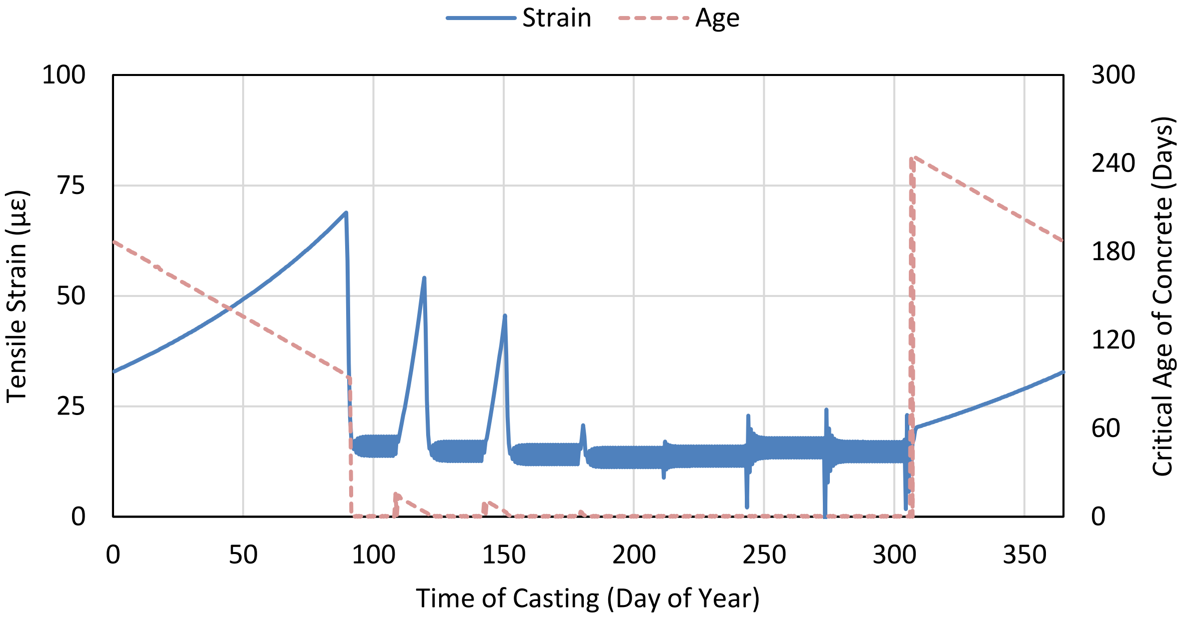

Figure 5.4. Analytically calculated maximum tensile strain for every casting time

This result was expected as shrinkage strain complements contractive thermal strain but reduces expansive thermal strain. Additionally, the temperature of the concrete at time of casting is not allowed to fall below 40°F (4.4°C) per standard construction specifications (Iowa DOT Highway Division 2015). This means that the difference between the initial temperature of the concrete and an extreme value will never be as large for expansive strain as for contraction strain. The most critical time of casting appears to be during summer. The age of concrete when it experiences the maximum contraction strains varies, generally decreasing in magnitude from spring to fall. Therefore, an FE analysis was warranted to account for creep effects as well as the nonlinear behavior of the concrete. The results of the developed MATLAB script allowed the FE analysis to solely focus on compressive strain, as that was identified as the most critical.

Another inference made from the results of the script was that thermal strains may play a larger role than shrinkage strain. This is due to almost all the considered casting times experiencing their maximum contractive strains on the same day (the end of January). This can be visualized by the linear relationship between the time of casting and age of the concrete when the maximum contractive strain occurs. In terms of magnitude, shrinkage strain and thermal strain were similar. However, thermal strains changed magnitude vary rapidly compared to shrinkage strain. This rapid change in strain will not be relaxed by creep as significantly as slowly developed strains, such as shrinkage strain. This limits the amount of creep relaxation thermal strains will experience and thus may lead to thermal strains playing a larger role than shrinkage strain in the behavior of the structure.

Four casting dates were selected for further analysis with the developed FE model: June 10th, July 10th, August 31st, and September 30th. The temperature time histories, showing only the daily lows for clarity, are provided in Figure 5.5 for each critical casting time.

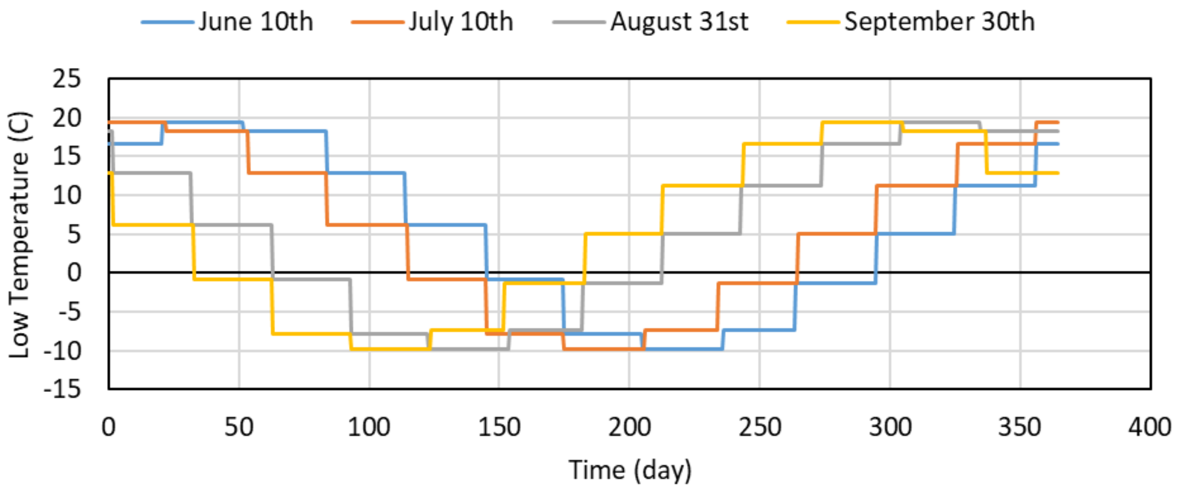

Figure 5.5. Low temperature time histories for each selected casting time

Each analysis simulated the full year of weather data that was previously used in the MATLAB script.

Creep Effects

To consider the effects of creep, an FE model was created. A single frame pier geometry representing a common frame pier in Iowa was selected to observe the effect of casting time. The selected frame pier geometry consisted of four cylindrical columns, each with a height of 10 ft, a diameter of 3 ft, and column spacing of 16 ft on center. The height of the columns was shorter than most frame piers to magnify the effects of volumetric change. The columns supported a cap beam with a length of 58.25 ft, a height of 3.25 ft, and a width of 3.25 ft. The cap overhang, measured from the center of the end column to the end of the cap, was 5.25 ft long.

The frame pier was symmetrical about its midpoint. The analysis took advantage of this symmetry, as only half of the frame pier was modeled with a symmetric boundary condition imposed on the right end of the cap beam to achieve computational efficiency. The foundation for each column was considered to consist of a pile cap and piles. The rotational stiffness of the pile group was calculated per the equation used (with 4.72×10^6 kip-in./radian). The heat transfer analyses were performed in a similar fashion to that performed in the model validation section where the actual temperature profiles from the heat transfer analysis are used. The FE model geometry used to investigate casting time is presented in Figure 5.6.

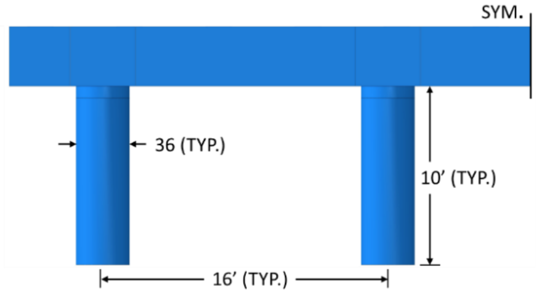

Figure 5.6. FE model of frame pier used in time of casting investigation

Results

The July 10 casting date resulted in the highest demand on the frame pier when considering column reactions and displacement, as summarized in Table 5.1.

Table 5.1. FE results for each casting time investigated

Casting Date	Max. Moment (kip-ft)	Max. Shear (kip)	Max. Displacement (in.)	Critical Age (days)
6/10/2019	344	74.8	0.151	235
7/10/2019	354	76.4	0.156	205
8/31/2019	335	73.2	0.148	153
9/30/2019	299	66.2	0.131	123

This maximum demand occurred during the lowest temperature, which was on the 205th day. Despite July 10 resulting in the maximum demand, any hot summer day is expected to result in a high demand due to shrinkage and temperature effects. For example, the average demand on the frame pier when cast on June 10th was only 2.6% lower than if cast on July 10.

Creep did not appear to significantly affect the results given the FE results reflected those of the MATLAB script, which neglected creep. In fact, the time histories that reached their maximum demand of the structure the fastest (i.e., as low as about 125 days) resulted in less demand compared to the time histories that took 200 days to reach their maximum demand on the structure. This can be attributed to the magnitude of creep diminishing with age. This means that, when a structure gradually reaches a high stress over a long period, less creep will result from that high stress compared to a structure that experiences the same high stress much earlier. This explains the results of the casting time analyses given that the analyses that took the longest resulted in the highest demand on the frame pier despite allowing for creep over a longer period. Full time histories of the moment at the base of the outer column are presented in Figure 5.7.

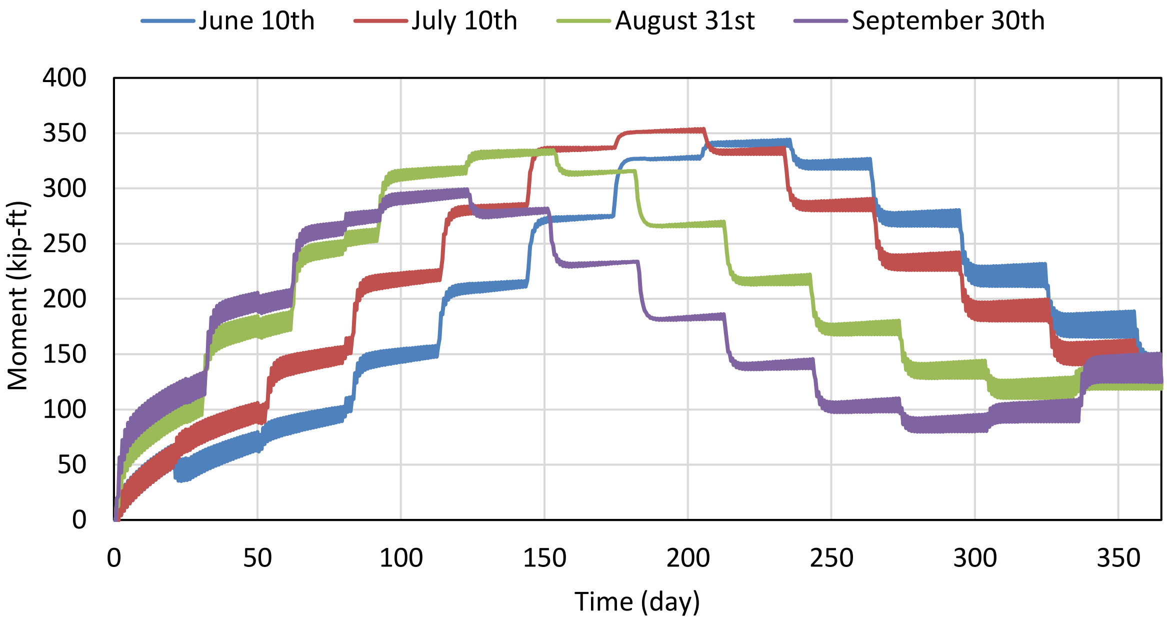

Figure 5.7. Moment reaction at exterior column base for each casting time investigated

Based on the FE results investigating time of casting, all subsequent analyses consider the cap beam cast on July 10th and consider a time history 215 days.

Effects of Column Stiffness

Purpose

Column stiffness affects the performance of frames under volumetric change. However, some design guides focus solely on frame length when determining design decisions regarding temperature and shrinkage effects in frame piers. For example, the bridge design manuals created by Illinois and Nebraska consider only the length of a frame pier when determining whether to place a joint in the cap beam or include temperature and shrinkage effects in design. Furthermore, studies often attempt to summarize the effect of column stiffness as dependent on only the height of a column. This has led to metrics such as the length-to-height ratio being utilized when identifying the susceptibility of a frame to volumetric changes.

While column height is critical in determining column stiffness, frame piers are known to have strong and weak moments of inertia due to rectangular cross sections. In some cases, the difference between the strong and weak moments of inertia is significant. For example, the columns of an existing frame pier in Dubuque, Iowa, have a strong moment of inertia that is 300% larger than their weak moment of inertia. This makes it crucial to consider column orientation when considering whether a frame pier is vulnerable to volumetric changes. Furthermore, material strength and the rigidity of the connections at the top and base of a column affect overall column stiffness.

Three methods were used to vary column stiffness of a frame pier. Method 1 varied column stiffness uniformly for all columns, meaning that all columns had equal stiffness. Method 2 varied column stiffnesses such that the outer columns differed from the interior columns. Method 3 varied column stiffness linearly along the length of the frame pier. This final case occurred most often when the heights of the columns varied to accommodate a sloped grade. The goal of this investigation was to understand the effect of column stiffness on the overall structural performance of frame piers.

Finite Element Analysis

The base case for the column stiffness investigation consisted of a frame pier with 20 ft tall columns and a length of 90 ft from the centerline of exterior column to the centerline of the exterior column. This frame pier geometry was based on an existing frame pier in Iowa that uses a common column size, 3 ft diameter columns modeled as square columns with a cross-section of 32 × 32 in. to increase model stability and maintain similar stiffness.

However, this frame pier was designed with more flexible columns with a height of 27.8 ft. This allowed the effects of flexible columns to be realistically shown. The frame pier was designed with tall, flexible columns which could be shortened to increase column stiffness while remaining adequately designed for supporting gravity loads. The frame pier supported prestressed concrete girders spaced 7.5 ft on center and an average bridge span of about 79 ft.

Only the dead load of the structure and forces due to temperature and shrinkage effects were considered in the analysis.

For every case considered, only the column stiffnesses were altered from the base case and all other components of the frame pier remained constant: including material properties, rebar configuration, rotational stiffness at the column bases, cap beam dimensions, column spacing, shrinkage strain development, dead load applied to the cap beam, and temperature history.

In the Method 1 cases, column stiffness was varied through two different approaches. The first approach only altered the height of the columns to alter column stiffness. This maintained consistent connections between the cap beam and columns. Column heights of 10, 11, 15, 20, and 27.8 ft were considered.

The second approach altered the cross-sectional shape of the column to vary the moment of inertia of the column. This also altered the behavior of the connections between the cap beam and columns. Only the width of the columns was increased as this dimension has the most effect on the moment of inertia of the columns. Therefore, the columns maintained a depth of 32 in. Column moments of inertia of 4.2, 14.2, 22.6, 33.7, and 48.0 ft^4 were considered (which corresponded to column widths of 32, 48, 56, 64, and 72 in.). The cases considered in Method 1 are presented in Figure 5.8 and Figure 5.9.

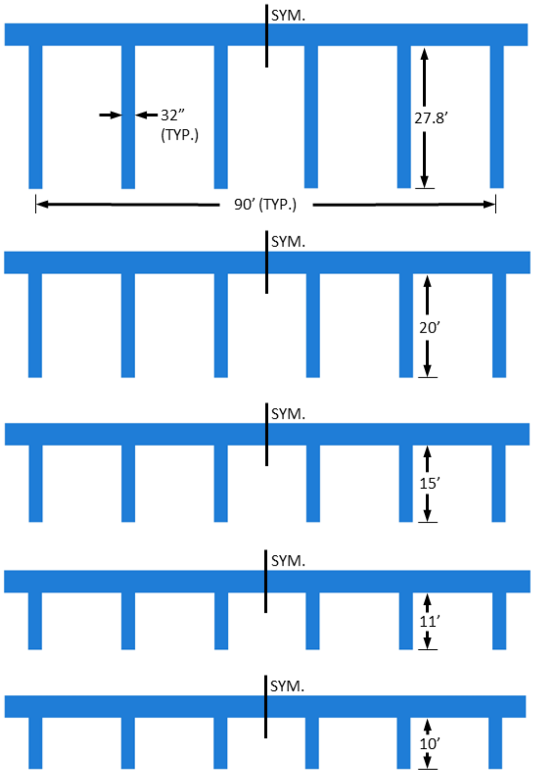

Figure 5.8. Uniform column height cases considered

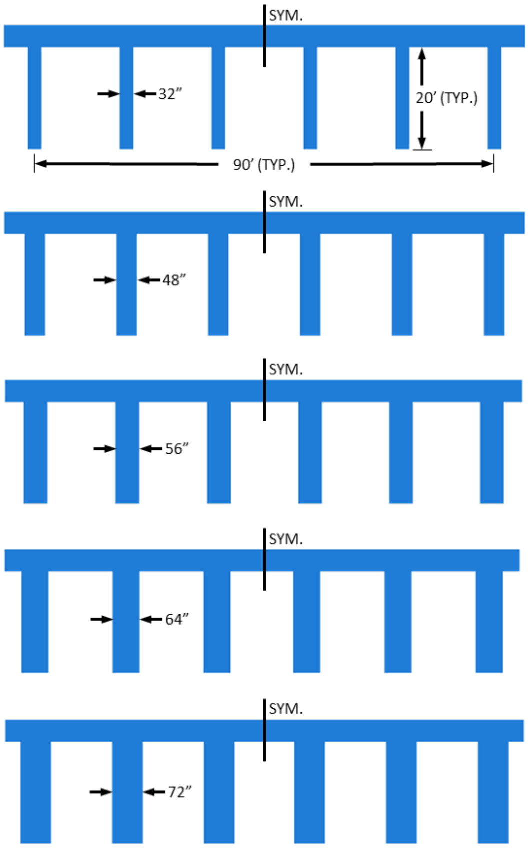

Figure 5.9. Uniform column shape cases considered

The cases considered in Method 2 only altered the cross-sectional shape of the columns. The cases considered in Method 2 are presented in Figure 5.10.

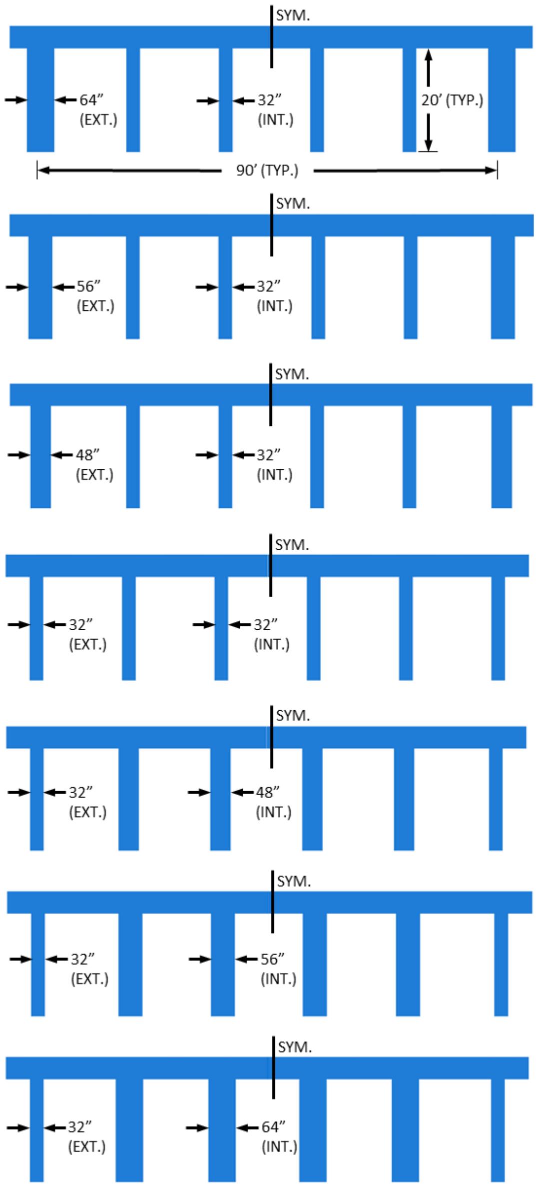

Figure 5.10. Exterior versus interior nonuniform column stiffness cases considered

The geometries in Figure 5.10 correspond to I_{Ext}/I_{Int} values of 0.1, 0.2, 0.3, 1.0, 3.4, 5.4, and 8.0, where I_{Ext}/I_{Int} is the ratio of the gross moment of inertia of an exterior column to an interior column. Method 3 considered one case in which the column height of the base case decreased linearly along the length of the frame pier from a height of 20 ft to 15 ft, as presented in Figure 5.11.

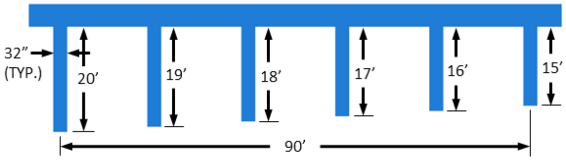

Figure 5.11. Linearly varied column stiffness case considered

Several measurements of performance and demand of the structure were extracted from the results of each case. The maximum shear at a column base, maximum moment at a column base, minimum vertical load at a column base, maximum lateral displacement of the top of an exterior column, maximum cracking strain of the structure, and maximum rebar stress were all extracted.

Method 1 Results

For every column height case, the maximum shear and moment reactions of a column occurred at the exterior column. However, in two column shape cases, the maximum column base shear occurred at the outermost interior column. These two cases were the stiffest column shape cases considered (i.e., column widths of 64 in. and 72 in.). The shifting location of the maximum base shear was attributed to the top of the interior column experiencing more restraint from the cap beam, which spanned on both sides of the column, than that experienced by the exterior column. Despite the maximum shear reaction occurring at an interior column in two cases, the maximum moment reaction occurred at the exterior column in every case considered. Maximum shear reactions of each column for every column shape case are presented in Figure 5.12.

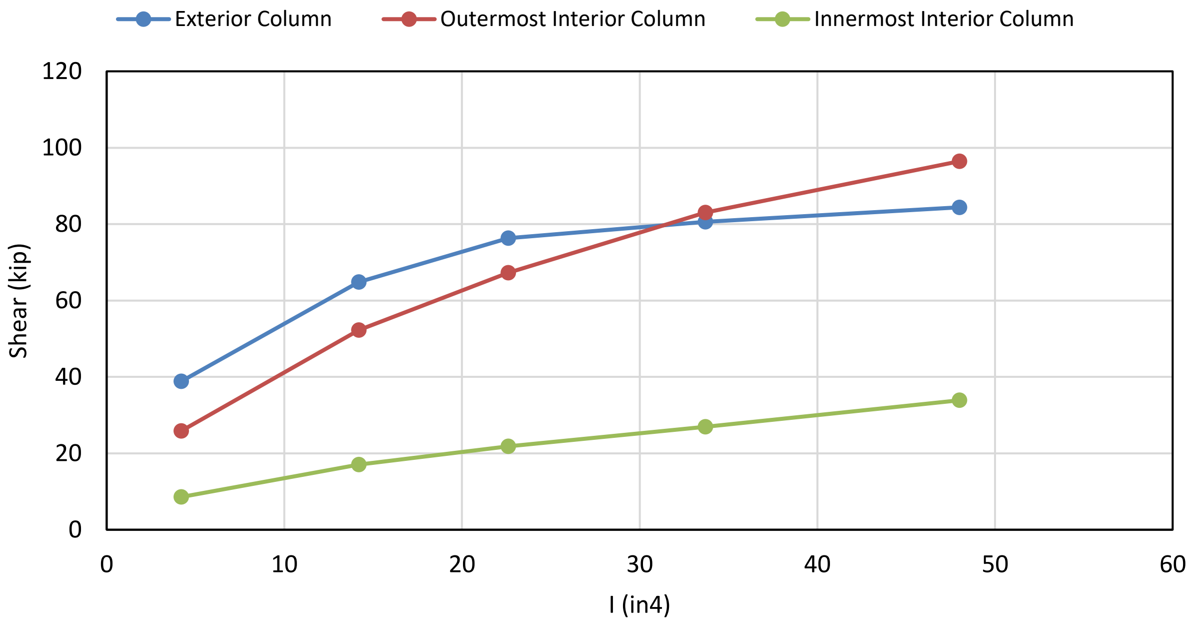

Figure 5.12. Maximum shear reaction of each column in the column shape cases

Maximum shear at the interior column was only 1.8% that of the exterior column in the stiffest column height case considered, a column height of 10 ft.

The results of uniformly varying the column stiffness show that column stiffness significantly affects the behavior of frame piers subjected to temperature and shrinkage effects. Decreasing the column height from 27.8 ft to 10 ft increased the shear at the exterior column by 633% from 17.6 kips to 129 kips. Increasing the moment of inertia of the columns from 4.2 ft^4 (i.e., the base case) to 48.0 ft^4 increased the shear at the outer column by 148% from 38.8 kips to 96.4 kips. In both the column height and column shape cases, the moment reaction did not increase as substantially as the shear reaction did. Decreasing the column height increased the moment reaction by 177% and increasing the moment of inertia of the columns increased the moment reaction by 48.7%.

It is well-known that the lateral stiffness of a column is proportional to the expression in equation (5.1).

$$k \propto EI/L^3 \tag{5.1}$$

where k is the lateral stiffness of the column, E is the modulus of elasticity, I is the moment of inertia, and L is the column height. The results of all the cases considered in Method 1 are presented in terms of EI/L^3 in Table 5.2 and Table 5.3 to draw direct comparisons between the cases.

Table 5.2. Maximum FE results from the column height cases

EI/L^3 (kip/in.)	Column Height (ft)	Shear (kip)	Moment (kip-ft)	Lateral Disp. (in.)	Cracking Strain (με)	Rebar Stress (ksi)
207.9	10.0	128.6	621.8	0.252	7,435	37.9
156.2	11.0	113.8	603.5	0.256	6,592	31.6
61.6	15.0	68.0	472.4	0.266	4,087	21.5
26.0	20.0	38.8	350.5	0.272	510	15.6
9.5	27.8	17.6	224.4	0.277	0	10.6

Table 5.3. Maximum FE results from the column shape cases

EI/L^3 (kip/in.)	Moment of Inertia (ft^4)	Shear (kip)	Moment (kip-ft)	Lateral Disp. (in.)	Cracking Strain (με)	Rebar Stress (ksi)
26.0	4.2	38.8	350.5	0.272	510	15.6
87.7	14.2	64.8	496.4	0.264	3,039	15.2
139.3	22.6	76.3	518.6	0.258	2,924	18.6
207.9	33.7	83.0	521.2	0.253	5,062	24.5
296.0	48.0	96.4	507.3	0.243	5,827	34.9

The shear reaction at the exterior column bases increased as column stiffness increased. However, the increase in shear significantly tapered off at higher column stiffnesses, as can be seen in Figure 5.13.

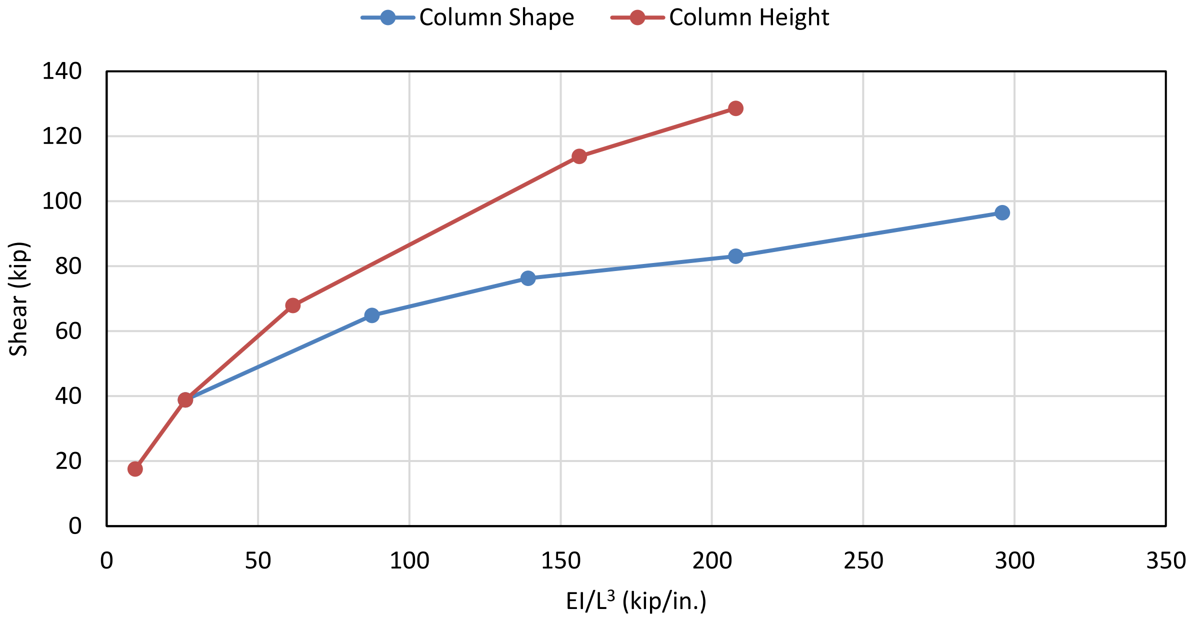

Figure 5.13. Maximum shear reactions of each uniform column stiffness case

This tapering can be attributed to creep and cracking of the concrete relaxing stress in the structure. The moment reaction at the exterior column base behaved similarly to the shear reaction. However, the tapering effect was even more prominent for the moment reaction, as seen in Figure 5.14.

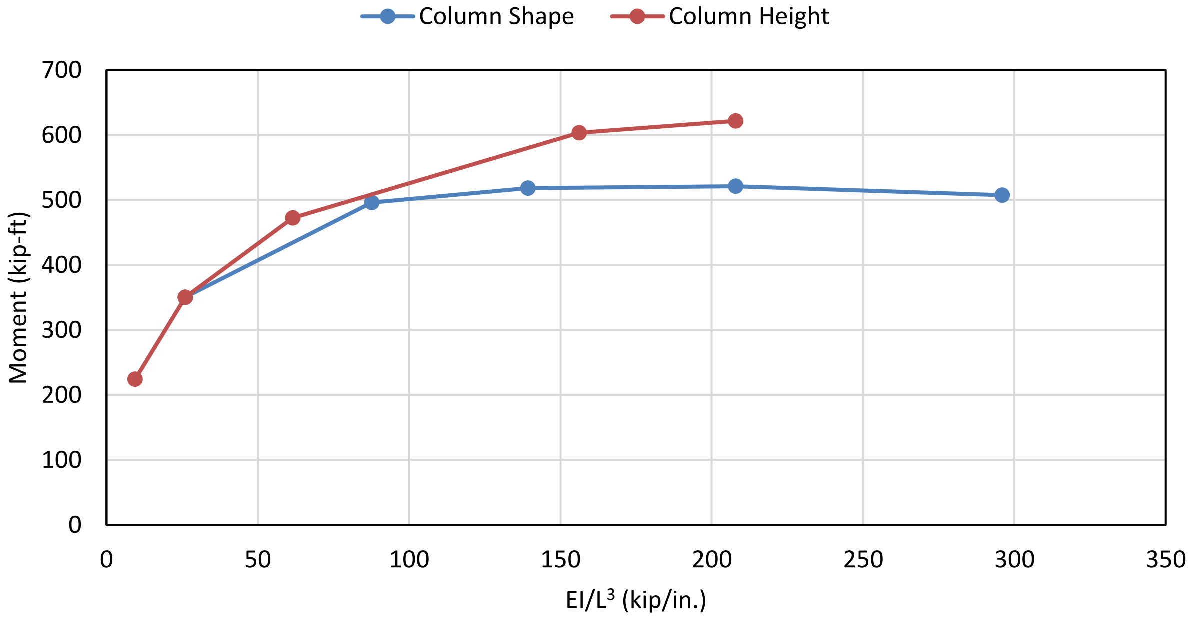

Figure 5.14. Maximum moment reactions of each uniform column stiffness case

In fact, the moment reaction was effectively constant for all of the column shape cases except for the base case, which had the lowest considered moment of inertia.

Increasing the rotational stiffness of the column bases as column stiffness is increased would likely produce different results.

Despite the cases covering a similar range of EI/L^3 values, the column height cases consistently experienced a higher demand than the cases altering the cross-sectional column shape. This difference was most prominent in the shear reaction results, in which the 10 ft column height case experienced 55% more shear demand than the 33.7 ft^4 moment of inertia case, despite both cases having identical EI/L^3 values. This difference was attributed to the ratio of flexural stiffness of the columns to that of the cap beam, which affects the locations of cracking.

In all the column height cases, the widest crack was a horizontal crack that formed at the beam-column interface at the exterior columns. This crack originated from the inside face of the exterior column. In the stiffest column height case considered, an additional small vertical crack formed in the cap, originating from the same location as the horizontal crack. The location of cracking differed among the column shape cases.

For the most flexible column shape cases considered, the widest crack formed nearly identical to that from the column height cases. However, for the stiffest column shape cases, the widest crack was a vertical crack that occurred in the cap beam and originated from the inside face of the exterior column. Additionally, no cracking occurred at the top of the column. In the stiffest column shape case considered, the cap beam experienced an additional crack near the outside face of the outermost interior column. This crack originated from the top of the cap beam. The location of this crack is interesting as additional gravity loads would likely widen the crack. The cracking strain distribution at the center of the frame pier for selected analyses is presented in Figure 5.15 and Figure 5.16 for various column height and column shape cases, respectively.

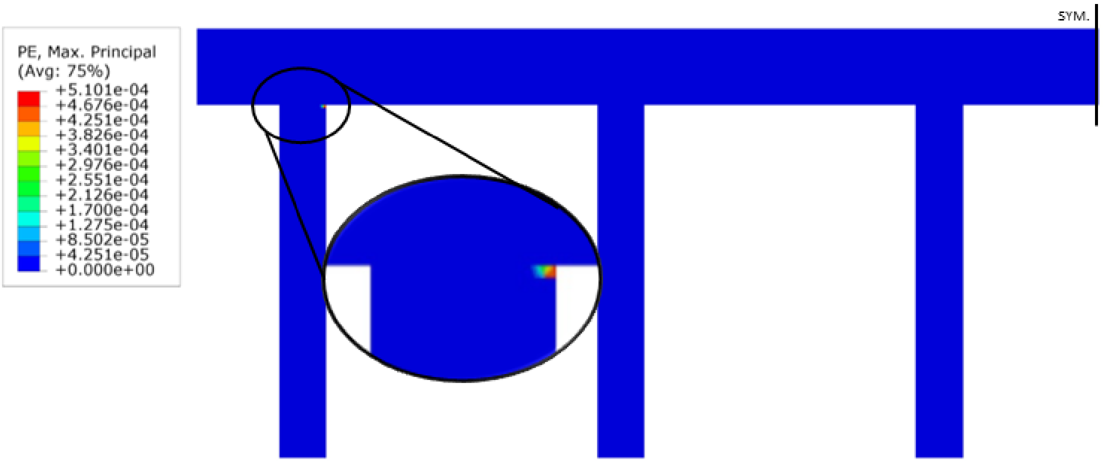

20 ft tall

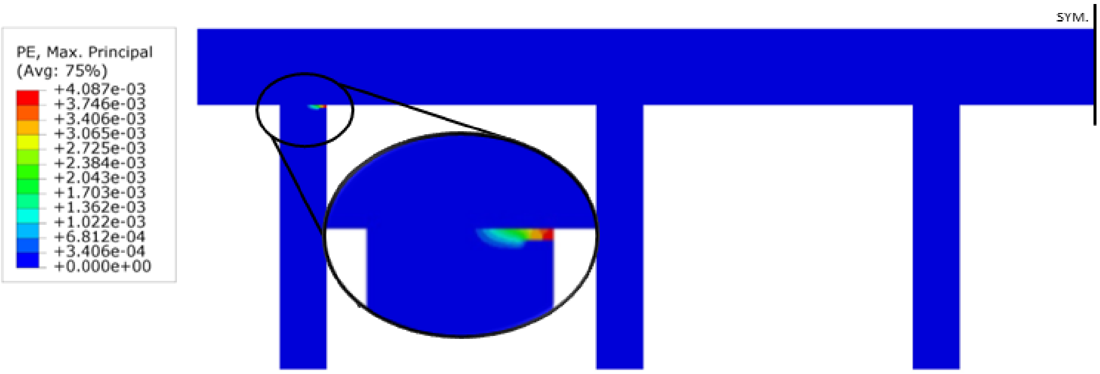

15 ft tall

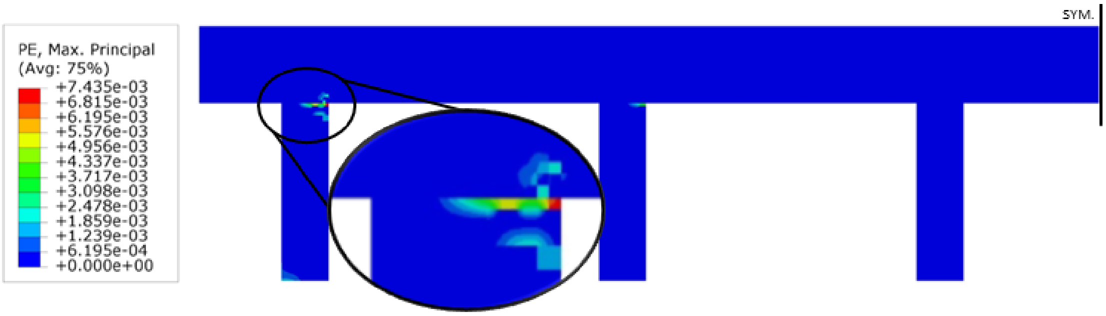

10 ft tall

Figure 5.15. Cracking strain for column height cases

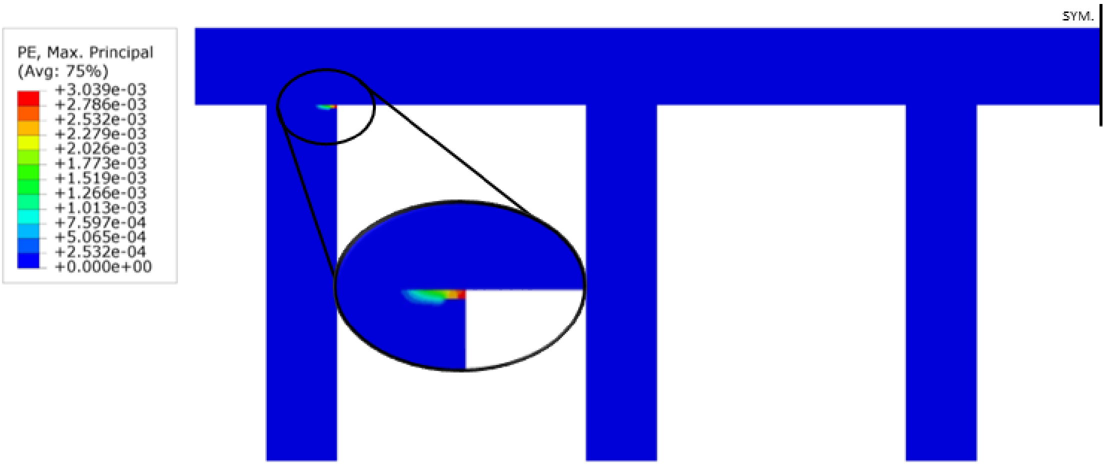

48 in. wide

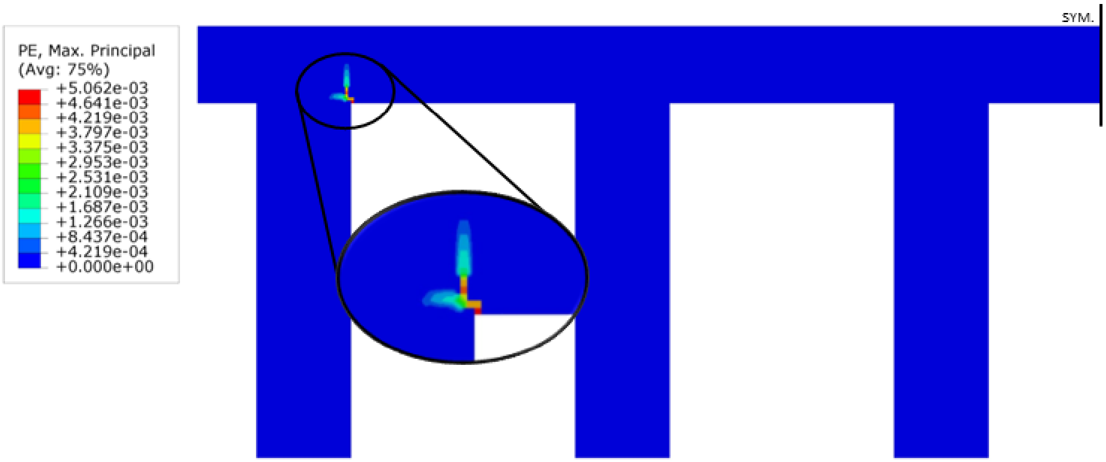

64 in. wide

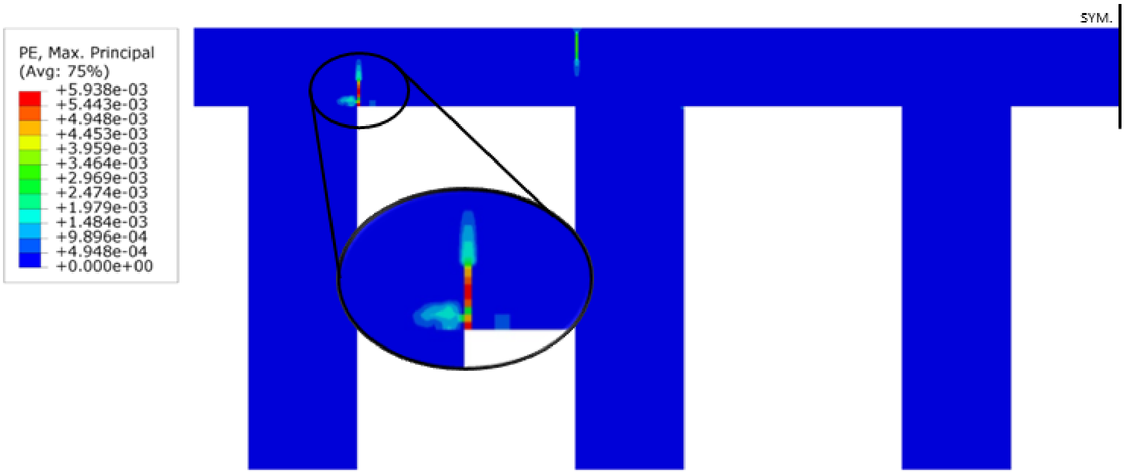

72 in. wide

Figure 5.16. Cracking strain for column shape cases

The vertical reactions at the column bases were observed. The minimum vertical reaction consistently occurred at the base of the exterior column. The minimum vertical reaction was important, since, when considered in combination with other loads such as wind, the vertical reaction may resist uplift. The minimum vertical reaction of the base case after all the dead load was placed on the frame pier resisted a downward force 325 kips. The column shape case with the stiffest columns decreased the vertical reaction the most of any case considered, resisting a downward vertical force of 250 kips, which constituted a 23% decrease in vertical force compared to the base case. The column height case with the stiffest columns was observed to decrease the vertical reaction by 16%, resisting a downward force of 273 kips.

Method 2 Results

To understand the effects of varying column stiffness between the exterior columns and interior columns, the results of Method 2 were compared to the uniform column shape cases considered in Method 1. Exterior columns considered in Method 2 were compared to exterior columns of the same stiffness in Method 1. Furthermore, the outermost interior columns in Method 2 were compared to the outermost interior columns of the same stiffness in Method 1.

The results of altering column stiffness in accordance with Method 2 show that a difference in stiffness between the exterior columns and interior columns had little effect on the behavior of frame piers subjected to temperature and shrinkage effects. The maximum shear and moment reactions at the exterior columns are presented in Figure 5.17 and Figure 5.18, respectively.

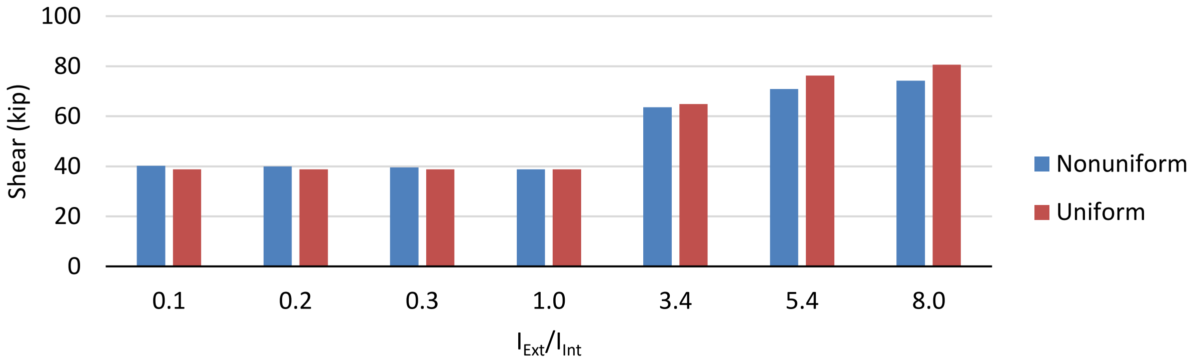

Figure 5.17. Exterior column base shear comparison between nonuniform and uniform column configurations

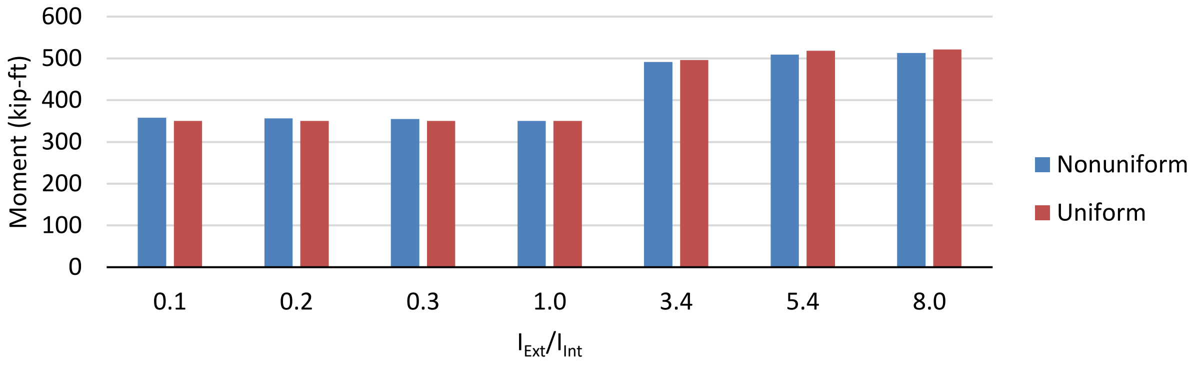

Figure 5.18. Exterior column base moment comparison between nonuniform and uniform column configurations

The maximum shear and moment reactions at the outermost interior column are presented in Figure 5.19 and Figure 5.20, respectively.

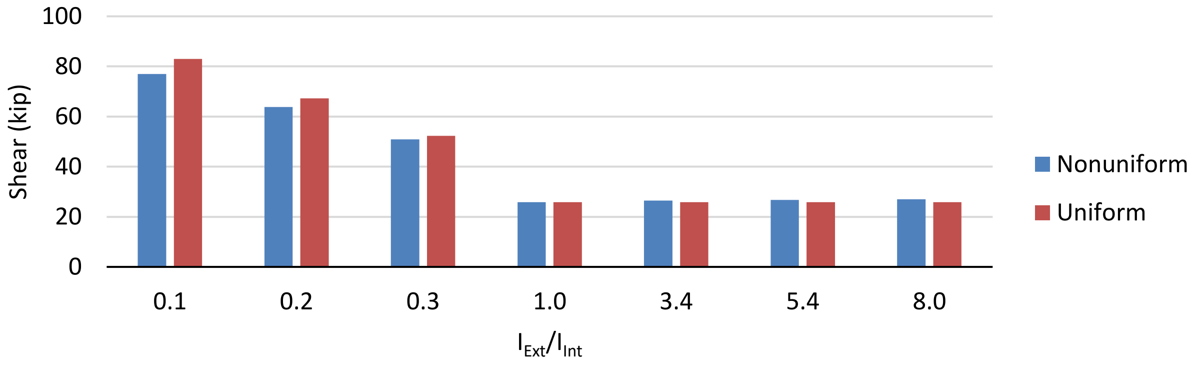

Figure 5.19. Outermost interior column base shear comparison between nonuniform and uniform column configurations

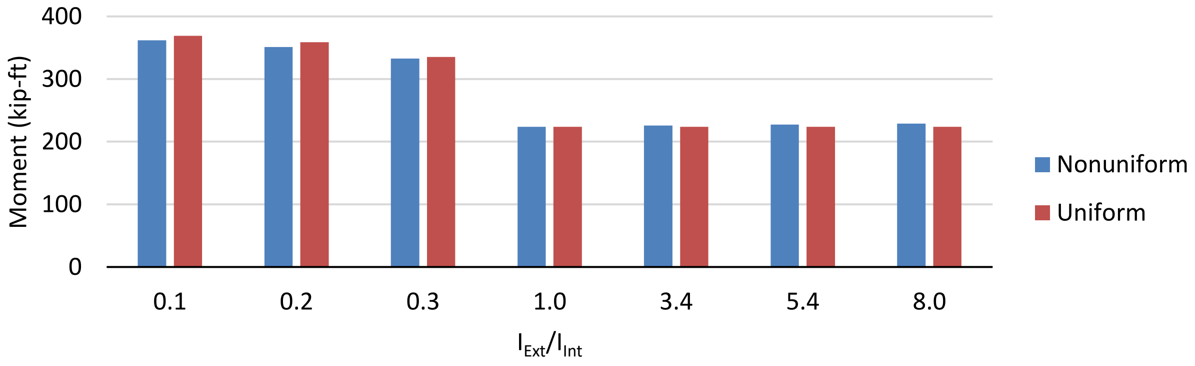

Figure 5.20. Outermost interior column base moment comparison between nonuniform and uniform column configurations

The most significant increase in shear and moment reactions occurred in the outermost interior column and increased by 4.6% and 2.3% over the Method 1 case, respectively. These increases in the interior column occurred in the case with the stiffest exterior columns considered (i.e., I_{Ext}/I_{Int} is equal to 8.0).

In this same case, the shear and moment reactions of the exterior column decreased by 7.9% and 1.6% over the Method 1 case, respectively. This decrease in the reactions of the exterior columns was significant since the exterior column experienced the maximum shear and moment demand of any column of the frame pier. In fact, the maximum shear and moment reactions of the frame pier were reduced in every case considered when compared to the Method 1 cases. Additionally, crack formations were identical to the cases of Method 1. Therefore, frame piers with either more or less stiff exterior columns were less susceptible to temperature and shrinkage effects than frame piers with uniform columns.

Method 3 Results

To understand the effects of linearly varied column stiffness along the length of a frame pier, the results of Method 3 were compared to the results of the uniform column height cases from Method 1. In particular, the 15 and 20 ft column height cases were used for comparison. The results of Method 3 in comparison to select results of Method 1 are presented in Table 5.4.

Table 5.4. Maximum FE results from the linearly varied column stiffness case compared to the uniform column stiffness case

Column Stiffness Case	Column Height (ft)	Shear (kip)	Moment (kip-ft)	Lateral Disp. (in.)	Cracking Strain (με)	Rebar Stress (ksi)
Linearly Varied	15.0	60.7	422.8	0.231	2,841	14.0
Uniform	15.0	68.0	472.4	0.266	4,087	21.5
Linearly Varied	20.0	42.6	390.4	0.307	2,137	13.4
Uniform	20.0	38.8	350.5	0.272	510	15.6

As expected, the maximum demand of the linearly varied column stiffness frame pier occurred in the shortest (15 ft tall) exterior column. Compared to the uniform 15 ft tall column case, the shear and moment demand of the 15 ft column of the linearly varied case was 10.7% and 10.5% less, respectively. Shear and moment demand of the 20 ft column increased by 9.8% and 11.4%, respectively, compared to the uniform 20 ft column case. However, the most significant difference between these two cases was the amount of cracking strain the frame pier experienced at the 15 ft column. Cracking occurred at both exterior columns at the column tops. Both cracks originated from the inside face of the columns, as presented in Figure 5.21.

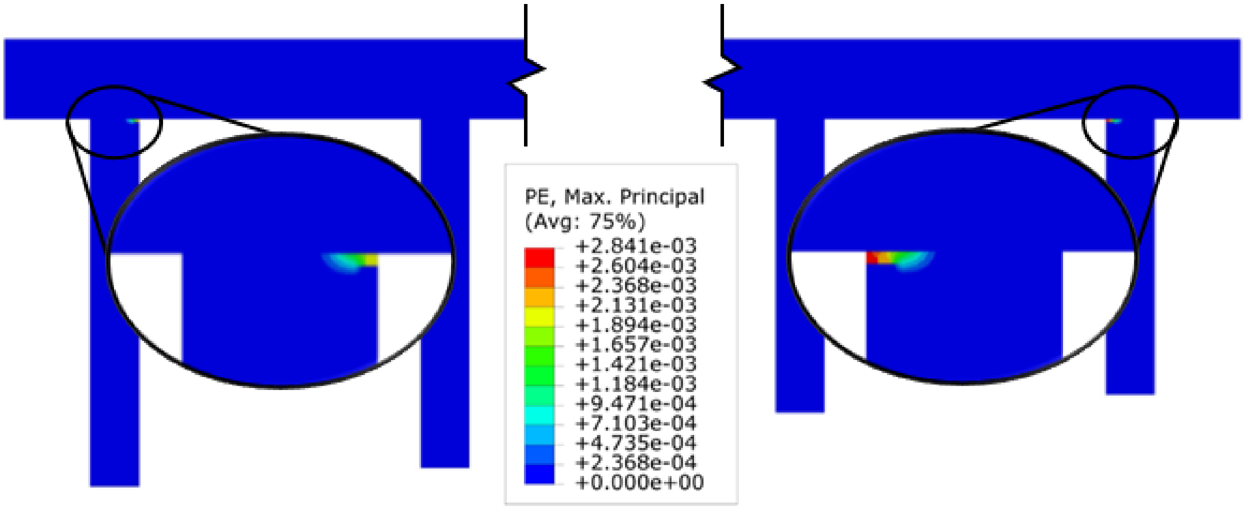

Figure 5.21. Cracking strain for the linearly varied column stiffness case

The location of cracking was identical to that from the uniform column height cases. Yet, for the 15 ft exterior column, the cracking strain was 30.5% less than that of the uniform 15 ft columns case. For the 20 ft exterior column, the cracking strain was 319% greater than that of the uniform 20 ft column case. These differences appear significant; however, they can be attributed to the development of cracking strain occurring suddenly at some point during the analysis. For example, the uniform 15 ft tall column case did not experience significant cracking strain until day 115 after casting.

The vertical reactions at the column bases were observed. The minimum vertical reaction occurred at the base of the 15 ft tall exterior column. The minimum vertical reaction was important since, when considered in combination with other loads such as wind, the vertical reaction may need to resist uplift. After all of the dead load was placed on the frame pier, the minimum vertical reaction of the case with uniform 15 ft tall columns was a downward force of 303 kips. The 15 ft tall exterior column of the linearly varied column stiffness case resisted a downward vertical force of 312 kips, which constituted a 3% increase in downward vertical force compared to the base case. Similarly, the 20 ft tall exterior column experienced a minor alteration in its vertical reaction compared to its corresponding uniform column case, with a 1.5% increase in downward force.

Effects of Frame Length

Purpose

The length of a frame is a well-known factor that influences the effects of volumetric changes in frames. Some bridge design manuals rely heavily on frame length as a criterion for designing a frame pier for temperature and shrinkage effects. For example, the bridge design manuals created by Illinois and Nebraska consider only the length of a frame pier when determining whether to place a joint in the cap beam or even include temperature and shrinkage effects in design, respectively.

The effect has yet to be investigated specifically in frame piers, as the literature focuses on building frames. The purpose of this parametric study was to isolate and observe the effect of frame length on the behavior of frame piers subjected to temperature and shrinkage effects.

The results from this parametric study will be compared with those of the other parametric studies performed to help identify the frame pier geometry most susceptible to temperature and shrinkage effects.

Finite Element Analysis

The base case for the frame length investigation was identical to that of the column stiffness investigation: a frame pier with 20 ft tall columns and a length of 90 ft from the centerline of exterior column to the centerline of exterior column. This frame pier geometry was based on an existing frame pier in Iowa that uses a common column size, 3 ft diameter columns (modeled as square columns with a cross-section of 32 in. by 32 in. to increase model stability and maintain similar stiffness). The frame pier supported prestressed concrete girders spaced 7.5 ft on center and an average bridge span of about 79 ft. Only the dead load of the structure and forces due to temperature and shrinkage effects are considered in the analysis.

For every frame length case considered, only the frame length (measured from centerline of exterior column to centerline of exterior column) was altered from the base case and all other components of the frame pier remained constant: including material properties, rebar configuration, rotational stiffness at the column bases, cap beam dimensions, column spacing, shrinkage strain development, dead load applied to the cap beam, and temperature history.

Six different frame lengths were considered with frame lengths of 18, 54, 90, 162, and 198 ft. The considered frame length cases are presented in Figure 5.22.

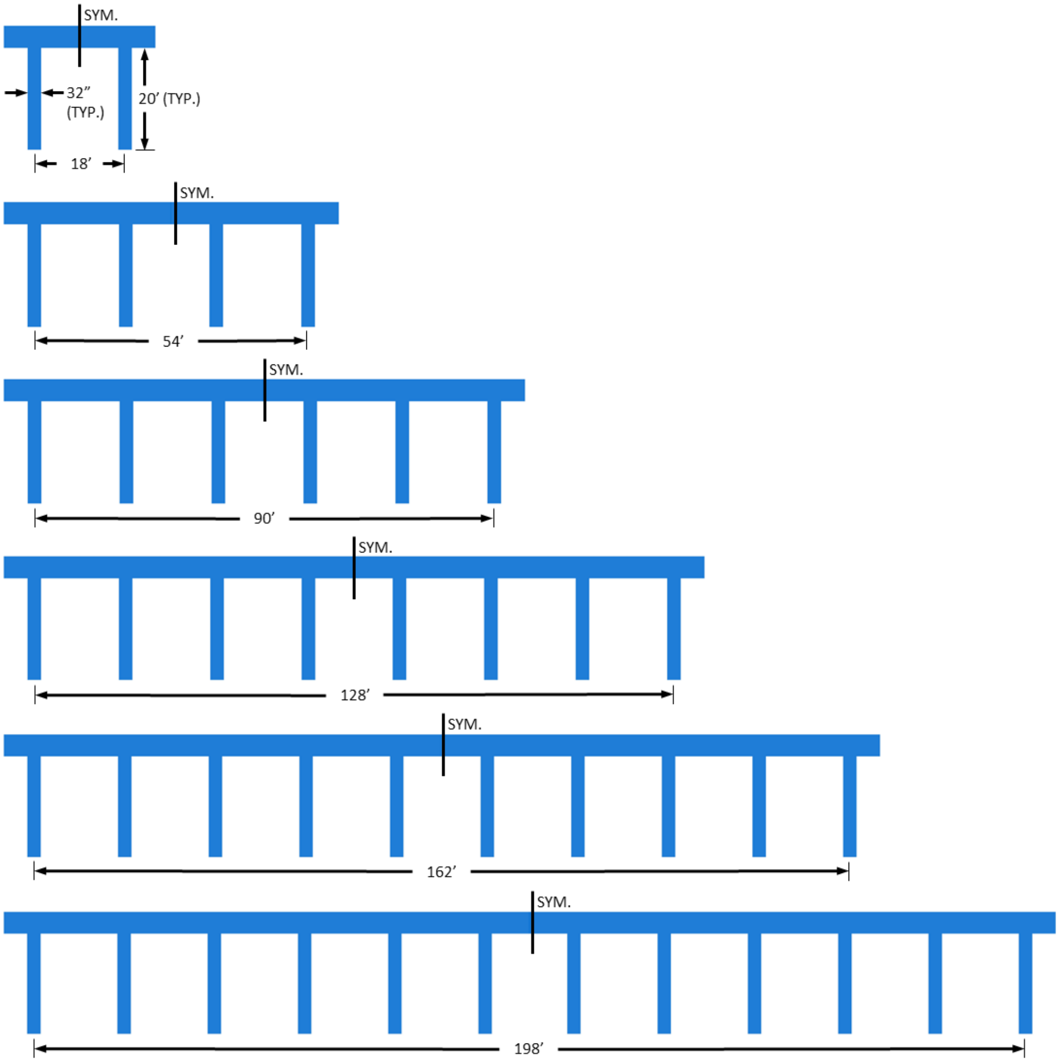

Figure 5.22. Frame length cases considered

Several different measures of performance and demand of the structure were extracted from the results of each case. The maximum shear at a column base, maximum moment at a column base, minimum vertical load at a column base, maximum lateral displacement of the top of an exterior column, maximum cracking strain of the structure, and maximum rebar stress are all extracted. Beam spacing was kept as consistent as possible between the various cases considered. However, if the beam spacing fluctuated by any amount, the beam loads were recalculated for the new beam spacing.

Results

In every frame length case considered, the exterior columns experienced the highest demand. In comparison to the base case, the shear and moment reactions at the column base increased by 64% and 77%, respectively, when the frame length was increased to 198 ft. The shear and moment reactions at the column base dropped by 78% and 79%, respectively, when the frame length was decreased to 18 ft. Like the column stiffness cases, these increases in shear and moment reactions were not linearly dependent on frame length and instead began to taper as the frame length increased. This was again attributed to creep and cracking of the concrete relieving stress in the structure under higher loads. A summary of key results extracted from the frame length cases is presented in Table 5.5.

Table 5.5. Maximum FE results from the frame length cases

Frame Length (ft)	EI/L^3 (kip/in.)	Shear (kip)	Moment (kip-ft)	Lateral Disp. (in.)	Cracking Strain (με)	Rebar Stress (ksi)
18.0	26.0	8.5	74.3	0.056	0	7.5
54.0	26.0	24.0	214.7	0.165	0	9.6
90.0	26.0	38.8	350.5	0.272	510	15.6
126.0	26.0	49.4	463.5	0.377	3,705	19.2
162.0	26.0	57.6	552.7	0.480	5,211	27.0
198.0	26.0	63.6	621.2	0.580	5,406	32.2

Plots of the maximum shear and moment reactions are presented in Figure 5.23 and Figure 5.24, respectively.

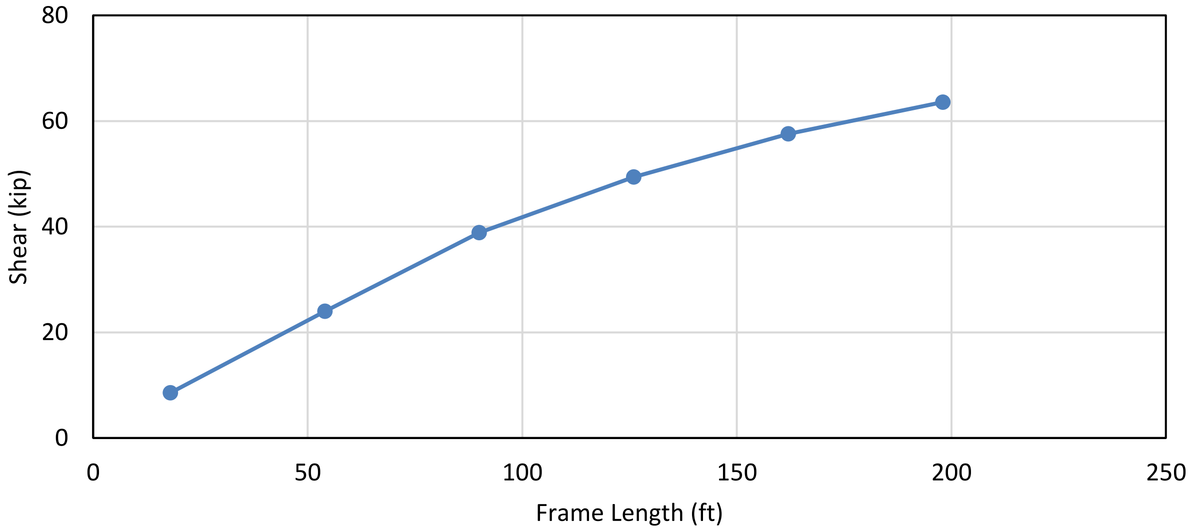

Figure 5.23. Maximum shear reactions of each frame length case

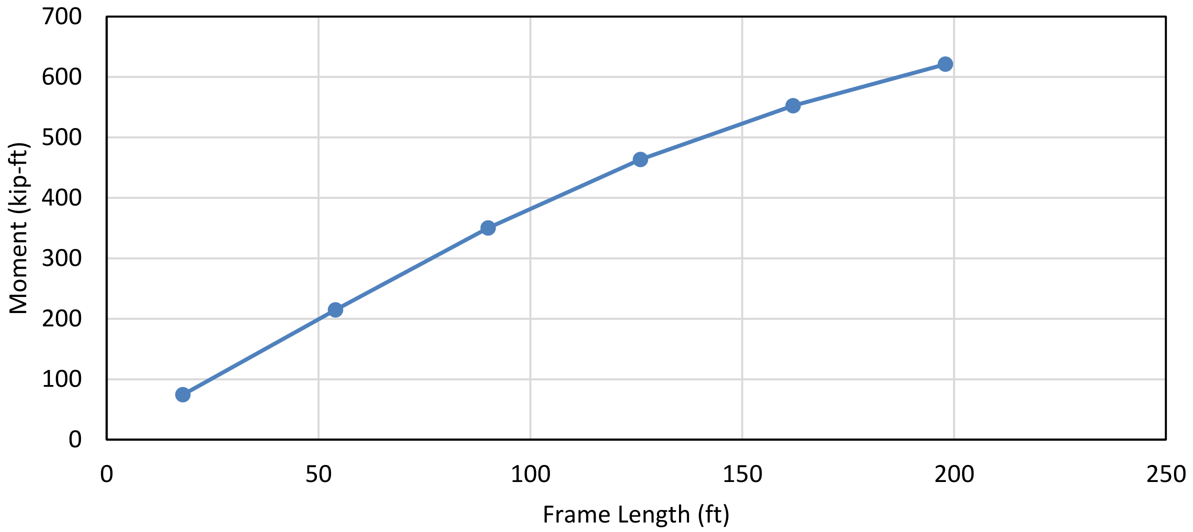

Figure 5.24. Maximum moment reactions of each frame length case

The formation of cracks in the frame length cases was nearly identical to that of the column height cases considered in the uniform column stiffness investigation. The two shortest frame lengths considered (18 ft and 54 ft) did not undergo any observable cracking in the FE analysis. The widest crack in the other frame length cases occurred at the interface between the cap beam and exterior column and originated from the inner face of the column. Cracking strain distribution of selected cases is presented in Figure 5.25.

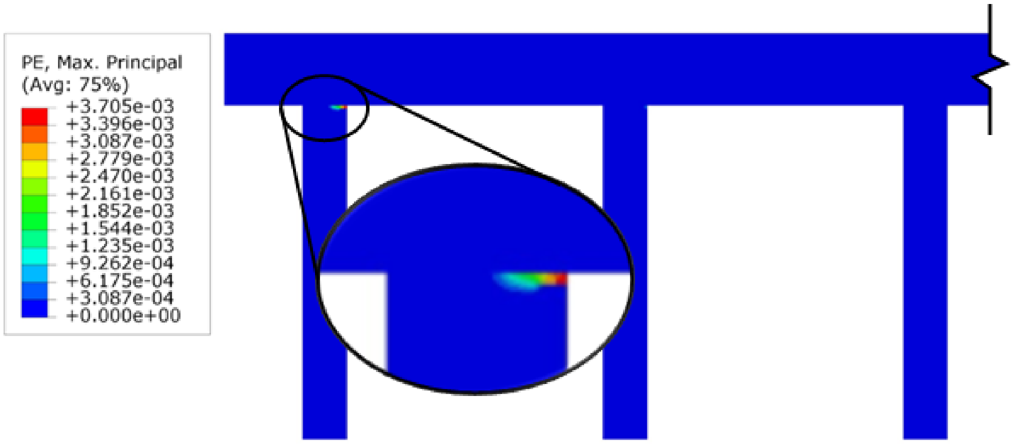

126 ft long

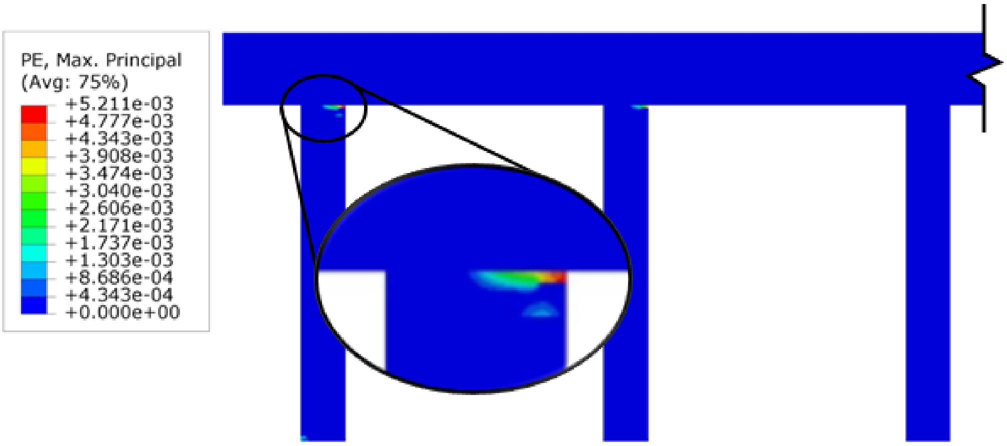

162 ft long

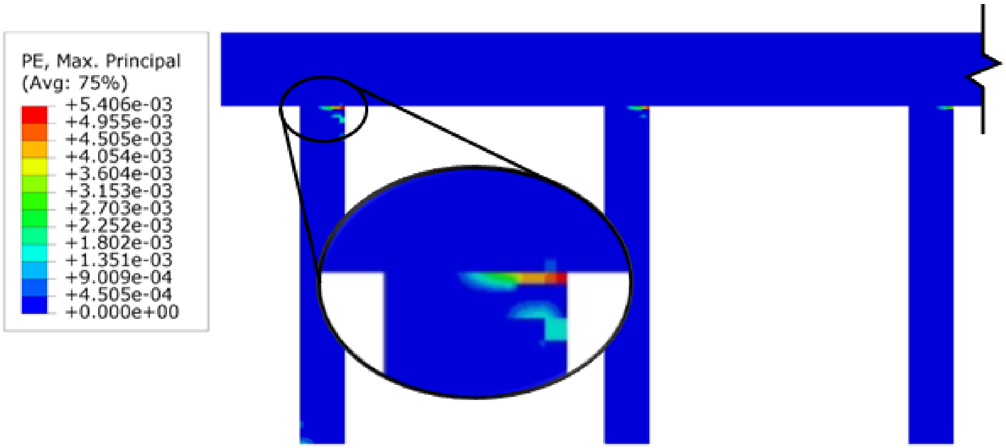

198 ft long

Figure 5.25. Cracking strain for frame length cases

The vertical reactions at the column bases were observed. The minimum vertical reaction at the column base was important because, when considered in combination with other loads such as wind, the column foundation may need to resist uplift. The minimum vertical reaction was determined to consistently occur at the base of the exterior column. The minimum vertical reaction of the base case was a downward force of 325 kips at a point in time after all the self-weight of the bridge was loaded onto the frame pier. The longest frame length case was observed to decrease the vertical reaction most significantly of out of all the frame length case considered, resisting a downward vertical force of 296 kips, which constituted a 9% decrease in vertical force compared to the base case.

Effects of Bay Length

Purpose

While frame length and column stiffness were the primary focus of this study, the effect of bay length was also known to influence forces in frames subjected to volumetric changes. In a study focused on building frames, roughly doubling the bay length led to a 1.6% increase in moments and axial forces in the members (Ahmed 2011). Generally, bay length has minimal effect on the overall structural performance of frames. However, this parameter has not been investigated for frame piers, which are exposed to different environmental conditions and loading than building frames. Therefore, the effect of bay length on the performance of frame piers subject to shrinkage and temperature effects was examined.

The results from this parametric study will be compared with those of the other parametric studies performed to identify the most susceptible frame pier geometry to temperature and shrinkage effects.

Finite Element Analysis

The base case for the bay length investigation was identical to that of the column stiffness investigation: a frame pier with 20 ft tall columns and a length of 90 ft from the centerline of the exterior column to the centerline of the exterior column. This frame pier geometry was based on an existing frame pier in Iowa that used a common column size, i.e., 3 ft diameter columns (modeled as square columns with a cross-section of 32×32 in. to increase model stability and maintain similar stiffness). The frame pier supported prestressed concrete girders spaced 7.5 ft on center and an average bridge span of about 79 ft. Only the dead load of the structure and forces due temperature and shrinkage effects were considered in the analysis.

Only the bay length (measured from centerline of column to centerline of column) was altered from the base case, and all other components of the frame pier remained constant, including material properties, rebar configuration, rotational stiffness at the column bases, cap beam dimensions, overall frame length, shrinkage strain development, dead load applied to the cap beam, and temperature history. The bay length was altered by reducing the column spacing and adding additional columns. The bay length was reduced from 18 ft of the base case to 10 ft, which constituted a 44% reduction in bay length. The considered bay length case is presented in Figure 5.26.

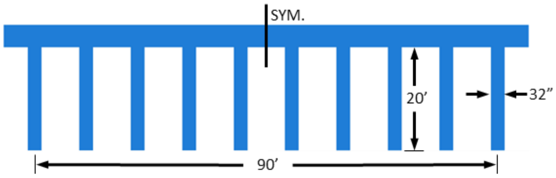

Figure 5.26. Bay length case considered

Several different measurements of performance and demand of the structure were extracted from the results of each case. The maximum shear at a column base, maximum moment at a column base, minimum vertical load at a column base, maximum lateral displacement of the top of an exterior column, maximum cracking strain of the structure, and maximum rebar stress were all extracted.

Results

Reducing the bay length from 18 to 10 ft was found to have a minor influence on the behavior of frame piers subjected to temperature and shrinkage effects. The frame pier with a shorter bay length was slightly more susceptible to temperature and shrinkage effects, as summarized in Table 5.6.

Table 5.6. Maximum FE results from the bay length case compared to the base case

Bay Length (ft)	EI/L^3 (kip/in.)	Shear (kip)	Moment (kip-ft)	Lateral Disp. (in.)	Cracking Strain (με)	Rebar Stress (ksi)
10.0	26.0	40.4	361.0	0.276	3,055	15.5
18.0	26.0	38.8	350.5	0.272	510	15.6

The shear and moment reactions were highest at the base of the exterior column at 3.9% and 3.0% greater, respectively, in the frame pier with 10 ft bays than those of the frame pier with 18 ft bays. Of significance, the plastic tensile strain was five times higher in the 10 ft bay model compared to the 18 ft model. This increase in cracking was attributed to the additional restraint at the top of the columns since the span of the cap beam was nearly cut in half and thus more able to resist rotation at the column tops. The distribution of cracking strain of the 10 ft bay length model is presented in Figure 5.27.

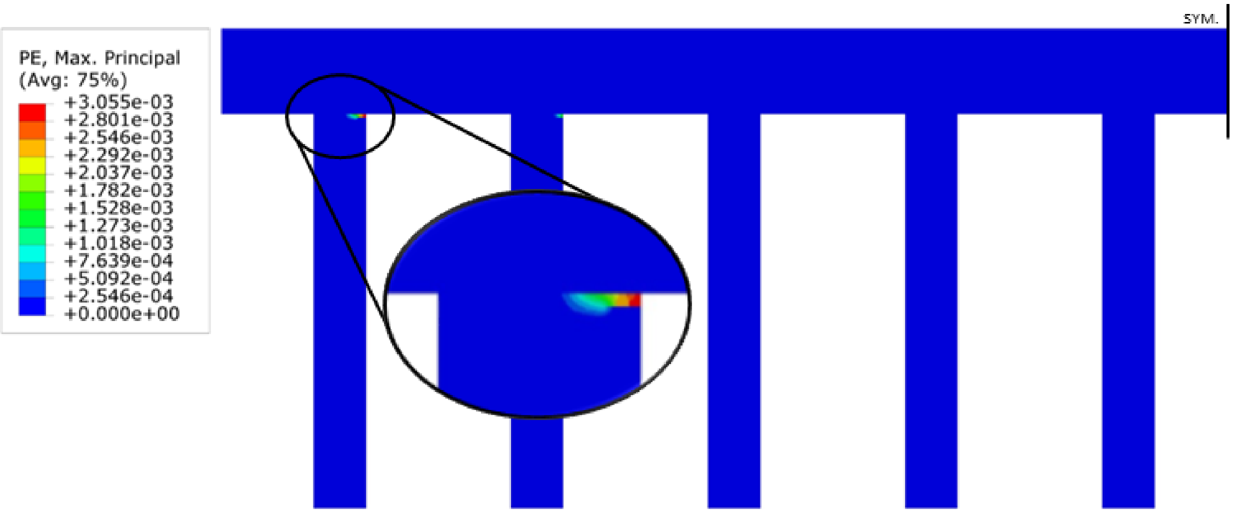

Figure 5.27. Cracking strain of the 10 ft bay length case

Another observation was that the downward vertical reaction at the exterior columns increased by 14.3%, indicating that the shorter bay length frame pier was less susceptible to experiencing uplift.

Discussion

Frame length was determined to significantly affect the demand of a frame pier under temperature and shrinkage effects. For example, increasing a 90 ft long frame pier by 108 ft (to a total length of 198 ft) increased the base shear at the exterior columns by 64%. However, reducing the column height of the same 90 ft long frame pier by just 5 ft (to a height of 15 ft) increased the base shear at the exterior columns by 75%. Furthermore, frame piers with 15 ft tall columns are more common than frame piers with a frame length of 198 ft. This shows that column stiffness can have a greater affect than frame length on the demand of a frame pier under these volumetric effects.

The ratio of flexural stiffness of the columns to that of the cap beam affects the location of cracking in frame piers. When the stiffness of the columns was greater than that of the cap beam (i.e., column stiffness was greater than about two times the cap beam stiffness), a vertical crack originating from the top of the cap beam formed above the outermost interior column. Because this crack is located at a point of negative moment in the cap beam, although not the widest, it could cause problems due to gravity loads increasing the width of the crack. However, vertical cracks in the cap beam were observed to reduce the demand on the columns.

Many of the cases analyzed with the calibrated FE model were compiled to observe the effectiveness of available metrics used to estimate the susceptibility of a frame to temperature or shrinkage effects. These metrics were used in other studies and bridge design guides. The maximum shear reactions from the numerical investigations were plotted against various metrics which were calculated for each frame pier geometry considered.

The first metric investigated was simply the length of the frame pier (measured from the centerline of the exterior column to the centerline of the exterior column). The results of this metric plotted against the numerical shear reactions is presented in Figure 5.28.

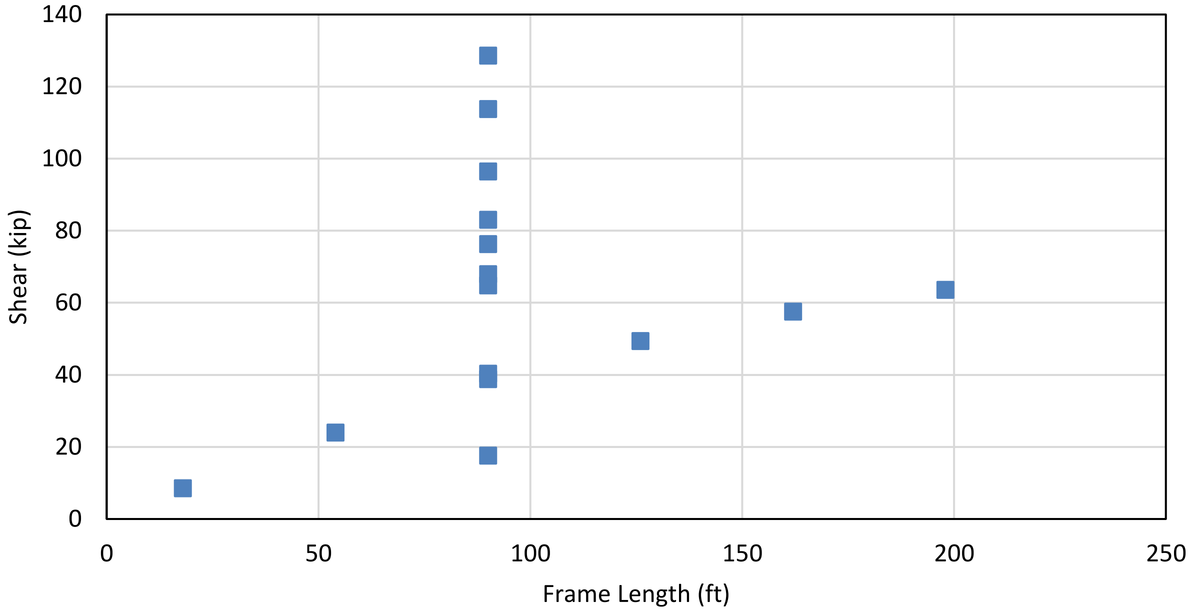

Figure 5.28. Maximum shear reaction plotted against frame length

As expected, relying only on frame length as a metric to determine susceptibility of a frame pier was not accurate enough. This is primarily because the column stiffness, which is determined to greatly affect the demand on the frame pier, was not accounted for in this metric.

Another metric considered was the ratio of the frame length to column height (i.e., L/H). This metric somewhat accounts for column stiffness, but neglects the cross-sectional shape of the column, which can significantly influence column stiffness. The results of the L/H metric plotted against the numerical shear reactions is presented in Figure 5.29.

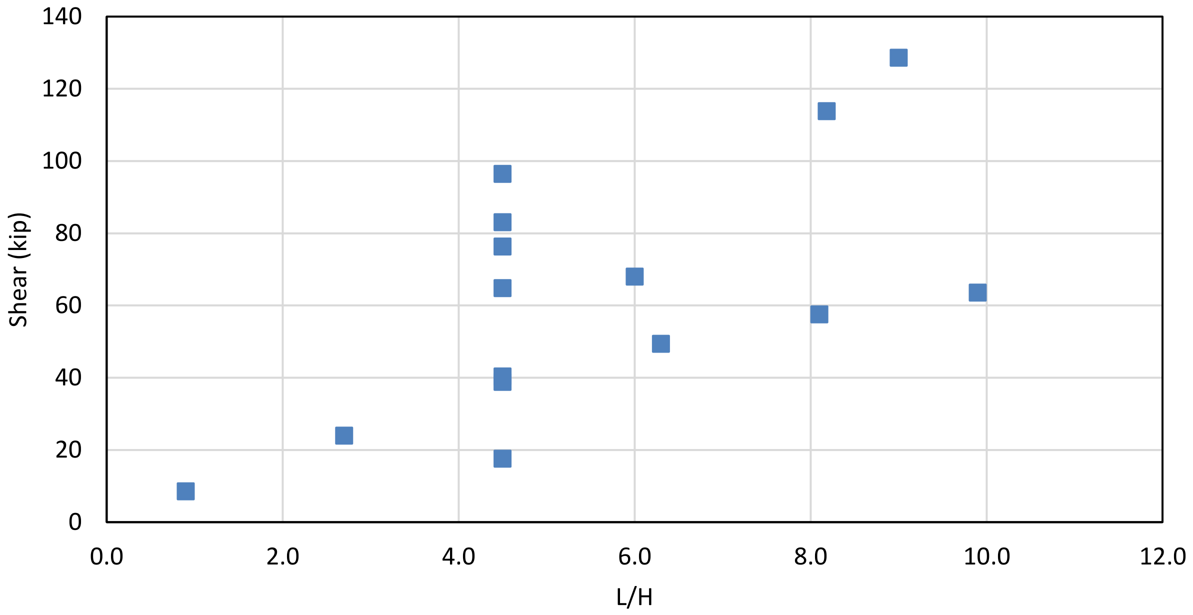

Figure 5.29. Maximum shear reaction plotted against the ratio of frame length to column height

This metric was a slight improvement over the frame length metric, as this metric had a more visible trend. However, this metric was still not accurate enough, as a significant component of column stiffness was unaccounted for.

Another metric considered was the EI/H^3, or $K_{approx.}$, portion of lateral column stiffness multiplied by the frame length (i.e., $L \times K_{approx.}$). This metric is plotted against the numerical shear reactions in Figure 5.30.

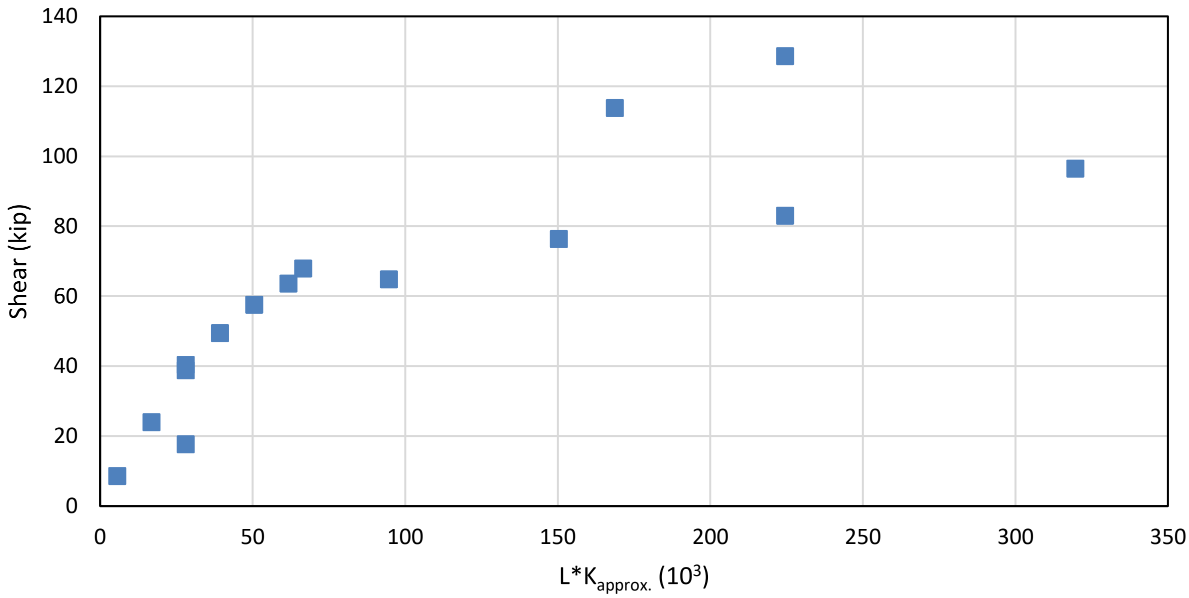

Figure 5.30. Maximum shear reaction plotted against the product of frame length and approximate lateral column stiffness

This metric was reasonably accurate at predicting susceptibility, apart from overestimating the shear demand of the stiff column shape cases. This can be attributed to neglecting the restraint of the cap beam at the top of the column. As the column stiffness increased, the effect of restraint provided by the cap beam diminished. Since column flexural stiffness was calculated differently than column lateral stiffness, the $L \times K_{approx.}$ metric failed to account for the effect of this restraint. Additionally, this metric did not account for the rotational stiffness at the column base.

The final metric investigated used a more robust value for the column's lateral stiffness. In this metric, lateral column stiffness was calculated as follows (Schultz 1992):

$$K_{fixed} = \left(\frac{12EI}{H^3}\right)\left(\frac{k_c+\sum k_{ga}}{4k_c+\sum k_{ga}}\right) \tag{5.2}$$

$$k_c = \frac{E_{column}I_{column}}{H} \tag{5.3}$$

$$k_g = \frac{E_{cap}I_{cap}}{L_{bay}} \tag{5.4}$$

where K_{fixed} is the lateral stiffness of the column assuming a fixed base, E is the modulus of elasticity of the column, I is the moment inertia of the column, H is the height of the column, k_c is the flexural stiffness of the column, and $\sum k_{ga}$ is the sum of the flexural stiffnesses of the beams connecting to the top of the column. The final metric considered was the product of the length of the frame and K_{fixed}. This metric is plotted against the numerical shear reactions in Figure 5.31.

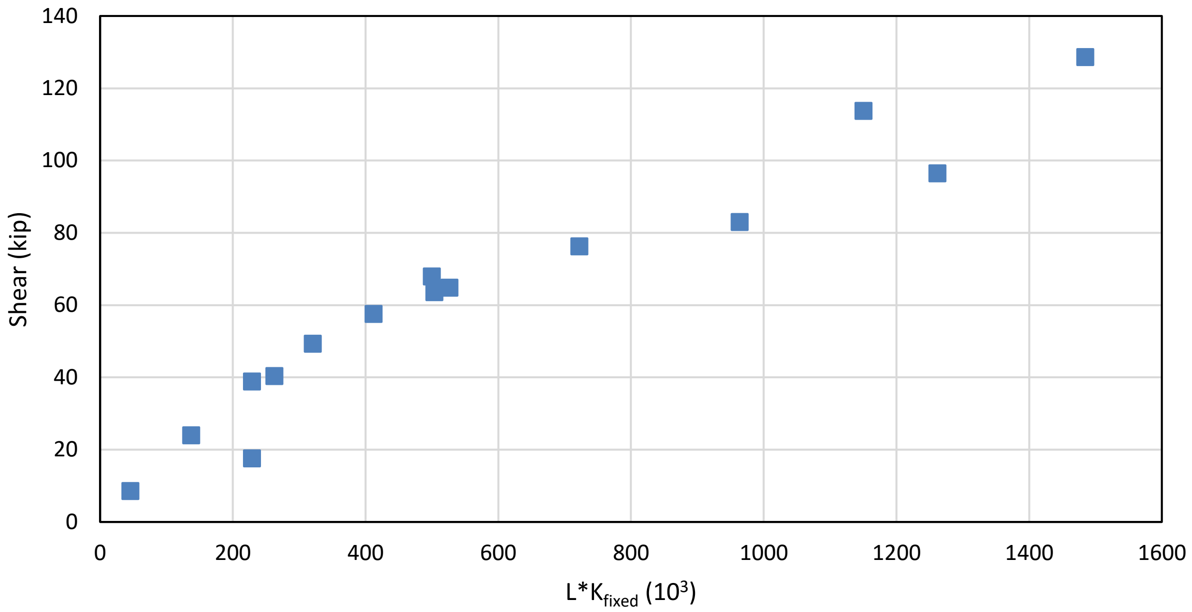

Figure 5.31. Maximum shear reaction plotted against the product of frame length and lateral column stiffness assuming a fixed base

Despite this metric treating the column bases as fixed, shear susceptibility was most accurately predicted in this metric compared to all other metrics investigated.

The results of investigating various metrics to predict the susceptibility of a frame pier to temperature and shrinkage effects show which factors of a frame pier most significantly affect its susceptibility to temperature and shrinkage effects. Column stiffness, frame length, and end restraints of the column must be considered to accurately predict a frame pier's susceptibility to temperature and shrinkage effects. Any predictive metric missing one of these components can significantly miscalculate the susceptibility of frame piers subjected to volumetric changes.

CHAPTER 6. COMPARISON OF MODELS AND DESIGN CONSIDERATIONS

This chapter compares the results of a series of material and geometric nonlinear brick element FE models created using Abaqus CAE to the result of a series of corresponding linear elastic beam element FE models created using LARSA. Both sets of models were constructed to represent the same geometry, member sizes, gross section properties and effective boundary conditions identified in the parametric study. Both models were loaded with equivalent levels of dead load to represent the superstructure load applied to the bent and to capture the gravity portion of second order effects resulting from the displacements caused by in-plane thermal and shrinkage loading. However, the magnitude of the response influenced by the vertical gravity loads was not further investigated in either type of model nor explicitly compared between the models.

Nonlinear Model Parameters

The nonlinear FE model used shrinkage and thermal forces derived from field data records. The thermal range recorded in the field varied from a low temperature of 14.3°F to a high temperature of 85.7°F, which was a range of 71.4°F. Based on the data collected and reported in previous chapters, the mean material temperature was between 65°F and 75°F. With a midpoint of 70°F, this resulted in a temperature rise of approximately 15°F and a temperature fall of approximately 55°F.

For concrete structures, Iowa DOT Bridge Design Manual (BDM), Section 6.6.2.12.2, specifies a design thermal range of 100°F centered on a mean material temperature of 50°F at the time of construction, i.e., a material temperature drop or rise of 50°F may occur over the life of the structure. Therefore, the nonlinear FE model captured approximately 110% of the 50°F drop in temperature specified as part of the design temperature range prescribed by the Iowa DOT BDM.

The concrete strength in the nonlinear FE model was based on field data with a measured 28-day compressive strength of just over 5 ksi. Correspondingly, the material properties of the linear elastic model were based on concrete with a 28-day compression strength of 5.0 ksi. The effects of shrinkage were incorporated into the nonlinear FE model using field data and construction staging as previously described. The linear elastic model considered shrinkage in accordance with the Iowa DOT BDM and used a shrinkage coefficient of 0.0002.

Results and Comparison to the Linear FE Model

A comparison and discussion of results between the two sets of models for five of the parametric cases follows. The parametric cases were typically based on a pier frame with 18 ft column spacing, 32 in. square columns and 90 ft between exterior columns as described in previous chapters. For the Iowa DOT, standard bridges typically have similar column spacing; however, the overall length of a pier is based on bridge width and skew angle with a frame length of 90 ft on the larger end of the range of typical pier lengths.

Thermal strain associated with material temperature change is a function of the thermal coefficient of the material. The thermal coefficient of concrete is 0.000006 in./in./°F, and this coefficient was applied in both the nonlinear and linear elastic models. The shrinkage strain applied in the nonlinear models was based on material properties and data gathered from field monitoring while the shrinkage strain applied to the linear elastic models was 0.0002 in./in. as specified in the Iowa BDM, Section 6.6.2.14.

Strains associated with a rise in temperature act in the opposite direction of shrinkage strains while strains associated with a drop in temperature are additive to shrinkage strains. As discussed in previous chapters, the controlling strain case measured in the field was associated with summer construction (i.e., the concrete was cast during the summer, at a time of higher temperatures) coupled with the drop in temperature that later occurred in the winter.

For the cases discussed later representing the combined effects of thermal contraction and concrete shrinkage, the lateral displacements occurring at the tops of the exterior columns predicted by the linear elastic models were nearly identical to those predicted by the nonlinear models, indicating that, although the field-observed temperature drop of 55°F was 110% of the Iowa DOT BDM-specified design temperature drop of 50°F, the field-observed effects of concrete shrinkage appear to have been slightly smaller than the Iowa DOT BDM-specified shrinkage by a similar magnitude.

This study used soil springs to represent the rotational flexibility of the foundation at the base of the columns, as described as an optional method to relieve internal forces in the Iowa BDM, Section 6.6.2.12.3. This effectively provided some relief of the in-plane thermal and shrinkage forces by representing additional flexibility in the overall structural system. This approach was determined to be adequate in representing the rotational stiffness at the base of the columns through the validation of the FE model with the field data. However, it does take BDM 6.6.2.12.3 out of context. This article of the BDM is meant to address out-of-plane TU forces, not in-plane forces.

An overarching design consideration for the various models was whether the column section properties used in the analyses represent the cracked or gross moment of inertia. In the ninth edition of the AASHTO Load and Resistance Factor Design (LRFD) Bridge Design Specifications (AASHTO BDS), Article 3.4.1 states, “When a refined analysis is completed for concrete substructures in the strength limit state, a value of 1.0 for γ_{TU} shall be used in conjunction with a partially cracked moment of inertia determined by analysis. For concrete substructures in the strength limit state, the value of 0.50 for γ_{PS}, γ_{CR}, and γ_{SH} may similarly be used when calculating force effects in nonsegmental structures, but shall be taken in conjunction with the gross moment of inertia in the columns or piers.” The nonlinear Abaqus models incorporated the ability to model cracked sections and material nonlinearity; therefore, displacement-driven loading effects such as thermal expansion/contraction and concrete shrinkage should be factored using γ_{TU} and γ_{SH} load factors of 1.0. Meanwhile, the linear elastic LARSA models featured column section properties based on the gross moment of inertia, with no consideration of concrete cracking or other nonlinear material behavior and would therefore be used in conjunction with γ_{TU} and γ_{SH} load factors of 0.5.

The tables that follow show the results from the parametric studies performed with both the linear elastic and nonlinear models. The results are shown for the top of the exterior column at the interface with the cap. When evaluating the results, a shear or moment ratio between the nonlinear model and the linear elastic model of 0.5 equates to perfect correlation with the AASHTO load factor discussion above, and a ratio of 1.0 signifies the same for displacement. A larger ratio represents areas where the AASHTO load factors may be unconservative while a smaller ratio represents the opposite.

The models used a frame length of 90 ft for all the cases, unless indicated below. Column heights are provided in each table to indicate which parametric run the results were taken from. To correlate the results with real world applications, column heights were typically 15 ft or greater for roadway crossings and taller for railroad crossings, but in some cases the column heights for stream crossing bridges were shorter. The column dimensions used in these models were 32 in. by 32 in. Iowa DOT typically uses round columns, but the moment of inertia, cross-sectional area, and shear area for a 32 in. square column (4.214 ft^4, 7.111 ft^2, and 5.926 ft^2, respectively) approximately correspond to the moment of inertia, cross sectional area, and shear area of a 38 in. diameter round column (4.936 ft^4, 7.876 ft^2, and 7.088 ft^2, respectively), which is in the range of typical column sizes used in Iowa DOT bridges per the Iowa DOT BDM, Section 6.6.4.1.2.

Table 6.1 contains the results and comparison ratios of the parametric study based on varying the height of the columns in the linear elastic and nonlinear models.

Table 6.1. Comparison of results from the column height cases

		NL Abaqus Model Results			**LE LARSA Model Results**			**Ratio NL/LE**		
EI/L^3 (kip/in.)	**Column Height (ft)**	**Shear (kip)**	**Moment (kip-ft)**	**Lateral Disp. (in.)**	**Shear (kip)**	**Moment (kip-ft)**	**Lateral Disp. (in.)**	**Shear**	**Moment**	**Lateral Disp.**
207.9	10.0	129	622	0.253	241	1589	0.245	0.53	0.39	1.03
156.2	11.0	114	604	0.256	198	1409	0.249	0.57	0.43	1.03
61.6	15.0	68	472	0.266	98	905	0.260	0.69	0.52	1.02
26.0	20.0	39	351	0.272	48	568	0.265	0.81	0.62	1.03
9.5	27.8	18	224	0.277	20	316	0.268	0.90	0.71	1.03

The comparison ratios for lateral displacement were consistently within 3% of 1.0, indicating the top of column displacements occurring in the linear elastic FE models closely matched those of the nonlinear FE models and the field observations. This shows that the imposed strain in the bent caps was the same in both the linear elastic and nonlinear models, allowing direct comparison of the moment and shear results between the two models on a consistent basis. The comparison ratios for moment and shear ranged from the conservative (ratio < 0.5) to significantly unconservative (ratio > 0.5) depending on the column height and the loading effect in question (i.e., moment or shear). The taller columns had the less conservative results, indicating and as shown in the previous chapters, there was less cracking seen in the results from the nonlinear models.

Table 6.2 contains the results and comparison ratios of the parametric study based on varying the shape of the columns in the linear elastic and nonlinear models.

Table 6.2. Comparison of results from the column shape cases

		NL Abaqus Model Results			LE LARSA Model Results			Ratio NL/LE		
EI/L^3 (kip/in.)	**Moment of Inertia (ft^4)**	**Shear (kip)**	**Moment (kip-ft)**	**Lateral Disp. (in.)**	**Shear (kip)**	**Moment (kip-ft)**	**Lateral Disp. (in.)**	**Shear**	**Moment**	**Lateral Disp.**
26.0	4.2	39	351	0.272	48	568	0.265	0.81	0.62	1.03
87.7	14.2	65	496	0.264	104	1,475	0.259	0.62	0.34	1.02
139.3	22.6	76	519	0.258	137	2,120	0.256	0.56	0.24	1.01
207.9	33.7	83	521	0.253	176	2,915	0.252	0.47	0.18	1.01
296.0	48.00	96	507	0.243	221	3,866	0.247	0.44	0.13	0.98

Larger diameter columns correspond to larger values of the column stiffness term, EI/L^3, corresponding to a stiffer frame overall. The results of the study comparing a nonlinear model to a linear elastic model predicted that column shears and moments show a greater discrepancy between the linear elastic and nonlinear model results when stiffer columns are used. This was also investigated in a parametric study where column size was varied for a given column height. The width of the column parallel to the pier cap was increased while the other dimension was held constant. Larger columns are often used in Iowa as warranted, such as for aesthetic considerations. As the columns become stiffer, column moments in the linear elastic model increased more rapidly than in the nonlinear model.

The study also investigated the effects of linearly varying the height of an individual column within the frame. The height of the tallest of the five columns in the pier is shown in Table 6.3. The column heights along the pier were consecutively decreased by 1 ft for a total difference in height of 5 ft between the two ends of the pier. Table 6.3 shows the results from the two column height cases investigated. A frame length of 90 ft and a column moment of inertia of 26.0 ft^4 was used for all the cases. While the differences were relatively minor between the varied and uniform cases, the results were opposite for the two cases. For the 15 ft column height, the uniform height generated larger moments and shear, while, for the 20 ft column height, the linearly varied model controlled the results. With only two data points, the amount of data was inadequate to form a conclusion from this parametric study.

Table 6.3. Comparison of results from the linearly varied stiffness compared to the uniform stiffness

Column Stiffness Case	Column Height (ft)	NL Abaqus Model Results			LE LARSA Model Results			Ratio NL/LE		
		Shear (kip)	Moment (kip-ft)	Lateral Disp. (in.)	Shear (kip)	Moment (kip-ft)	Lateral Disp. (in.)	Shear	Moment	Lateral Disp.
Linearly Varied	15.0	61	423	0.231	83	769	0.224	0.74	0.55	1.03
Uniform	15.0	68	472	0.266	98	905	0.260	0.69	0.52	1.02
Linearly Varied	20.0	43	390	0.307	56	657	0.301	0.76	0.59	1.02
Uniform	20.0	39	351	0.272	48	568	0.265	0.81	0.62	1.03

Table 6.4 shows the results of the investigation into the effect of the spacing between columns, also known as the bay length.

Table 6.4. Comparison of results from the bay length case compared to the base case

Bay Length (ft)	EI/L^3 (kip/in.)	NL Abaqus Model Results			LE LARSA Model Results			Ratio NL/LE		
		Shear (kip)	Moment (kip-ft)	Lateral Disp. (in.)	Shear (kip)	Moment (kip-ft)	Lateral Disp. (in.)	Shear	Moment	Lateral Disp.
10.0	26.0	40	361	0.276	53	606	0.262	0.76	0.60	1.05
18.0	26.0	39	351	0.272	48	568	0.265	0.81	0.62	1.03

A frame length of 90 ft and a column height of 20 ft were used for all of the cases. This evaluation captured the differences between nine column spaces at 10 ft on center and five column spaces 18 ft on center. The results indicated the number of columns equally spaced between the exterior columns affected the maximum thermal and shrinkage forces developed less than in the other cases previously developed.

Table 6.5 contains the results and comparison ratios of the parametric study based on varying the length of the frame in the linear elastic and nonlinear models.

Table 6.5. Comparison of results from the frame length cases

Frame Length (ft)	EI/L^3 (kip/in.)	NL Abaqus Model Results			LE LARSA Model Results			Ratio NL/LE		
		Shear (kip)	Moment (kip-ft)	Lateral Disp. (in.)	Shear (kip)	Moment (kip-ft)	Lateral Disp. (in.)	Shear	Moment	Lateral Disp.
18.0	26.0	9	74	0.056	10	125	0.054	0.84	0.59	1.04
54.0	26.0	24	215	0.165	27	332	0.161	0.88	0.65	1.03
90.0	26.0	39	351	0.272	48	568	0.265	0.81	0.62	1.03
126.0	26.0	49	464	0.377	68	796	0.366	0.73	0.58	1.03
162.0	26.0	58	553	0.480	87	1,014	0.462	0.66	0.55	1.04
198.0	26.0	64	621	0.580	105	1,220	0.553	0.61	0.51	1.05

The results are all based on a column height of 20 ft. The results cover a large variation in frame length and for the given parameters investigated captured the trends in the moments and shear based on the frame lengths. Both models showed an increase in moment and shear, although at slightly different rates. For the cases investigated, the comparison ratios indicated the AASHTO load factor of 0.50 for γ_{PS} , γ_{CR}, and γ_{SH} would be unconservative for moment and shear. However, further investigation of variation in column stiffness (variations in column height and moment of inertia) would be needed before broad statements could be made concerning the application of the AASHTO load factors for nonlinear and linear elastic models strictly based on frame length.

Summary

In summary, typical frame piers used in Iowa have historically been designed for thermal and shrinkage forces using the AASHTO BDS and the Iowa DOT BDM. This study investigated the loads imparted on these piers based on gathered field data and calibrated geometric nonlinear brick element FE models created using Abaqus CAE for a variety of different geometric configurations.

These results were then compared to results from the same geometric configurations analyzed using linear elastic beam element FE models created using LARSA and representing the traditional method of frame pier analysis. The results and ratios between the models did not fall within tightly defined parameters.

Some conclusions that can be drawn include the following. The stiffer a frame pier, the more conservative the AASHTO load factors for linear elastic models using gross section properties become. This does not necessarily make the use of linear elastic models using gross section properties not applicable for more flexible piers. This study dealt with in-plane thermal and shrinkage forces and engineering judgement needs to be applied to the results of any pier analysis to assess the magnitude of the effect that these in-plane forces represent in a controlling load combination. This is particularly true for taller, more flexible piers where the magnitude of the in-plane thermal and shrinkage loads, when compared to other forces acting on the pier, may not significantly affect the design.

Additionally, the Iowa DOT BDM, Section 6.6.2.12.1, calls attention to the additional consideration necessary for the design of in-plane forces on unusual pier types in the following statement: "… conditions such as highly irregular span lengths, large variations in pier heights or stiffnesses, skews greater than 30 degrees, unusually large deck widths, unusual bearings or combinations of bearings, and unusual pier types will require special analysis and consultation with the supervising Unit Leader." For these cases in particular, but for all pier design, consideration should be given to the following:

- Is the pier routine? The above paragraph lists a variety of conditions that, if present, would potentially indicate the pier is not routine. If none of these conditions are present, the pier should be considered routine for Iowa and designed using the Iowa BDM thermal and shrinkage guidance. Note that this study did not find discrepancy with this approach because the frame length of 90 ft used in the study would represent an "unusually large deck width or a skew greater than 30 degrees" and thus not be considered routine.
- Is the magnitude of the in-plane thermal and shrinkage loads prohibitive to the design or do they represent a significant portion of any of the load groups? If the answer is "no" to both questions, through the use of engineering judgement, it may be stated that the differences observed in this study would not significantly affect the design of the pier, and a pier designed using the Iowa BDM thermal and shrinkage guidance would be adequate.

If the above two questions do not describe the pier, it is likely non-standard and would need more refined analysis. This refined analysis can be done in several different ways.

For example, a nonlinear model similar to the one used for this study may be used. Also applicable is a linear elastic model(s) using cracked section properties where each load group indicates the column has cracked. This is an iterative approach as the model will often vary between load groups based on the extent of cracking anticipated. Alternatively, detailing changes to the pier, such as breaking a long pier into separate shorter piers, detailing hinges at the bases of columns, and further analysis into the rigidity assumed for the foundation, may all be used to reduce the thermal and shrinkage demands.

The approaches indicated in the previous paragraph would also need a value of 1.0 for the AASHTO load factors γ_{PS}, γ_{CR}, and γ_{SH}, which could potentially provide a more accurate model of the behavior for the frame pier. Finally, other load types may impart forces that could locally induce cracking in the concrete. For these cases, the use of cracked section properties in the regions anticipated to crack is necessary to capture the second order effects from vertical loads on the frame pier. Therefore, the designer should consider and evaluate the responses of the pier as a whole when determining the methods of analysis and the corresponding AASHTO load factors.

CHAPTER 7. CONCLUSIONS

This research project aimed to understand the structural behavior of frame piers under shrinkage and temperature effects. Several frame piers in Iowa were selected to be visually inspected or have their historical inspection reports reviewed. These frame piers were selected based on their expected susceptibility to temperature and shrinkage effects. From the inspections and inspection reports, very few of the frame piers showed any notable signs of damage. While the inspections suggested that frame piers in Iowa are sufficiently designed for shrinkage and temperature effects, additional field monitoring was needed to obtain insight into the actual magnitude and progression of shrinkage and temperature effects.

To address the relevant research questions, two frame piers were instrumented for long-term monitoring. For the frame piers instrumented, the columns were identified as more susceptible to temperature and shrinkage effects than the cap beam. The data from the instrumented frame piers were also utilized to validate a set of FE models that were developed in Abaqus to simulate shrinkage, creep, and thermal strains that the frame piers experience.

This study incorporated the ACI 209R shrinkage and creep model into the FE models. The ACI model was first calibrated with published experimental results and experiments performed on concrete samples collected from the construction of a frame pier in Iowa. The developed base model was then validated through comparison with field data collected from instrumented frame piers. The modeling process and details were determined to accurately capture how the frame piers responded to shrinkage, creep, and temperature effects.

Contraction of the frame piers was determined to be more critical than expansion. The worst casting time for a frame pier in Iowa was established to be any hot day in summer, particularly in June and July, due to the combined effects of shrinkage and temperature. The frame piers were found to experience the highest demand from temperature and shrinkage effects on cold days in winter, such as those in late January.

Several frame pier geometries were investigated with the validated FE model to identify geometries susceptible to temperature and shrinkage effects. Frame piers that had stiffer exterior than interior columns, stiffer interior than exterior columns, and linearly varied column stiffnesses were determined to not be any more susceptible to volumetric changes than frame piers with uniform columns. Furthermore, bay length was observed to have minimal effect on the susceptibility of frame piers to these effects.

The lateral stiffness of the columns, the length of the frame, and the flexural stiffness of the cap beam were found to be the most important factors in determining the susceptibility of a frame pier to temperature and shrinkage effects. The most critical factor was the lateral stiffness of the columns. High column stiffness, whether due to the cross-sectional shape of the column or the column height, can affect the demand on a frame pier due to volumetric changes more than the frame length. However, frame length was also determined to be an important factor given exceptionally long frames with moderately stiff columns were determined to develop high internal forces due to shrinkage and temperature effects.

Finally, the flexural stiffness of the cap beam was determined to affect the formation of cracks in the pier. Cap beams with lower flexural stiffness than the columns experienced vertical cracking in the cap beam itself, while cap beams with higher flexural stiffness than the columns experienced horizontal cracking at the column-beam interface. The most reliable metric considered to identify frame pier susceptibility to volumetric changes was the frame length multiplied by the column stiffness, treating the base of the column as fixed and accounting for the restraint provided by the cap beam.

This study concluded with the development of a simplistic procedure to account for temperature and shrinkage effects in frame piers. This simplistic model covered various parametric cases, following the guidance in the Iowa DOT BDM. To compare linear elastic versus complex nonlinear models, the same pier geometries and material properties were modeled. The results showed very good correlation on lateral displacement in the cases investigated, validating the comparable strains from thermal and shrinkage loading between the models.

However, the moments and shears from the linear analysis were larger, but by varying magnitudes, than the values from the nonlinear models. Per AASHTO, the linear analysis using gross section properties is allowed to use a 0.5 load factor, while the refined nonlinear analysis requires a 1.0 load factor. For some of the cases, there was good correlation between these values. However, outliers were also apparent. For example, in cases where the interior and exterior columns varied in thickness, the nonlinear model captured the cracking of the cap to relieve stresses, particularly when the moment of inertia of the columns became much larger than the cap. For cases like this, a more refined analysis similar to options discussed in this report are recommended.

REFERENCES

AASHTO. 2012. *AASHTO Load and Resistance Factor Design (LRFD) Bridge Design Specifications*. American Association of State Highway and Transportation Officials, Washington, DC.

Abaqus. 2018. *User's Manual*. Dassault Systems Simulia Corp., Pawtucket, RI.

ACI 122. 2002. *ACI 122R-02: Guide to Thermal Properties of Concrete and Masonry Systems*. American Concrete Institute, Farmington Hills, MI.

ACI 209. 1992. *ACI 209R-92: Prediction of Creep, Shrinkage, and Temperature Effects in Concrete Structures*. (Reapproved 1997). American Concrete Institute, Farmington Hills, MI.

ACI 209. 2008. *ACI 209.2R-08: Guide for Modeling and Calculating Shrinkage and Creep in Hardened Concrete*. American Concrete Institute, Farmington Hills, MI.

ACI 318. 2014. *ACI 318-14: Building Code Requirements for Structural Concrete*. American Concrete Institute, Farmington Hills, MI.

Ahmed, K. 2011. Temperature Effects in Multi-Story Buildings. *Journal of Engineering Sciences*, Vol. 39, No. 2, pp. 249–267.

Ali, W. and G. Urgessa. 2014. Computational Model for Internal Relative Humidity Distributions in Concrete. *Journal of Computational Engineering*, Vol. 2014, pp. 1–7.

Altoubat, S. A. and D. A. Lange. 2001. Creep, Shrinkage, and Cracking of Concrete at Early Ages. *Materials Journal*, Vol. 98, No. 4, pp. 323–331.

Arguez, A., I. Durre, S. Applequist, M. Squires, R. Vose, X. Yin, and R. Bilotta. 2010. *U.S. Climate Normals (1981-2010).* National Oceanic and Atmospheric Administration (NOAA), National Centers for Environmental Information.

Badrah, M. K. and M. N. Jadid. 2014. Investigation of Developed Thermal Forces in Long Concrete Frame Structures. *The Open Civil Engineering Journal*, Vol. 7, pp. 210–217.

Baweja, S. 1995. Creep and Shrinkage Prediction Model for Analysis and Design of Concrete Structures: Model B_3. *Materials and Structures*, Vol. 28, pp. 357–365.

Bažant, Z. and S.-S. Kim. 1979. Approximate Relaxation Function for Concrete. *Journal of the Structural Division*, Vol. 105, No. 12, pp. 2695–2705.

Bažant, Z. and G.-H. Li. 2008. *Comprehensive Database on Concrete Creep and Shrinkage*. Structural Engineering Report No. 08-3/A210c. Northwestern University, Evanston, IL.

Bažant, Z. and G.-H. Li. 2008. Comprehensive Database on Concrete Creep and Shrinkage. *Materials Journal*, Vol. 105, No. 6, pp. 635–637.

Bažant, Z. P. and Q. Yu. 2010. Modeling of Concrete Creep and Hygrothermal Deformations, and Computation of their Structural Effects. In *Computational Modelling of Concrete Structures*, pp. 3–13.

Bentz, D. P. 2000. *A Computer Model to Predict the Surface Temperature and Time-of-Wetness of Concrete Pavements and Bridge Decks*. NIST Interagency/Internal Report (NISTIR) 6551. National Institute of Standards and Technology, Gaithersburg, MD.

Bissonnette, B.and M. Pigeon. 1995. Tensile Creep at Early Ages of Ordinary, Silica Fume and Fiber Reinforced Concretes. *Cement and Concrete Research*, Vol. 25, No. 5, pp. 1075–1085.

DeJong, A., W. Shi, B. Shafei, and T. Hosteng. 2021a. Integral Abutment Connections with Grouted Reinforcing Bar Couplers and Ultra-High Performance Concrete. *ASCE Journal of Bridge Engineering*, Vol. 26, No. 8, 04021042.

DeJong, A., W. Shi, B. Shafei, and T. Hosteng. 2021b. Laboratory and Numerical Investigation of Integral Abutment Connections with Pile Couplers. *Journal of Engineering Structures*, Vol. 248, 113159.

Gilbert, R. I. 1988. *Time Effects in Concrete Structures*. Elsevier, Amsterdam, Netherlands.

Gilbert, R. I. 1990. Time-Dependent Analysis of Composite Steel-Concrete Sections. *Journal of Structural Engineering*, Vol. 115, No. 11, pp. 2687–2705.

Gilbert, R. I. 1992. Shrinkage Cracking in Fully Restrained Concrete Members. *Structural Journal*, Vol. 89, No. 2, pp. 141–149.

Gilbert, R. I. and G. Ranzi 2011. *Time-Dependent Behaviour of Concrete Structures*. *Time-Dependent Behaviour of Concrete Structures*. CRC Press, London.

Gribniak, V., G. Kaklauskas, R. Kliukas, and R. Jakubovskis. 2013. Shrinkage Effect on Short-Term Deformation Behavior of Reinforced Concrete – When It Should Not Be Neglected. *Materials and Design*, Vol. 51, pp. 1060–1070.

Hsu, L. S., and C. T.T. Hsu. 1994. Complete Stress – Strain Behaviour of High-Strength Concrete under Compression. *Magazine of Concrete Research*, Vol. 46, No. 169, pp. 301–312. https://doi.org/10.1680/macr.1994.46.169.301.

Hwang, C. C., and Y. H. Jiang. 2003. Extensions to the Finite Element Method for Thermal Analysis of Underground Cable Systems. *Electric Power Systems Research*, Vol. 64, No. 2, pp. 159–164.

Iowa DOT Highway Division. 2015. *Standard Specifications for Highway and Bridge Construction*. Iowa Department of Transportation, Ames, IA.

Iowa DOT Office of Bridges and Structures. 2018. *LRFD Bridge Design Manual*. Iowa Department of Transportation, Ames, IA.

Karahan, M.and O. Kalenderli. 2011. Chapter 9: Coupled Electrical and Thermal Analysis of Power Cables Using Finite Element Method. From *Heat Transfer - Engineering Applications*.

Karim, R., M. Najimi, and B. Shafei. 2019. Assessment of Transport Properties, Volume Stability, and Frost Resistance of Non-Proprietary Ultra-High Performance Concrete. *Journal of Construction and Building Materials*, Vol. 227, 117031.

Karim, R., and B. Shafei. 2021. Performance of Fiber-Reinforced Concrete Link Slabs with Embedded Steel and GFRP Rebars. *Journal of Engineering Structures*, Vol. 229, 111590.

Karim, R., and B. Shafei. 2022. Addition of Partial-Depth Link Slabs to Bridge Structures: Role of Support Conditions. *ASCE Journal of Bridge Engineering*, Vol. 27, No. 7, 04022049.

Kasera, S. C. 2014. *Simulation of the Effect of Deck Cracking Due to Creep and Shrinkage in Single Span Precast/Prestressed Concrete Bridges*. MS thesis. University of Cincinnati, OH.

Kazemian, M., and B. Shafei. 2022. Internal Curing Capabilities of Natural Zeolite to Improve the Hydration of Ultra-High Performance Concrete. *Journal of Construction and Building Materials*, Vol. 340, 127452.

Khan, I., A. Castel, and R. I. Gilbert. 2017. Tensile Creep and Early-Age Concrete Cracking Due to Restrained Shrinkage. *Construction and Building Materials*, Vol. 149, pp. 705–715.

Khan, I,, A, Murray, A, Castel, and R. I. Gilbert. 2015. Experimental and Analytical Study of Creep and Shrinkage in Early-Age Concrete. In *10th International Conference on Mechanics and Physics of Creep, Shrinkage, and Durability of Concrete and Concrete Structures*, September 21–23, Vienna, Austria, pp. 1066–1075.

Khatami, D., B. Shafei, and O. Smadi. 2016. Management of Bridges under Aging Mechanisms and Extreme Events: A Risk-Based Approach. *Transportation Research Record: Journal of the Transportation Research Board*, Vol. 2550, No. 1, pp. 89–95.

Khatami, D., and B. Shafei. 2021. Impact of Climate Conditions on Deteriorating Reinforced Concrete Bridges in the U.S. Midwest Region. *ASCE Journal of Performance of Constructed Facilities*, Vol. 35, No. 1, 04020129.

Kulkarni, A., and B. Shafei. 2018. Impact of Extreme Events on Transportation Infrastructure in Iowa: A Bayesian Network Approach. *Transportation Research Record: Journal of the Transportation Research Board*, Vol. 2672, No. 48, pp. 45–57.

Lampropoulos, A. P. and S. E. Dritsos. 2011. Concrete Shrinkage Effect on the Behavior of RC Columns under Monotonic and Cyclic Loading. *Construction and Building Materials*, Vol. 25, No. 4, pp. 1596–1602.

Levy, C. 2010. *Numerical Investigation of the Effects of Shrinkage and Thermal Loading on the Behaviour of Misaligned Dowels in Jointed Concrete Pavement*. MS thesis. University of Waterloo, Ontario.

Li, F., J. Guo, H. Huang, and Q. Liu. 2013. Concrete Creep and Shrinkage Effect Analysis Program Development. *Applied Mechanics and Materials*, Vols. 405–408, pp. 850–855.

Michał, S., and W. Andrzej. 2015. Calibration of the CDP Model Parameters in Abaqus. *The 2015 World Congress on Advances in Structural Engineering and Mechanics*, August 25–29, Incheon, Korea, pp. 1–11.

Mills, A. F. 1999. *Basic Heat and Mass Transfer*. Second edition. Prentice-Hall, Upper Saddle River, NJ.

Østergaard, L., D. A. Lange, S. A. Altoubat, and H. Stang. 2001. Tensile Basic Creep of Early-Age Concrete under Constant Load. *Cement and Concrete Research*, Vol. 31, No. 12, pp. 1895–1899.

Perez, R., S. Kivalov, A. Zelenka, J. Schlemmer, and K. Hemker, Jr. 2010. Improving the Performance of Sattelite-to-Irradiance Models Using the Satellite's Infrared Sensors. *American Solar Energy Society Annual Conference*, May 17–22, Phoenix, AZ, pp. 1–8.

Purani, D. 2013. *Incorporating Shrinkage Effects in FE Modeling of Prestressed Concrete Bridge*. MS thesis. Rutgers, The State University of New Jersey, New Brunswick, NJ.

Ranaivomanana, N., S. Multon, and A. Turatsinze. 2013. Tensile, Compressive and Flexural Basic Creep of Concrete at Different Stress Levels. *Cement and Concrete Research*, Vol. 52, pp. 1–10.

Šahinagić-Isović, M., G. Markovski, and M. Ćećez. 2012. Shrinkage Strain of Concrete - Causes and Types. *Građevinar*, Vol. 9, No. 9, pp. 727–734.

Schultz, A. E. 1992. Approximating Lateral Stiffness of Stories in Elastic Frames. *Journal of Structural Engineering*, Vol. 118, No. 1, pp. 243–263.

Shafei, B., A. Alipour, and M. Shinozuka. 2012. Prediction of Corrosion Initiation in Reinforced Concrete Members Subjected to Environmental Stressors: A Finite-Element Framework. *Journal of Cement and Concrete Research*, Vol. 42, No. 2, pp. 365–376.

Shafei, B., and A. Alipour. 2015a. Application of Large-Scale Non-Gaussian Stochastic Fields for the Study of Corrosion-Induced Structural Deterioration. *Journal of Engineering Structures*, Vol. 88, pp. 262–276.

Shafei, B., and A. Alipour. 2015b. Estimation of Corrosion Initiation Time in Reinforced Concrete Bridge Columns: How to Incorporate Spatial and Temporal Uncertainties. *ASCE Journal of Engineering Mechanics*, Vol. 141, No. 10, 04015037.

Shi, W., B. Shafei, Z. Liu, and B. Phares. 2019. Early-Age Performance of Longitudinal Bridge Joints Made with Shrinkage-Compensating Cement Concrete. *Journal of Engineering Structures*, Vol. 197, 109391.

Shi, W., M. Najimi, and B. Shafei. 2020a. Reinforcement Corrosion and Transport of Water and Chloride Ions in Shrinkage-Compensating Cement Concretes. *Journal of Cement and Concrete Research*, Vol. 135, 106121.

Shi, W., M. Najimi, and B. Shafei. 2020b. Chloride Penetration in Shrinkage-Compensating Cement Concretes. *Journal of Cement and Concrete Composites*, Vol. 113, 103656.

Shi, W., B. Shafei, Z. Liu, and B. Phares. 2020c. Longitudinal Box-Beam Bridge Joints under Monotonic and Cyclic Loads. *Journal of Engineering Structures*, Vol. 220, 110976.

Sümer, Y. and M. Aktaş. 2015. Defining Parameters for Concrete Damage Plasticity Model. *Challenge Journal of Structural Mechanics*, Vol. 1, No. 3, pp. 149–155.

Tinni, A. 2008. *The Importance of the Factors Affecting Concrete Shrinkage*. Pavement Information Note No. 20. TMC – Tinni Management Consulting. pp. 1–6.

Tong, T. 2016. *Computational Modelling of Concrete Time-Dependent Mechanics and Its Application to Large-Scale Structure Analysis*. PhD dissertation. University of Pittsburgh, PA.

Wahalathantri, B. L., D. P. Thambiratnam, T. H. T. Chan, and S. Fawzia. 2011. A Material Model for Flexural Crack Simulation in RC Using ABAQUS. *Proceedings of the First International Conference on Engineering, Designing, and Developing the Built Environment for Sustainable Wellbeing*, pp. 260–264.

Wei, Y. and W. Hansen. 2012. Tensile Creep Behavior of Concrete Subject to Constant Restraint at Very Early Ages. *Journal of Materials in Civil Engineering*, Vol. 25, No. 9, pp. 1277–1284.

THE INSTITUTE FOR TRANSPORTATION IS THE FOCAL POINT FOR TRANSPORTATION AT IOWA STATE UNIVERSITY.

InTrans centers and programs perform transportation research and provide technology transfer services for government agencies and private companies;

InTrans contributes to Iowa State University and the College of Engineering's educational programs for transportation students and provides K–12 outreach; and

InTrans conducts local, regional, and national transportation services and continuing education programs.

INSTITUTE FOR TRANSPORTATION
IOWA STATE UNIVERSITY

Visit InTrans.iastate.edu for color pdfs of this and other research reports.